Canadian Nuclear Battery$^{\text{TM}}$

PRELIMINARY THERMODYNAMICS AND NEUTRONICS ANALYSIS OF CANADIAN NUCLEAR BATTERY$^{\text{TM}}$

By Miao Yu

A Report Submitted to the School of Graduate Studies in the Partial Fulfillment of the Requirements for the Degree Master in Applied Science

McMaster University, March, 2022

McMaster University
MASTER of APPLIED SCIENCE (2022)
Hamilton, Ontario (Engineering Physics)

TITLE: Preliminary Thermodynamics and Neutronics Analysis of Canadian Nuclear Battery$^{\mathrm{TM}}$
AUTHOR: Miao Yu (McMaster University)
SUPERVISOR: Dr. Adriaan Buijs
NUMBER OF PAGES: xvii, 133

Abstract

The Canadian Nuclear Battery$^{\text{TM}}$ (CNB) is a 2400 kWth (500 kWe) small modular reactor (SMR) initially designed in the 1980s targeted at applications in remote locations in Northern Canada [1]–[3]. The reactor uses potassium or sodium heat pipes as the primary heat removal system which demonstrate passive cooling characteristics. Heat pipes are metal pipes filled with working liquid and its vapour phase to transfer heat from the heated area (evaporator section) to the cooled area (condenser section) through phase change. Theoretical investigations are carried out to produce adequate information for the effective utilization of the heat pipe design in the reactor. Steady-state and a hypothetical double-power transient are simulated with STAR-CCM+ to understand the thermodynamics of the core and the propagation of heat pipe failures in accidental events. Preliminary neutronics calculations are carried out for the hypothetical double power transient and 50% power setback transient to evaluate the neutronics and xenon behaviours of the reactor. The purpose of the study is to provide first information about the thermal and neutronics performances of CNB in the early stage of development.

Acknowledgements

The two and a half years I have spent at McMaster University are a meaningful and profound period of time in my life.

I thank the patience and guidance of my supervisor Dr. Buijs, suggestions and software package support from Dr. Novog, and instructions and teaching from Dr. Luxat, Dr. Rouben, and Dr. Nagasaki which opened my eyes to the field of nuclear engineering. I also appreciate the help from the CNB group members and discussions we've had, and I have enjoyed the times spent together with other nuclear engineering students.

This thesis is targeted to analyse the thermophysical behaviours of the Canadian Nuclear Batter, a newly launched SMR program, including the operation of heat pipes and heat distribution throughout the reactor core. The reactor configuration has changed for a few times, in this material only the results of the last configuration when I was working on the thermophysics of CNB are presented. As a freshman in the field of nuclear energy, I have accumulated understanding and experience of the R&D process of a reactor, and witnessed the progressing of the project, which is explorative, incremental, and retrospective. I wish for the best success of the project and a bright career for those involved in this joint effort.

Lastly I thank myself for trying to be solid and consistent in the period of pandemic, and holding on to the wish for a better self and future.

Contents

List of Figures

List of Tables

Variables

U : axial vapour velocity (m/s)
C_{son} : speed of sound (m/s)
$Mach$: $Mach$ number, defined as $\frac{U}{C_{\text{son}}}$ (dimensionless)
M : molar mass of working liquid (kg/mol)
R : universal gas constant (J/K-mol)
R_{g} : specific gas constant, defined as $R_{\text{g}} = \frac{R}{M}$ (J/K-kg)
T : temperature (°C, in calculations it is K)
L : latent heat of vaporization (J/kg)
ρ_{v} : density of vapour potassium (kg/m^3)
ρ_{l} : density of liquid potassium (kg/m^3)
x : position along the heat pipe (m)
w : the width of the individual crosshatch channels on the inside surface of the pipe wall (m)
d : depth of the individual crosshatch channels on the inside of the pipe wall (m)
q : axial heat flux (W/m^2)
Q : heat flow or total heat transfer rate (W)
$\dot{m}$: axial vapour mass flow (kg/m^2-s)
A_{v} : the cross-section area of vapour passage (m^2)
A_{l} : cross sectional area of liquid passage (m^2)
A_{s} : area of a pore of the wick (m^2)
μ_{v} : viscosity of vapour potassium (Pa-s)
μ_{l} : viscosity of liquid potassium (Pa-s)
γ : specific heat ratio of vapour potassium (dimensionless)
f : Fanning friction factor (dimensionless)
τ : sheer stress of vapour on the wick (Pa)
r_{v} : radius of vapour space (and the radius of the inside surface of the wick) (m)
r_{eff} : effective radius of the wick (m)
r_{b} : radius of a bubble (m)
r_{i} : radius of the inside surface of pipe wall (m)
$r_{\text{h,s}}$: hydraulic radius of the wick surface pores (m)
r_{pi} : wick pore radius of the inner wick (m)
r_{po} : wick pore radius of the outer wick (m)
C_{s} : wetted perimeter of a pore of the wick (m)
l_{eff} : effective length of the heat pipe (m)
l_{eva} : length of the evaporator section (m)
l_{adi} : length of the adiabatic section (m)

l_{con} : length of the condenser section (m)
k : permeability of the wick (dimensionless)
σ : surface tension of liquid potassium in heat pipe calculations (N/m), microscopic cross section in neutronics (barn)
λ : thermal conductivity (W/m-K)
$poro_{\text{rad}}$: porosity of the wick (dimensionless)
P : pressure (Pa) for heat pipe calculations, power (W) for thermodynamics calculations
$P_{\text{cap,max}}$: maximum of capillary pressure difference (Pa)
P_{s} : saturation pressure of vapour (Pa)
P_{vis}: viscous vapour pressure drop (Pa)
P_{i} : inertial vapour pressure drop (Pa)
P_{l} : viscous liquid pressure drop (Pa)
P_{z} : hydrostatic pressure drop (Pa)
P_{b} : pressure inside the bubble (Pa)
T_{inf} : temperature of liquid far from pipe wall (K)
ΔT_{boil} : superheat of nucleate boiling (K)
Re : Reynolds number (dimensionless)
Re_{r} : radial Reynolds number (dimensionless)
We : Weber number, the ratio of the shear force by the vapour to the liquid of the surface tension force that retain liquid in the wick (dimensionless)
ϕ : neutron flux (n/cm^3-s)
$\vec{J}$: neutron current (n/cm^3-s)
ν : fission neutron yield (dimensionless, number of neutrons)
Σ : macroscopic cross section (cm^{-1})
k_{eff} : multiplication constant constant (dimensionless, 1 mk $= 1 \times 10^{-3}$)
ρ : reactivity (dimensionless, or mk)
B^2 : geometrical buckling (cm^{-2})
D : diffusion constant (cm)
β : delayed neutron fraction (dimensionless)
Λ : average neutron generation time (s)
λ : decay constant (s^{-1})

Subscripts:

0 : the beginning of evaporator (where the vapour velocity is null, and thus also the stagnation state of the vapour)
v : vapour phase
l : liquid phase

f : fission
a : absorption
t : total
ss : steady-state
fp : full power (nominal power)

Chapter 1

Introduction

1.1 High-Temperature Gas-Cooled Reactors and CNB

Established in 2000, the International Generation-IV Reactor initiative proposed several kinds of new generation nuclear reactor designs to improve safety, proliferation control, sustainability, and economy of reactor systems [4]. Among those reactors, Very-High-Temperature Gas-Cooled Reactor (VHTGR, with a temperature of 900-1000 °C), or High-Temperature Gas-Cooled Reactor (HTGR, with a lower temperature of 700-850 °C), features graphite moderator in prismatic block or pebble-bed form, helium noble gas coolant, ceramic fuel particles surrounded by coatings (TRISO fuel particles), enabling a rise in the operating temperature in comparison with traditional Gas Cooled Reactor (GCR). Higher outlet coolant temperature not only increases the energy conversion efficiency of the reactor, but also enables some other high-temperature industrial processes like hydrogen production.

There are mainly two types of VHTGR or HTGR: pebble-bed reactor (PBR) and prismatic modular reactor (PMR). Some existing reactor designs are: the prismatic core High Temperature Test Reactor (HTTR) in Japan, the high-temperature reactor pebble-bed modules (HTR-PM) in China, the Gas Turbine Modular Helium Reactor (GT-MHR) in Russia, and the Next Generation Nuclear Plant (NGNP) in the United States.

The concept of Modular HTGR is a further step of development upon HTGR, starting with the 80 MW(e) HTR module (HTR-MODUL) design proposed by Siemens/Interatom [5] in 1980s. The concept was originally designed for industrial process heat applications, but soon came into utilization for electricity production by virtue of the passive safety features and the appealing characteristics of the modular concept. The safety philosophy of Modular HTGR was that the protection of the environment and containment of fission products were ensured by passive system features even under severe, extreme accident conditions, and in the case of complete loss of active cooling systems or coolant, the fuel temperature would still keep within proper range such that fission products were well contained in fuel elements.

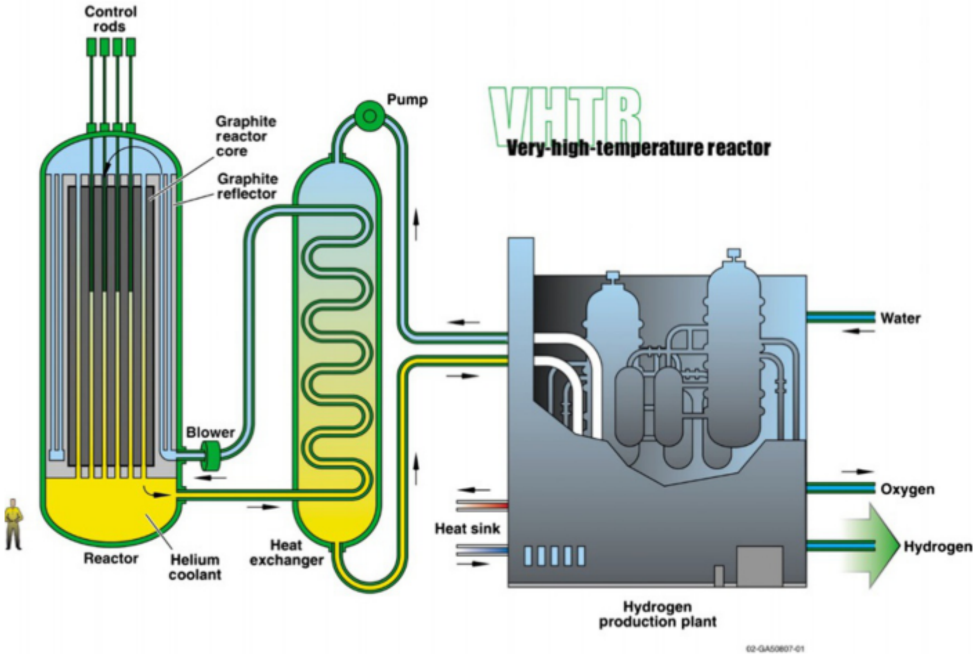

Figure 1.1: Very-High-Temperature Reactor [4].

The Canadian Nuclear Battery (CNB) studied in this material is a 2400 kWth (500 kWe) small modular reactor (or say micro reactor due to the small power) initially designed in 1980s targeted at remote locations in Northern Canada as a substitute of diesel fuel to generate electricity. It shares many similarities with Modular HTGR. Some of the important characteristics of Modular HTGR are [5]:

- The use of TRISO fuel particles designed to keep all radiologically related fission products up to fuel temperatures about 1600 °C.
- Active cooling is not necessary in case of accidents. Decay heat is adequately transported by passive cooling mechanisms (conduction, radiation, natural convection, etc.) to simple outside surface coolers, e.g., a water cooled system outside the reactor pressure vessel.
- Reactor shutdown is enabled solely by absorber rods dropping into the boreholes in the reflector, which limits the core diameter to approximately 3 m.

- Graphite, which has accumulated substantial successful application experience in Gas-Cooled Reactors, is used in high temperature regions in the core, such as fuel elements and moderator. Failures due to high temperatures are impossible up the maximum temperature of 1600 °C.
- The single phase noble gas coolant or circulating atmosphere, helium, is inert in terms of both chemistry and neutronic physics, further enhancing the safety features of the reactor.

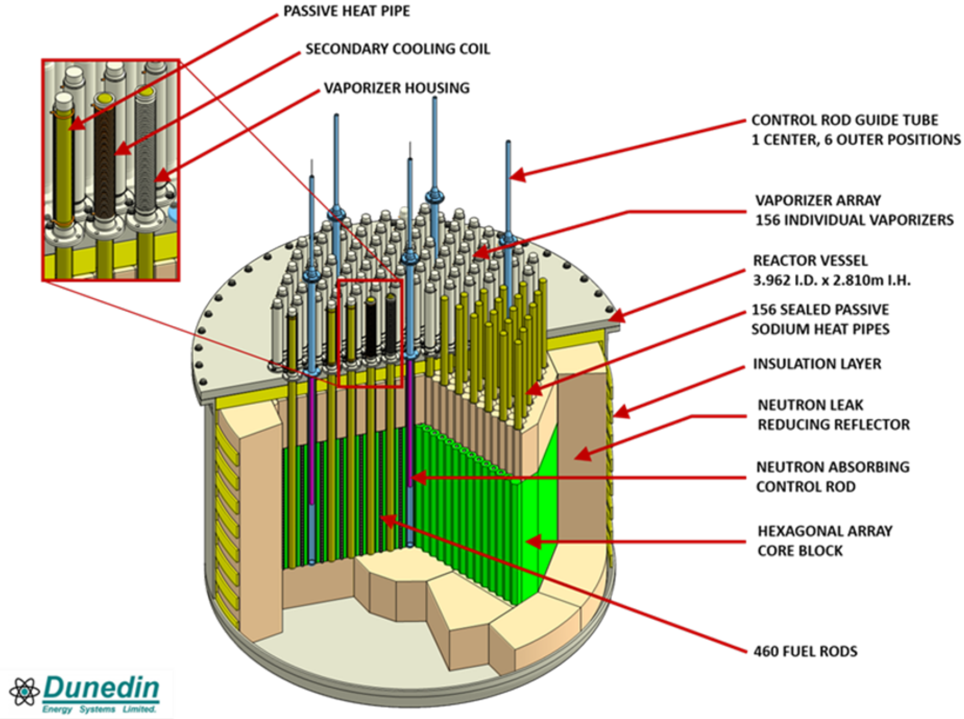

Figure 1.2: Canadian Nuclear Battery core module. Figure courtesy from Dunedin, Inc..

1.1.1 Graphite

Nuclear graphite is a porous, polycrystalline material made from coke, usually produced as a by-product of the coal or oil industry. It has been widely used in the nuclear industry as moderator, reflector, and fuel binder material, etc., due to its favorable properties like low neutron absorption cross section, high moderating efficiency, high mechanical strength, large thermal capacity, as well as high machinability. The Thorium High Temperature Reactor (THTR) in Germany has approximately 400 ton graphite; for the HTR-PM reactor in China there is more than 1,000 tons of nuclear graphite as structural material and matrix graphite as pebble fuel spheres. Some typical requirements for modern nuclear graphite are [6]:

- high purity with a low elemental contamination
- good isotropic characteristic
- machinability into bulk molds
- validated irradiation database

The properties of nuclear graphite are highly dependent on the raw material chosen and the manufacture procedure, which need to be judiciously planned out in order to obtain the desired characteristics [6], [7]. In the nuclear reactor, graphite is exposed to the radiation of high-energy neutron fluxes causing irradiation damages to its crystal structure and changes to most of the properties. The neutron energy required to displace a carbon atom in the lattice is around 60 eV, but in a reactor the energies inducing most of the damage is above 0.1 MeV. A high-energy neutron hits the carbon atom out of its lattice position to interstitial positions between the basal panels leaving a vacancy in the lattice, and causes subsequent cascading knock-ons to other atoms. Interstitial clusters or loops of atoms or vacancies can also be formed during this process.

The response of nuclear graphite to high-energy irradiation is highly dependent on the specific type of graphite chosen. Purity, anisotropy, grain size, manufacture processes and other aspects exhibit various influences on the properties of graphite. However, it is not well understood the relation between those microscopic in-crystal structures and the macroscopic bulk characteristics as well as their evolution in irradiated environments. The irradiation induced changes in graphite properties can hardly be precisely evaluated with current model developed with historical data. Therefore, it is of crucial importance to understand the behaviours of specific graphite grades.

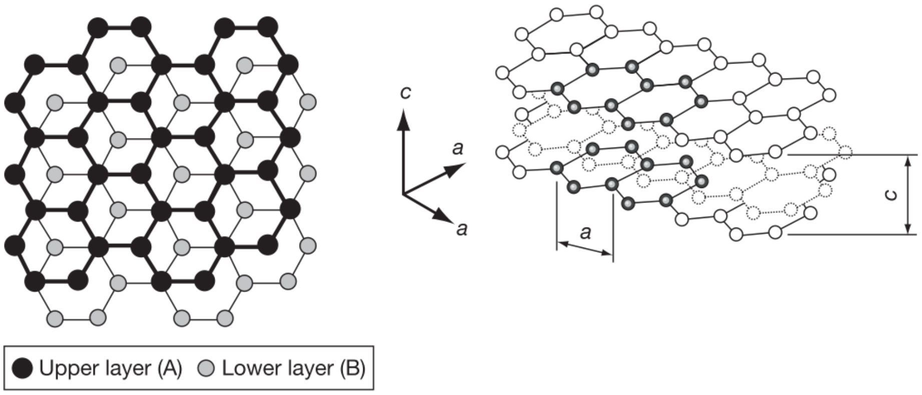

Figure 1.3: Crystal structure of graphite [7]

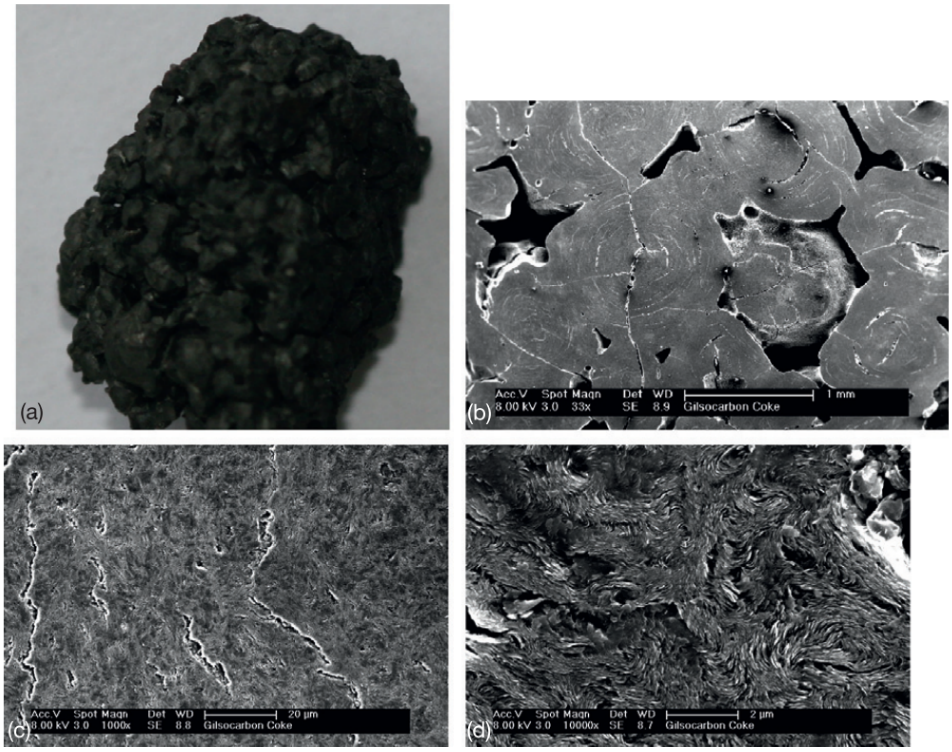

Figure 1.4: Microstructure of Gilsonite raw-coke from Utah in the United States. (a) Photograph of Gilsonite coke, (b) Scanning electron microscopy (SEM) image of polished Gilsonite coke, (c) the region around cracks in the spherical shape of the coke particles, and (d) a higher magnification SEM image showing the random orientation of platelets [7].

1.1.2 TRISO Fuel

Tristructural-Isotropic (TRISO) coated particles are nuclear fuel particles initially developed in Germany aiming to improve the high temperature endurance and fission product retention capabilities of fuel. TRISO particles are used in modern HTGR technologies and are investigated to be employed in traditional reactor types [8], [9]. In a pebble-bed reactor TRISO particles are integrated in a graphite matrix to form fuel compacts, such as pebble elements in pebble bed reactors and fuel rods in prismatic reactors. The TRISO particles consist of a fuel kernel, porous carbon buffer layer, inner pyrolytic carbon (IPyC) layer, SiC, and outer pyrolytic carbon (OPyC) (Figure 1.5). The fuel kernel contains the fissile and fertile elements like uranium, plutonium, and thorium. The carbon buffer serves to relieve the recoiling of fission fragments and changes in particle dimensions, and contain fission gas production. SiC is the major pressure structure keeping the particle intact and withstanding gas buildup, and also functions as a barrier to deter fission products (FPs) migration out of the particle [9]. The IPyC layer protects SiC from corrosive gases during the SiC coating process; both IPyC and OPyC layers keep SiC from chemical attacks during service of the particles, serving as additional barriers for FPs [10].

Manufacture methods and procedures have significant impact on the properties and capabilities of TRISO. And the dimensions of individual layers demonstrate statistical variations from particle to particle. The estimated failure fraction of a group of product particles and the manufacturing tolerances circumscribe the performance of TRISO. It is important to evaluate the statistical uncertainties of the manufacture processes to determine the quality of particles.

The temperature gradients and heat transfer across a particle directly influence the properties and performance of TRISO fuel. Various gasous products are produced in the kernel and the coatings containing carbon element, including FPs like Xe and Kr, oxygen produced due to thermal solubility and metallic elements depletion in the kernel, CO and CO_2 formation from reaction between oxygen and carbon. Gas generation along with radiation-induced structural deform and the differential thermal expansion of local regions lead to stresses and strains throughout the particle (Figure 1.6). Those phenomena need to be well investigated to understand the change and degradation processes of TRISO particles during reactor operation [9].

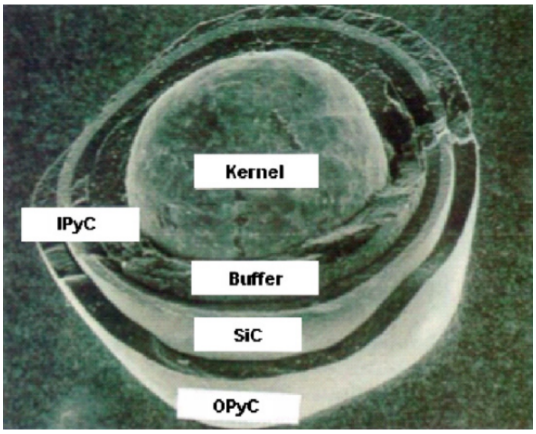

Figure 1.5: Photograph of a TRISO particle [8].

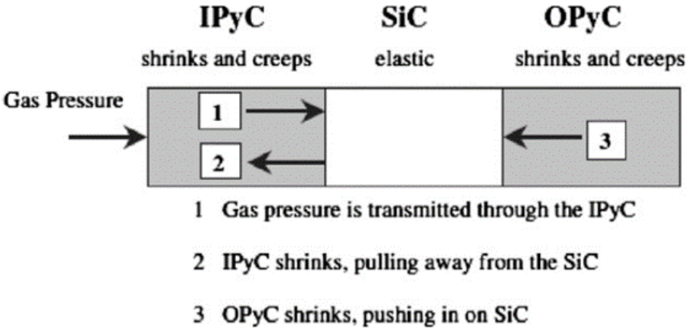

Figure 1.6: Pressures and strains across a TRISO particle [11].

1.2 Heat Pipe Micro Reactors

With the development of heat pipe technology, a new type of nuclear reactor has been brought out, i.e., the Heat Pipe Micro Reactors. Instead of the piping systems and pumps seen in traditional large reactors, heat pipe cooled reactors utilize heat pipes as the primary cooling system exhibiting passive cooling feature. Such solid core structures embody the safety, simplicity, and transportability characteristics of the reactor [12]. The existing Heat Pipe Reactor designs in current industry typically use fast spectrum and stainless steel monolith as the core structure material to contain fuel pins and heat pipes [13]. In comparison, the CNB makes use of neutrons in the thermal spectrum, and requires a graphite moderator to slow down neutrons to the desired range.

Micro reactors target at small scale and decentralized markets such as remote community, islands, military applications, space exploration, and so on [13]. The development of heat pipes provides a promising solution to the cooling problem of micro reactors; and the research efforts on micro reactors further promotes the maturing of heat pipe technologies. Nowadays the analysis of those solid heat pipe reactors are well carried out particularly in neutronics and thermal hydraulics. Redundant heat pipes can be arranged in the core layout to provide backup heat removal in case of one or a few heat pipes failure accidents. Table 1.1 shows some main parameters of several heat pipe reactor concepts in current market.

Parameters	Kilopower	SAIRS	MSR-B	HP-STMCs	eVinci
Institution	LANL	NMU	LANL	NMU	Westinghouse
Spectrum	Fast	Fast	Fast	Fast	Epithermal
Power	1 kWe	110 kWe	2 MWe	110 kWe	0.2-15 MWe
HP Fluid	Na	Na	K	Li	Na/K
HP Temperature	1050 K	1100-1200 K	930 K	1500 K	920 K
HP Material	Haynes-230	Mo-14Re	SS-316	Mo-14Re	–
HP Number	8	60	204	126	–
Refueling Period	10 years	5-7 years	>10 years	10-15 years	10 years
Efficiency	23.2%	22.7–27.3%	40%	6.7%	–
Fuel	U-Mo	UN	UO_2	UN	UN/U-Mo
Enrichment	93.1%	83.5%	19.75%	55–85%	19.75%
Reflector Material	BeO	BeO	Al_2O_3/BeO	BeO	BeO
Reactivity Control	Rod	Drum	Drum	Drum	Rod & Drum

Table 1.1: Parameters of several heat pipe reactors, adapted form Ref. [12]. Note: NMU - New Mexico University. U-Mo is the uranium-molybdenum alloy.

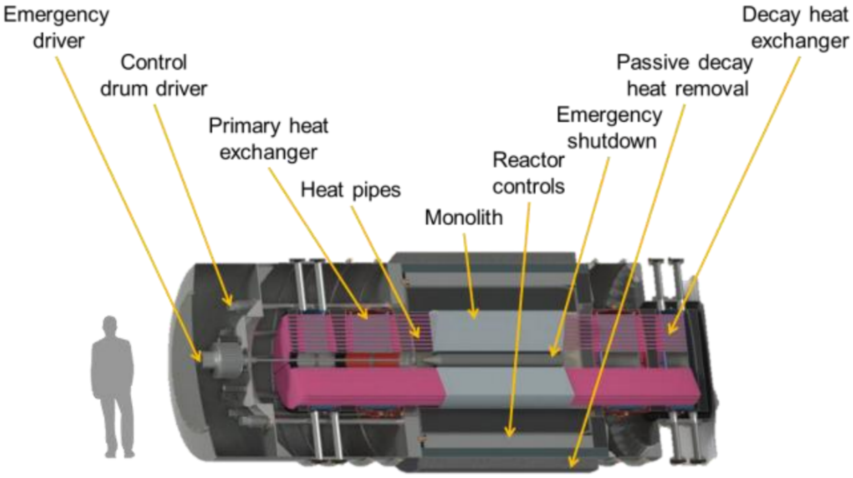

Figure 1.7: The eVinci micro reactor by Westinghouse [14]. eVinci utilizes neutrons in the epithermal range.

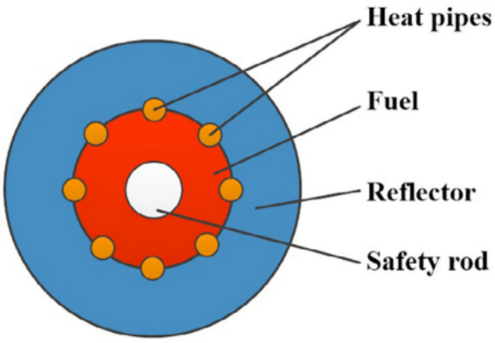

Figure 1.8: Cross-section of the Kilopower reactor [15].

1.3 Heat Pipe Structure and Working Principles

The major difference between HTGR and CNB is that CNB utilizes heat pipes as the primary heat transport system and phase change to transfer heat instead of gaseous coolant circulation (Figure 1.2), which is one highlight of the safety features of CNB. Heat pipes enable large amounts of heat transfer in a nearly isothermal state (which is reversely due to the rapid heat transfer) with only a small amount of working liquid by natural, passive phase change, eliminating the need for active pumping to extract thermal energy out of the reactor core.

Heat pipes take away heat by evaporating the working liquid at the evaporator section, and then the vapour flows to the condenser section where it gives up the latent heat to the heat sink and turns back to liquid state. The liquid return flow is mainly driven by the capillarity provided by the wick structure to flow from condenser to evaporator on the pipe wall (Figure 1.11). For CNB, the liquid flow is also assisted by gravity as the heat pipes are vertically mounted with the condenser region being higher than the evaporator.

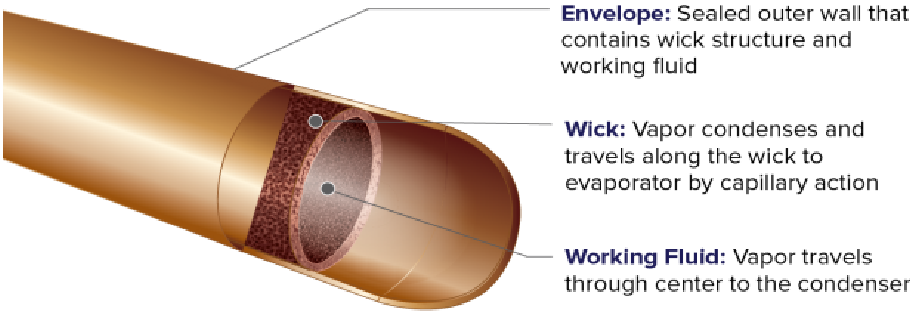

Figure 1.9: Schematic showing the structure and composition of heat pipe. Produced by Advanced Cooling Technologies, Inc. (ACT, Inc.) [16].

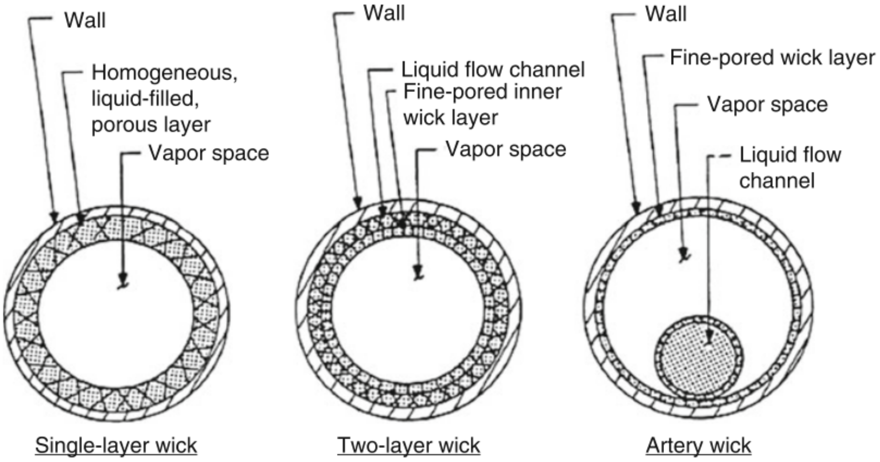

Figure 1.10: Examples of wick [17]

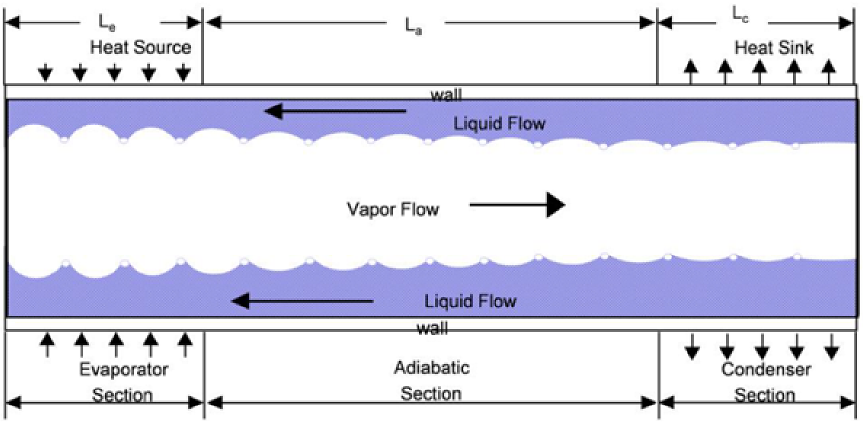

Figure 1.11: Schematic showing the operating principle of heat pipe [18].

The wick is a fine metal structure consisting of grooved liquid channels, thin films with small pores, and/or other structures that provide capillarity or flow passages to enable the liquid content to be transferred back to the evaporator from the condenser (Figure 1.10). In Figure 1.11, it is shown that the curvature of the liquid-vapour interface at the evaporator section is larger than the curvature at the condenser. This is because at the evaporator, liquid evaporates to the vapour space making the liquid meniscus to withdraw into the wick, while at the condenser vapour condenses back to liquid, causing flooding in the wick and consequently reduction in the curvature there. Thereby a pressure difference is created between the condenser and evaporator due to the different radii of local curvatures driving the liquid to heat source for evaporation (Figure 1.12).

Figure 1.12 presents the typical pressure profiles of vapour and liquid content in a heat pipe. Along the passage of vapour, it first accelerates in the evaporator due to constant evaporation; in the adiabatic section, the vapour is normally thought to remain at constant velocity; then in the condenser, the vapour decelerates and condenses back to liquid. This process causes pressure change along the vapour space. Meanwhile, there is also friction within the vapour and between the vapour and the wick introducing further pressure decrease; the pressure drop in the adiabatic section is mainly considered caused by friction. It can be noticed that in the condenser region only a fraction of the vapour pressure is recovered, which should be accounted for by the condensing process occurring in the condenser and the pressure losses due to friction; the resulted difference between the final vapour pressure and its pressure at the beginning of the evaporator is the vapour pressure drop.

Liquid is driven by the capillary pressure provided by the fine wick structure. It flows reversely from the condenser to the evaporator, and experiences friction with wick and wall structures as well as changes in hydrostatic and gravity pressure. The total variation of liquid pressure along its passage is the liquid pressure drop. Gravity can serve as either assist or hindrance depending on the relative position of condenser and evaporator. If the evaporator is lower then gravity will act as assist for the liquid to flow to evaporator; otherwise it will be a resistance.

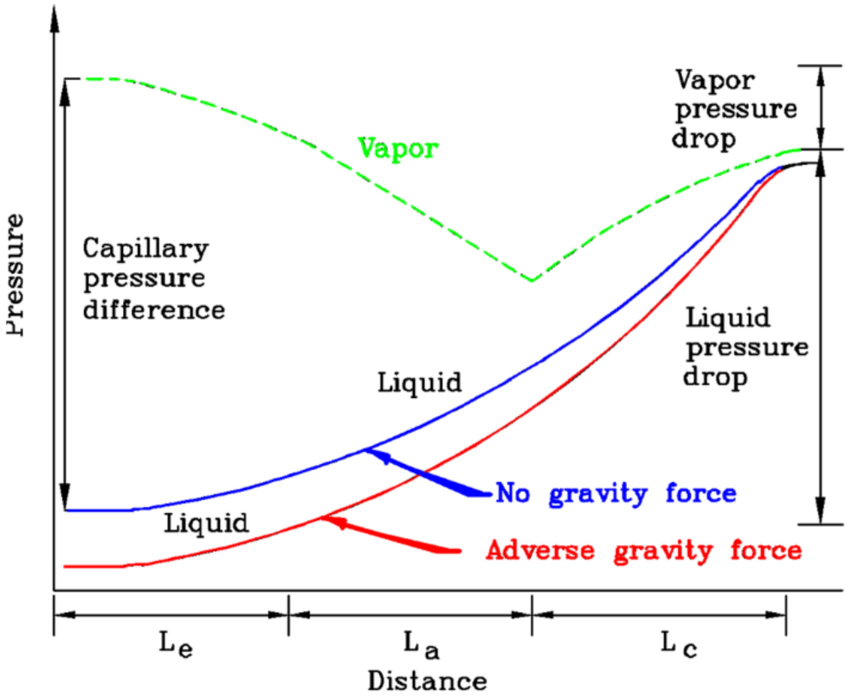

Figure 1.12: Typical pressure distributions in vapour and liquid fluid in heat pipe [19].

1.4 Heat Pipe Applications and Current Status

The heat pipe was introduced in 1964; since then the heat pipe has been continuously developed and used in various industries. A major application is cooling in modern electronic systems like CPUs, in which risen power and heat emission demands have led to greater requirements for cooling systems (Figure 1.13). Depending on the application requirements, heat pipes can operate at temperatures ranging from 4 K to 3000 K. A variety of materials can be chosen as the working fluid in heat pipe. Organic and inorganic, metal and gaseous elements demonstrate potential in various ranges of temperature (Table 1.2).

Figure 1.13: Heat pipe for CPU cooling [20].

T_{min}/°C	T_{max}/°C	Working Fluid	Potential Wall/Wick Materials
-246	-160	Oxygen	Aluminum, Stainless Steel
-203	-170	Nitrogen	Aluminum, Stainless Steel
-150	40	Propylene	Aluminum, Stainless Steel, Nickel
-65	100	Ammonia	Aluminum, Stainless Steel, Nickel
-60	25 to 100	Methanol	Copper Stainless Steel
20	280 to 300	Water	Copper, Monel, Nickel, Titanium
500	700	Potassium	Stainless Steel, Inconel, Haynes, Niobium
500	800	NaK	Stainless Steel, Inconel, Haynes, Niobium
600	1100	Sodium	Stainless Steel, Inconel, Haynes, Niobium
1100	1825	Lithium	Tungsten, Niobium, Molybdenum

Table 1.2: Working fluids and wall/wick materials. Adapted from Ref [21].

There are three main categories of heat pipe applications: temperature equalization, temperature control, and separation of heat source and sink [17]. Due to the extremely high thermal conductivity of heat pipe, temperature equalization can be achieved between two opposite faces of a platform by mounting a heat pipe between the two faces to maintain a balanced and steady temperature distribution and thus reduce thermal stresses. Temperature control is realized by the capability of heat pipe to rapidly transport large amounts of heat. For instance, a heat source with a changing flux can be kept at a constant temperature so long as the heat flux extremes lie within the operation range of the heat pipe. It also provides a method of transporting heat from a compact source to a remote sink, enabling applications such as dense packing of electronics without the undue worries about heat sink placement.

Under extreme space conditions heat pipes can still work by capillarity and natural evaporation and condensation of the working liquid. Such applications of heat pipe include spacecraft temperature equalization, temperature control, and radiator [17].

A recent concept of hybrid heat pipe for spent nuclear fuel cooling has been suggested by UNIST thermal-hydraulics and reactor safety laboratory in Korea [22]. The hybrid heat pipe has features similar with other heat pipes but with neutron absorber material placed in the centre core region, and thus it has both the function of common heat pipes to transport heat and additional function to control reactivity. Due to this unique feature, hybrid heat pipe is considered to be applied as both primary cooling system and neutron population control device in substitution to control rods in advanced reactor systems, wet storage pools, and dry storage casks for spent nuclear fuel [23].

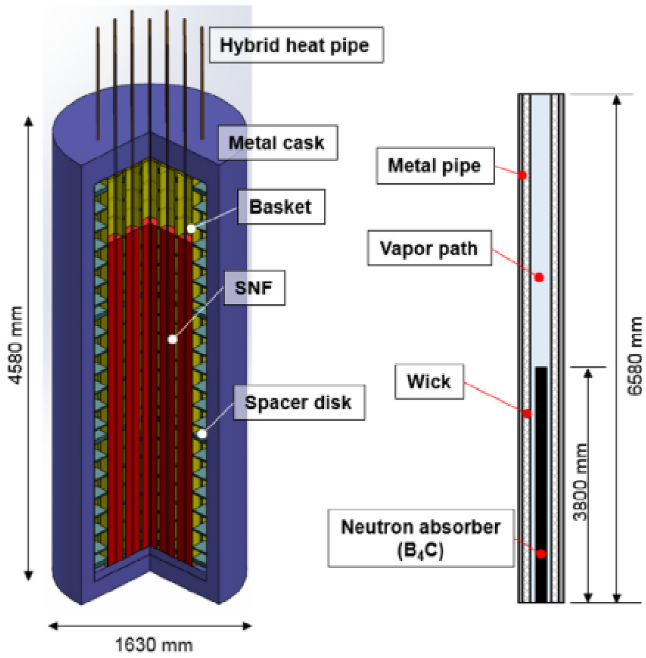

Figure 1.14: Hybrid heat pipe for spent fuel cooling [24].

1.5 Reactor Design and Development

In this section the procedure of reactor design is briefly reviewed with an emphasis on the neutronics and thermodynamics (or thermal-hydraulics) analysis. The primary goal of reactor design is to determine a set of parameters that ensures safety, reliability, and economy of the reactor, such as the multiplication factor, fuel enrichment, core geometry, etc.. It includes a number of considerations regarding not only neutronics, but also other subjects like thermal-hydraulics, material performance, and economic efficiency. The process of reactor design and development is a concerted effort involving multiple disciplines and requires good understanding and collaboration among all the segments [13]. Such considerations will exert a variety of confinements to the reactor in multiple kinds of ways. For example, the determination of core materials not only need to examine the thermal performance of the material to withstand high temperatures, but also the neutronics properties such as neutron absorption cross section to ensure good neutron economy.

In order to establish a design, nuclear analysis must be carried out multiple times to determine the range of parameters that are allowed under the constraints placed on the reactor. In the early stage of development, this is done by examining a simple, crude model which captures the most important features of the reactor. During this process, the nuclear calculations need to interact with other aspects of the reactor, especially thermal-hydraulics. As the process advances, more information is accumulated and more detailed models and codes will be used to narrow down the scope of parameters to come to an optimal reference design that gives best performance within the restricts placed on the reactor [13], [25].

1.5.1 Neutronics Analysis

Activities under the principal matter of neutronics analysis can be put into three categories [13]:

- determination of core criticality and core distributions
- reactivity and control analysis
- depletion analysis

The criticality calculation examines various core parameters to ensure stable operation without ramping up or shutdown, such as fuel enrichment, core layout, and poison load, etc.. One needs to make sure that the reactor holds sufficient reactivity control during the operation lifetime and shutdown. The flux or power distribution is of primary importance, and a flat power map is always preferred to ensure uniform burnup of fuel throughout the reactor core and is used in subsequent thermal-hydraulics and depletion studies. The power distribution is also influenced by the operation time and position since fission products accumulate with burnup and affect the distribution of neutrons. Nowadays the escalating solving capabilities of computers enable the Monte

Carlo method to be applied to simulating the transport processes of neutrons. Monte Carlo basically simulates the neutron interactions in the microscopic level by random sampling: it samples a sequence of neutrons to assemble the actual distribution of states of neutrons, and tracks the history of the random movements and interactions of a neutron from generation to destruction [26]. Some commonly used codes are: Serpent [27], OpenMC, and MCNP.

Reactivity is a parameter used to evaluate the multiplication of neutrons defined as the net neutron production rate:

$$\rho = \frac{neutron\ production - neutron\ loss}{neutron\ production}. \tag{1.1}$$

If:

$\rho > 0$	neutron population is increasing
$\rho = 0$	neutron population is at equilibrium
$\rho < 0$	neutron population is decreasing

An expression of reactivity is given in Section 2.3. Adequate negative reactivity is required to counterbalance the large initial power density at the beginning of operation and to compensate for temperature feedback and fission product buildup, which can be achieved by reactivity devices like control rods and poison. It is important to evaluate core kinetic behaviours and the temperature changes in short time scales with the temperature coefficients of reactivity of fuel and moderator, as well as the density coefficient of coolant and moderator if it is liquid.

The depletion or burnup analysis produces information about fissile elements depletion and fission products accumulation during reactor operation which is needed to determine fuel composition and reactivity. It is carried out by numerous times of multiplication and power distribution calculations over the lifetime. The depletion analysis is closely associated with fuel management which considers fuel loading, refueling, and core arrangement to attain the optimal fuel economy. However, for CNB there is no refuelling arrangement; the reactor is designed to operate for about 20 years without changing the fuel.

1.5.2 Thermodynamics Analysis

Another significant aspect of reactor design is the thermodynamics analysis. The major goals of thermodynamics evaluations are to determine a high specific power to ensure minimal fuel load, a high power density to minimize the core size, and a high coolant outlet temperature to optimize the power conversion efficiency in the secondary loop. In terms of reactor safety analysis, it also needs to ensure the maximum fuel temperature must not exceed the melting point of fuel or a melt-down would occur. Another constraint considered by thermal calculations is the heat transfer rate between fuel/moderator to the coolant, because if the heat flux becomes too high film boiling or dryout might occur, resulting in reduced heat transfer and sudden increase in fuel and clad temperature [13], [25].

In current time the thermophysics study of the reactor can be conducted in finite-element 3D simulating software packages such as ANSYS, STAR-CCM+, and codes like OpenFOAM. In criticality calculations, the thermal model takes the power density distribution from the neutronics code, generates the core temperature map, and then feeds back to the neutronics code which runs the static calculation again until convergence. This procedure is called neutronics/thermal coupling as shown in Figure 1.15. Over the past two decades or so, such schemes used to couple codes of separate physics realms (mono-disciplinary codes) by linearly transferring the output parameters to one another to solve a nonlinearly coupled process, is mathematically called the operator-splitting method (OS) [28].

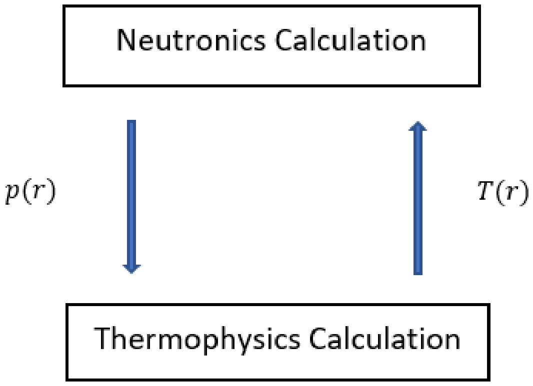

Figure 1.15: Neutronics/thermal coupling. $p(r)$ is power density distribution, $T(r)$ is temperature distribution.

Chapter 2

Reactor Physics

The main reference literature is the course material for Nuclear Reactor Analysis by Dr. Benjamin Rouben at McMaster University. The content is rewritten and rearranged here by the author.

2.1 Neutron Cycle

In a thermal reactor, neutrons are generated in the fast spectrum (a few MeV) in fission events and then slow down thorough collision in the moderator to thermal range (less than 0.6 eV). During this process, neutrons face various interactions with the core materials and not all neutrons can reach to the desired interval of energy. When first created in high energies, they may induce fast fission with fissionable elements like U-238. For the neutrons that survive to lower energies, a portion of them get absorbed by the core materials through resonance capture (1 eV to 0.1 MeV). Finally, neutrons are sufficiently moderated and arrive at the thermal range. Some of them induce fission events with heavy metallic nuclides, while others are lost in non-productive thermal absorptions in fuel and other components. Leakage out of the reactor through diffusion happens for all energies in the spectrum. In order to reduce neutron loss in non-productive events and increase neutron economy, reflectors are added to encompass the reactor core and less absorptive materials are favored as structural materials.

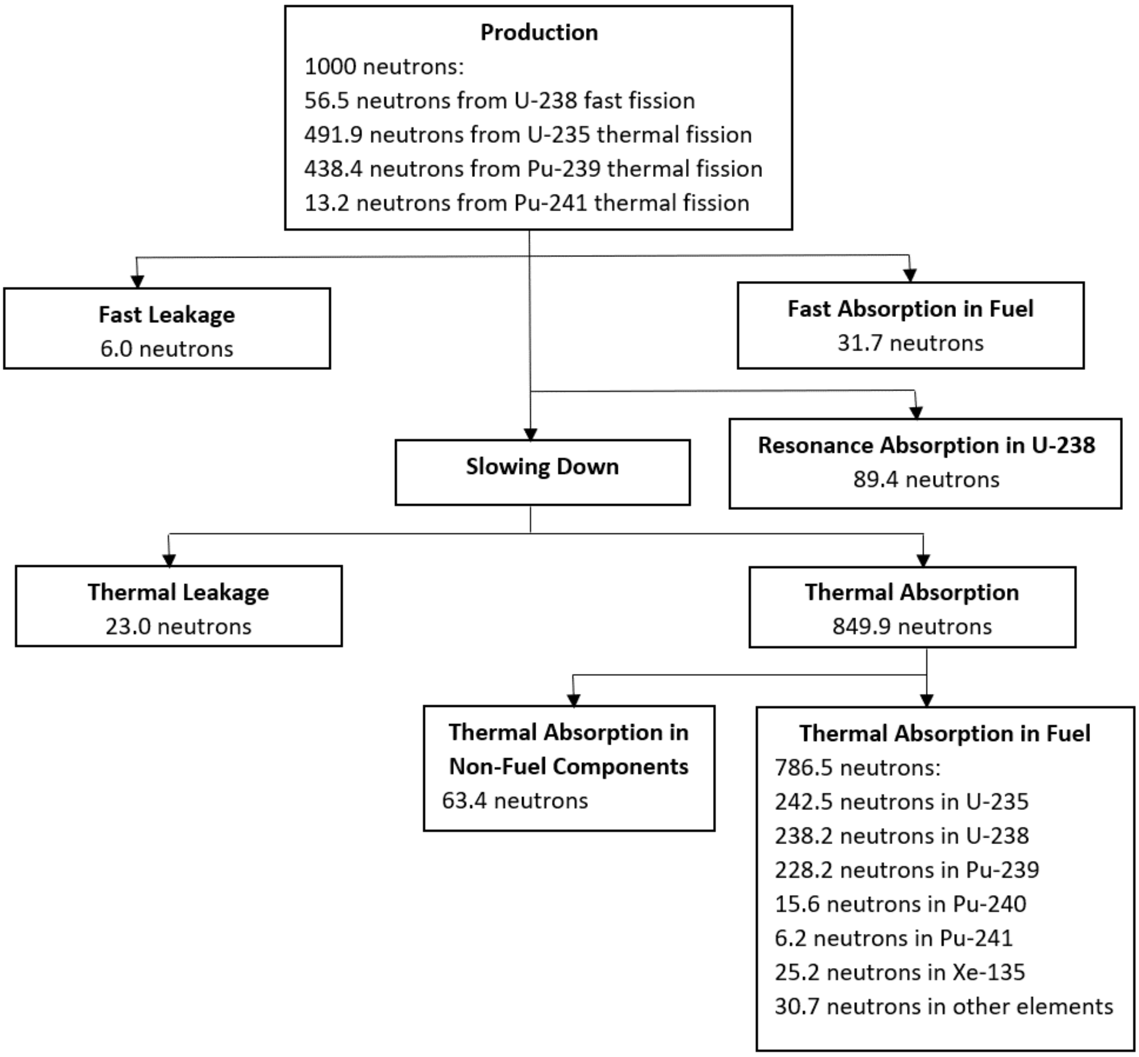

Figure 2.1: Neutron cycle in CANDU-6 equilibrium core, adapted from Ref. [29]. Note the neutron cycle of the CNB is very different than what's shown in this figure.

2.2 Neutron Transport Equation and Diffusion Equation

The time-dependent neutron transport equation describes the rate of change of neutron flux in terms of production and destruction in a differential volume at position $\vec{r}$, direction $\hat{\Omega}$, energy E, and time t:

$$
\begin{aligned}
\overbrace{\frac{1}{v}\frac{\partial\phi(\vec{r},E,\hat{\Omega},t)}{\partial t}}^{①} = {} & \overbrace{\frac{1}{4\pi}S(\vec{r},E,t)}^{②} + \overbrace{\frac{\chi(E)}{4\pi}\int_{E'}\nu\Sigma_{\mathrm{f}}(\vec{r},E',t)\phi(\vec{r},E',\hat{\Omega},t)dE'}^{③} \\
& + \overbrace{\int_{\hat{\Omega}'}\int_{E'}\Sigma_{\mathrm{s}}(\vec{r},E'\rightarrow E,\hat{\Omega}'\rightarrow\hat{\Omega})\phi(\vec{r},E',\hat{\Omega}',t)dE'd\hat{\Omega}'}^{④} \\
& - \overbrace{\Sigma_{\mathrm{t}}(\vec{r},E,t)\phi(\vec{r},E,\hat{\Omega},t)}^{⑤} - \overbrace{\vec{\nabla}\cdot\vec{J}(\vec{r},E,\hat{\Omega},t)}^{⑥}, \qquad (2.1)
\end{aligned}
$$

where

ϕ	neutron flux
$\vec{J}$	neutron current
S	external neutron source
4π	solid angle integral over all 3D directions
χ	neutron energy spectrum
ν	fission neutron yield
Σ_{f}	fission cross section
Σ_{s}	neutron scattering cross section
Σ_{t}	total cross section, defined as $\Sigma_{\mathrm{t}} = \Sigma_{\mathrm{a}} + \Sigma_{\mathrm{s}}$
(1)	rate of change in neutron density written in terms of ϕ
(2)	external neutron source
(3)	fission neutron production
(4)	neutron source scattered into $\vec{r}$, $\hat{\Omega}$, E
(5)	neutron loss through absorption and scattering
(6)	neutron loss through leakage

Using Fick's law, the variable $\hat{\Omega}$ can be eliminated:

$$\vec{J}(\vec{r},E) = -D(\vec{r},E)\vec{\nabla}\phi(\vec{r},E), \qquad (2.2)$$

where D is the diffusion coefficient. This basically states that the direction of overall neutron current of energy E is the direction of the largest decrease of neutron flux of energy E. With Eq. 2.2 the time-dependent angle-integrated neutron diffusion equation can be derived:

$$\begin{aligned}\frac{1}{v}\frac{\partial\phi(\vec{r},E,t)}{\partial t} &= S(\vec{r},E,t)+\chi(E)\int_{E'}\nu\Sigma_{\mathrm{f}}(\vec{r},E',t)\phi(\vec{r},E',t)dE' \\ &\quad+\int_{E'}\Sigma_{\mathrm{s}}(\vec{r},E'\rightarrow E,t)\phi(\vec{r},E',t)dE' \\ &\quad-\Sigma_{\mathrm{t}}(\vec{r},E,t)\phi(\vec{r},E,t)+\vec{\nabla}\cdot D(\vec{r},E,t)\vec{\nabla}\phi(\vec{r},E,t).\end{aligned} \tag{2.3}$$

However, the assumption of Fick's law breaks down at regions of significant inconsistency, such as locations near strong absorbing materials, neutron source, and between structures with large differences in physical properties.

Often the diffusion equation is expressed in one energy group for study and preliminary assessment purposes. Assume the reactor is a homogeneous reactor without external neutron source, and the diffusion coefficient D is a constant independent of space and time. Then the one-group neutron kinetics equation in a homogeneous reactor is:

$$\frac{1}{v}\frac{\partial\phi(\vec{r},t)}{\partial t}=\nu\Sigma_{\mathrm{f}}(t)\phi(\vec{r},t)-\Sigma_{\mathrm{a}}(t)\phi(\vec{r},t)+D\nabla^2\phi(\vec{r},t). \tag{2.4}$$

Here the scattering term disappears because there is only one energy group, no exchanges between energy intervals through collision. The geometrical buckling B^2 is defined as the relative curvature of neutron flux:

$$B^2\equiv-\frac{\nabla^2\phi}{\phi}. \tag{2.5}$$

With B^2 Eq. 2.4 can be rewritten:

$$\frac{1}{v}\frac{\partial\phi(\vec{r},t)}{\partial t}=\nu\Sigma_{\mathrm{f}}(t)\phi(\vec{r},t)-\Sigma_{\mathrm{a}}(t)\phi(\vec{r},t)-DB^2\phi(\vec{r},t). \tag{2.6}$$

The homogeneous finite reactor approximation is equivalent to the so-called "point" approximation of the reactor indicating that there is no change in flux shape (B^2 is constant) only change in flux magnitude, and the corresponding kinetics problem is called "point-kinetics".

2.3 One-group Criticality

If a finite homogeneous reactor can operate at steady state (criticality), then from Eq. 2.6 we get:

$$\nu\Sigma_{\mathrm{f}}\phi(\vec{r})-\Sigma_{\mathrm{a}}\phi(\vec{r})-DB^2\phi(\vec{r})=0, \tag{2.7}$$

which is the neutron balance equation, and

$$\nu\Sigma_\mathrm{f} - \Sigma_\mathrm{a} - DB^2 = 0. \tag{2.8}$$

But often the reactor is not intrinsically critical. Usually we modify core material properties to make the reactor stable instead of changing the geometry:

$$\frac{\nu\Sigma_\mathrm{f}}{k_\mathrm{eff}} - \Sigma_\mathrm{a} - DB^2 = 0, \tag{2.9}$$

and

$$k_\mathrm{eff} = \frac{\nu\Sigma_\mathrm{f}}{\Sigma_\mathrm{a} + DB^2}. \tag{2.10}$$

Here k_eff is the multiplication constant. The standard definition is:

$$k_\mathrm{eff} \equiv \frac{neutron\ production}{neutron\ loss\ (absorption + leakage)}, \tag{2.11}$$

and Eq. 2.10 is consistent with the standard definition. If:

$k_\mathrm{eff} = 1$	the reactor is critical. The rate of production is equal to destruction.
$k_\mathrm{eff} > 1$	the reactor is supercritical. The rate of production is larger than destruction.
$k_\mathrm{eff} < 1$	the reactor is subcritical. The rate of production is less than destruction.

And the reactivity ρ is defined as:

$$\rho = 1 - \frac{1}{k_\mathrm{eff}} = \frac{\nu\Sigma_\mathrm{f} - (\Sigma_\mathrm{a} + DB^2)}{\nu\Sigma_\mathrm{f}}, \tag{2.12}$$

which is the net neutron production rate as discussed in Sec. 1.5.1.

In the case of a critical reactor, i.e. $k_\mathrm{eff} = 1$, the geometrical buckling can be written as :

$$B^2 = \frac{\nu\Sigma_\mathrm{f} - \Sigma_\mathrm{a}}{D}, \tag{2.13}$$

and the neutron balance equation Eq. 2.7 becomes:

$$\nabla^2\phi(\vec{r}) + B^2\phi(\vec{r}) = 0. \tag{2.14}$$

As an example, now examine the solution to this equation for a infinite slab with a constant height h. Let the origin $x = 0$ be placed at the middle of the height. Since this is a one-dimensional problem, the vector $\vec{r}$ reduces to x:

$$\nabla^2\phi(x) + B^2\phi(x) = 0. \tag{2.15}$$

The extrapolation distance d is defined as the distance beyond the reactor where the neutron flux is assumed to be zero. The boundary condition requires the flux to be zero at the extrapolation distance:

$$\phi(\frac{h_{\text{ex}}}{2}) = 0, \tag{2.16}$$

where h_{ex} is the height with extrapolation distance on both sides:

$$h_{\text{ex}} = h + 2d. \tag{2.17}$$

The general solution to Eq. 2.15 is:

$$\phi(x) = A_1 \cos(Bx) + A_2 \sin(Bx). \tag{2.18}$$

The symmetry at $x = 0$ excludes $\sin(Bx)$, and from the boundary condition we have:

$$A_1 \cos(B\frac{h_{\text{ex}}}{2}) = 0. \tag{2.19}$$

There are multiple solutions of B, but keeping in mind that the flux can't be negative the solution can only be:

$$\phi(x) = A_1 \cos(\frac{\pi x}{h_{\text{ex}}}). \tag{2.20}$$

The flux is of cosinusoidal shape along the height of a infinite slab. The coefficient A_1 can be determined from the power generated per unit area of the slab.

2.4 Delayed Neutrons

Delayed neutrons are neutrons produced by the decay of certain fission products, called the “delayed neutron precursors”. Even though the delayed neutrons only take up about 0.6% of all neutrons, they have a significant impact on the kinetics behaviour of reactor.

The average generation time Λ is defined as the average time between the birth of two successive generations. According to this definition we can write the correlation between two successive neutron generations:

$$N(t + \Lambda) = k_{\text{eff}} N(t), \tag{2.21}$$

where $N(t)$ is the neutron population at time t, and k_{eff} is the multiplication constant representing the ratio of neutron populations between two adjacent generations. Subtracting $N(t)$ and dividing by Λ we have:

$$\frac{N(t + \Lambda) - N(t)}{\Lambda} = \frac{k_{\text{eff}} N(t) - N(t)}{\Lambda} = \frac{k_{\text{eff}} - 1}{\Lambda} N(t), \tag{2.22}$$

and

$$\frac{dN(t)}{dt} = \frac{k_{\text{eff}} - 1}{\Lambda} N(t). \tag{2.23}$$

Here Λ is sufficiently small and is regarded as the time differential interval dt. Integrated by both sides Eq. 2.23 becomes:

$$N(t) = N(0) e^{\frac{k_{\text{eff}} - 1}{\Lambda} t}, \tag{2.24}$$

Typically Λ for prompt neutrons is 1 ms (0.001 s). If we look at an example of $k_{\text{eff}} = 1.001$ with a reactivity of 1 mk, Eq. 2.24 gives:

$$N(t) = N(0) e^{t}, \tag{2.25}$$

where t is in seconds. In this case, the reactor would evolve as follows:

1 s	$N = 2.7N(0)$
2 s	$N = 7.3N(0)$
3 s	$N = 20.1N(0)$
4 s	$N = 54.6N(0)$

Such speed is very fast and impossible to stabilize the reactivity. However, with delayed neutrons things would become very different. Due to the long period of their production, the average neutron generation time is dominated by delayed neutrons even if they only count for a small fraction in the total population. With delayed neutrons Λ is approximately 0.1 s compared to 0.001 s in case of prompt neutrons. Substituting into Eq. 2.24 we have:

$$N(t) = N(0) e^{0.01t}, \tag{2.26}$$

and the development of neutron population with a reactivity of 1 mk becomes:

1 s	$N = 1.018N(0)$
2 s	$N = 1.02N(0)$
3 s	$N = 1.03N(0)$
4 s	$N = 1.04N(0)$

which is much slower than if there are only prompt neutrons.

The delayed neutron fraction β is defined as the proportion of delayed neutrons in the total number of neutrons generated per fission event, and let C be the concentration of delayed neutron precursors. Then the coupled one-group kinetics equations with one delayed neutron precursor group can be written in terms of neutron density n:

$$\frac{\partial C}{\partial t} = \nu\beta\Sigma_f v n - \lambda C, \tag{2.27}$$

$$\frac{\partial n}{\partial t} = \nu(1-\beta)\Sigma_f v n - DB^2 v n - \Sigma_a v n + \lambda C, \tag{2.28}$$

where

$\nu\beta\Sigma_f v n$	delayed neutron precursor generation by fission
λC	delayed neutron precursor decay
$\nu(1-\beta)\Sigma_f v n$	prompt neutron production by fission
$DB^2 v n$	neutron out-leakage
$\Sigma_a v n$	neutron absorption

Typical values of the constants are listed in Table 2.1.

Constant	Value
β	0.006
λ/s^{-1}	0.1
Λ/s	0.001

Table 2.1: Typical values of constants related to delayed neutrons for thermal reactors.

2.5 Prompt Jump

Eq. 2.27 and 2.28 can also be written as:

$$\frac{dn}{dt} = \frac{\rho-\beta}{\Lambda} n + \lambda C, \tag{2.29}$$

$$\frac{dC}{dt} = \frac{\beta}{\Lambda} n - \lambda C. \tag{2.30}$$

Here the neutron generation time Λ is:

$$\Lambda = \frac{1}{\nu\Sigma_\mathrm{f}\nu}. \tag{2.31}$$

In case of small reactivity insertion (say $\rho < \frac{\beta}{2}$), the general solutions are:

$$n(t) = n_1 e^{\omega_1 t} + n_2 e^{\omega_2 t}, \tag{2.32}$$

$$C(t) = \frac{\beta n_1}{\Lambda(\lambda + \omega_1)} e^{\omega_1 t} + \frac{\beta n_2}{\Lambda(\lambda + \omega_2)} e^{\omega_2 t}, \tag{2.33}$$

where

$$\omega_1 = \frac{\lambda \rho}{\beta - \rho}, \tag{2.34}$$

$$\omega_2 = \frac{\rho - \beta}{\lambda} \quad (< 0), \tag{2.35}$$

$$n_1 = \frac{\beta}{\beta - \rho}, \tag{2.36}$$

$$n_2 = -\frac{\rho}{\beta - \rho}. \tag{2.37}$$

Substituting the solutions into Eq. 2.32 it becomes:

$$n(t) = \frac{\beta}{\beta - \rho} e^{\frac{\lambda \rho}{\beta - \rho} t} - \frac{\rho}{\beta - \rho} e^{\frac{\rho - \beta}{\Lambda} t}. \tag{2.38}$$

Note that ω_1 has the same sign as ρ and ω_2 is always negative. Algebraically $\omega_1 > \omega_2$, while in absolute values $|\omega_2| \ll |\omega_1|$. Because of the exponential behavior of the solutions, during a sudden reactivity insertion transient the second term will disappear quickly due to the negative sign and large absolute quantity of ω_2 (period $\frac{1}{|\omega_2|}$ is small); the first term will soon be the surviving one and the reactor will evolve with a stable period of $\frac{1}{\omega_1}$. Such phenomenon is called prompt jump or drop depending on the sign of reactivity. The time needed for the algebraically smaller frequencies to die out is called the stable period τ:

$$\tau = \frac{1}{|\omega_1|}. \tag{2.39}$$

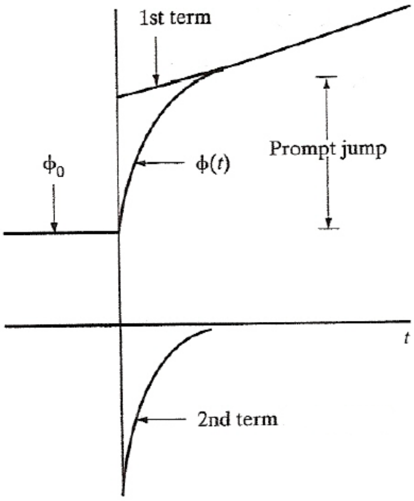

Figure 2.2: Prompt jump, adapted from Ref. [30].

The prompt jump can be derived by three assumptions: 1) the reactor is at steady state before prompt jump, 2) the concentration of delayed neutron precursor doesn't change during the prompt jump, 3) the time derivative at the end of stable period can be regarded as zero. From those assumptions and let subscript ss denote the steady state at the beginning, we can write:

$$0 = \frac{\beta}{\Lambda} n_{\mathrm{ss}} - \lambda C_{\mathrm{ss}}. \tag{2.40}$$

Then the delayed neutron precursor concentration at the initial steady state and during the transient is:

$$C_{\mathrm{ss}} = \frac{\beta n_{\mathrm{ss}}}{\lambda \Lambda}. \tag{2.41}$$

Using assumption 3) and C_{ss} Eq. 2.29 becomes:

$$0 = \frac{\rho - \beta}{\Lambda} n + \lambda \frac{\beta n_{\mathrm{ss}}}{\lambda \Lambda}, \tag{2.42}$$

and the prompt jump can be given:

$$\frac{n}{n_{\mathrm{ss}}} = \frac{\beta}{\beta - \rho}. \tag{2.43}$$

Following a sudden reactivity insertion the neutron population will evolve according to the sign and magnitude of the inserted reactivity. However, the change in neutron population will incur other changes in certain properties of the core, such as temperature, power, coolant and moderator densities, and this will influence the microscopic neutronic processes and further lead to feedback mechanisms to the reactivity. Such effect is called the reactivity feedback, and the parameters used to evaluate the effect is the reactivity coefficients.

2.6 Reactivity Coefficients and Doppler Broadening

Reactivity coefficients are important parameters for nuclear reactors. They are defined as the derivative of reactivity to certain core parameters, reflecting the sensitivity of reactivity to those parameters. Reactivity coefficients have significant implication on the transient behaviours of a reactor when changes in operation conditions happen. Some important reactivity coefficients are:

$\frac{\partial \rho}{\partial T_{\mathrm{f}}}$	fuel temperature coefficient of reactivity (mk/°C)
$\frac{\partial \rho}{\partial M_{\mathrm{d}}}$	moderator density coefficient of reactivity (mk/(g/cm^3))
$\frac{\partial \rho}{\partial C_{\mathrm{d}}}$	coolant density coefficient of reactivity (mk/(g/cm^3))

The fuel temperature coefficient of reactivity indicates the variation in the absorbing ability of fuel when temperature changes, mainly through resonance capture and Doppler broadening. Resonance capture happens to very specific neutron energies at the intermediate range (approximately 1 eV to 0.1 MeV) with very high absorption cross sections (Figure 2.3). The nuclei in fuel are constantly oscillating in a random manner regarding to the fuel temperature. When temperature increases, the random movement of the nuclei becomes intense and the range of the relative speeds between neutrons and the nuclei become larger. As a result, there will be higher possibilities for those neutrons slightly off the exact resonance energies to be captured in collision with the nuclei; in other words, the absorption cross section is broadened but lowered since the neutrons with the exact energies also seem to be off to the nuclei. However, the total area under the cross section curve remains the same (Figure 2.4) [30].

Then, because the cross section reduces, the average neutron flux increases since there is less absorption, which in turn brings up the amount of absorption. The overall effect is that the absorption is increased at higher temperatures. Consequently, the fuel temperature coefficient is negative, providing negative feedback and bringing the power down when temperature goes up. However, it gives positive reactivity when temperature drops such as during reactor shutdown. The feedback mechanisms must be considered and counterbalanced by reactivity devices to ensure safe shutdown.

For LWRs where coolant is moderator, a decrease in coolant density is equivalent to a decrease in moderator density. Therefore the coolant density coefficient is positive, which means when coolant density drops negative reactivity is added to the reactor due to the reduced moderating effect in the coolant. While for pressure tube reactors like CANDU, the coolant and moderator are separated and need to be considered respectively.

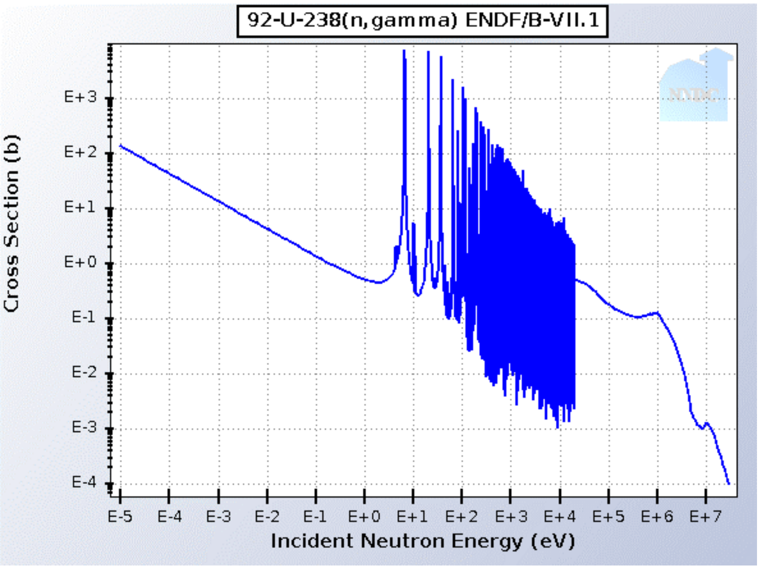

Figure 2.3: Radiative capture cross section spectrum of U-238.

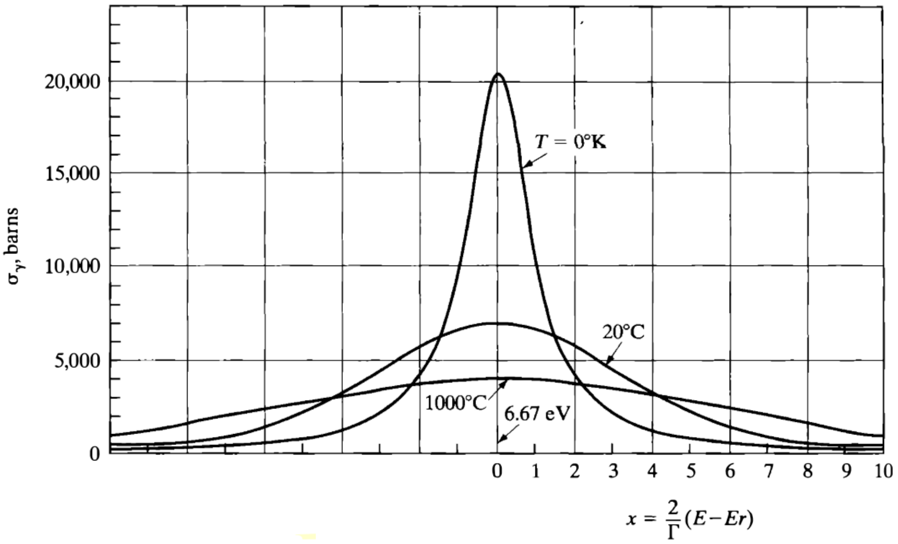

Figure 2.4: Doppler broadening of the capture cross section of U-238 at 6.67 eV [30]. Γ is the resonance width, and E_{r} is the resonance energy.

Chapter 3

Core Structure and Heat Pipe Design

For the Canadian Nuclear Battery, the name “Nuclear Battery” highlights its passive safety features, solid state system, and the graphite core block of high heat capacity as a storage cell. Throughout the life time, no fuel is added or removed from the reactor, which means skilled operation of fuel handling is not required. Such feature enhances the safety capacity of the reactor to avoid dispersion of radioactivity and fission products outside the reactor.

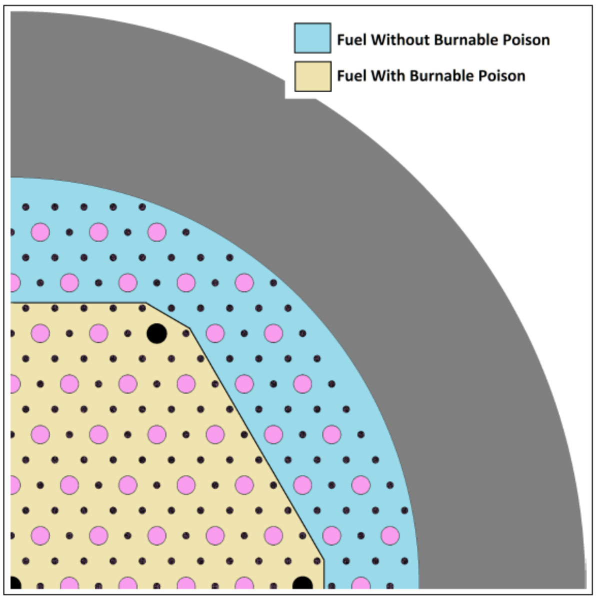

Figure 3.1: Two-zone layout of the core. The small black dots are fuel rods, the large pink dots are heat pipes, and the large black dots indicate control rods. Produced by another member in the team, Sameer Reodikar [31].

The fuel uses U-235 in the form of uranium dioxide, and exists in the reactor as TRISO particles. The TRISO coated fuel particles are bonded by a graphite matrix and formed into cylindrical segment rods then stacked together to form a fuel rod of 1.5 m long. To maintain steady operation throughout the life time, the burnalble poison erbium-oxide (Er_2O_3) is added into the fuel rods in the central region to suppress power fluctuation and smooth power distribution. A two-zone layout of the core is consequently formed (Figure 3.1): in the inner region, TRISO particles together with Er_2O_3 are integrated into fuel rods, while in the outer region the fuel rods only contain TRISO fuel particles.

Control rods and the shutoff rods of boron carbide serve as reactivity control devices during the operation and shutdown. A top, bottom, and side reflector of graphite are placed on top of the moderator block to enhance neutron economy. The reactor is designed to be placed underground, adding an additional barrier to fission product dispersion (Figure 3.2) and aboveground interruptions.

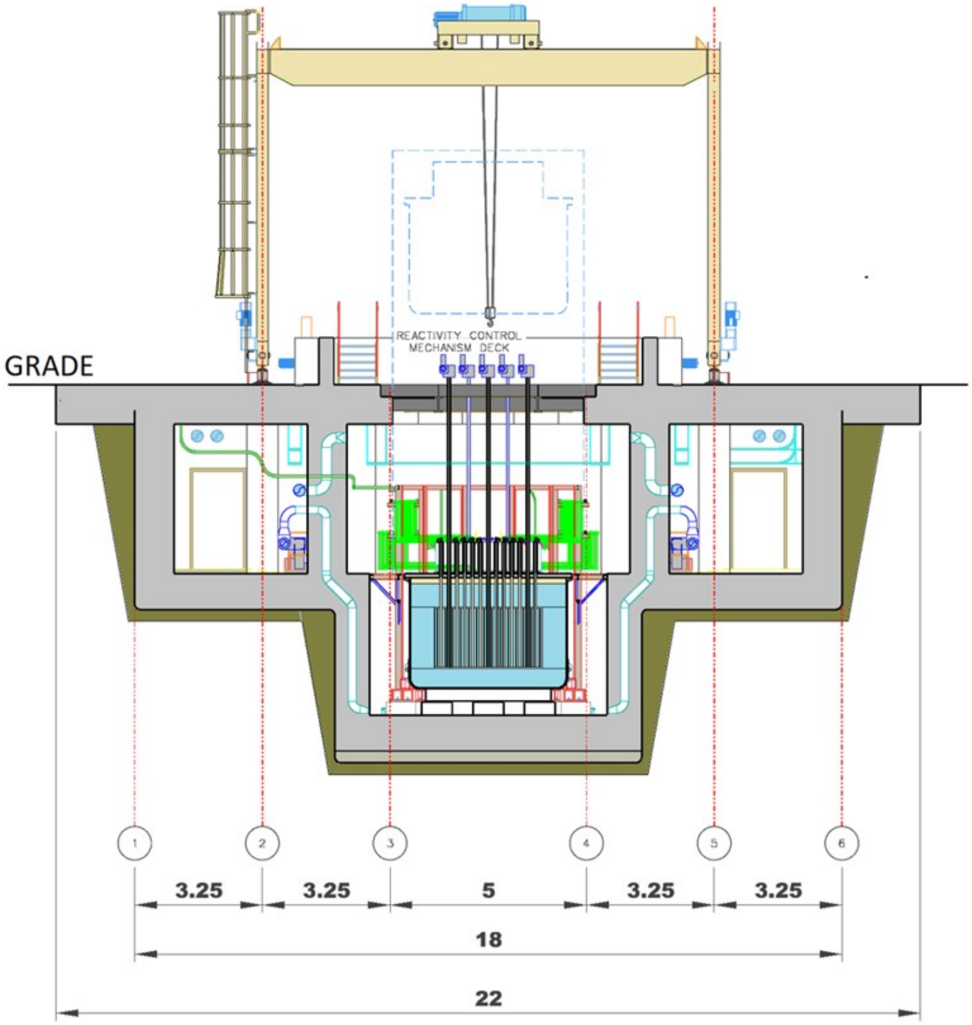

Figure 3.2: Layout of the Canadian Nuclear Battery reactor plant. Unit: [m]. Figure courtesy from Dunedin, Inc..

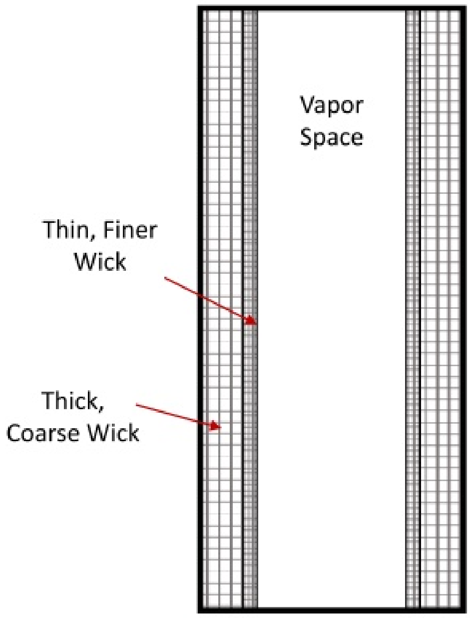

Figure 3.3: Schematic of the structure of the wick, produced by Advanced Cooling Technologies, Inc..

Total length	3.0 m	Evaporator length	1.5 m
Adiabatic section length	0.6 m	Condenser length	0.75 m
Buffer gas space, end caps	0.15 m	Outside diameter	50.8 mm
Tube wall thickness	0.7 mm	Wick thickness	0.7 mm
Vapour flow diameter	48.0 mm	Vapour flow area	18.1 cm^2
Evaporator surface area	2262 cm^2	Condenser surface area	1131 cm^2

Table 3.1: Dimensions of the heat pipe design.

Pipe wall, end fittings	Nb-1 wt% Zr alloy (stainless steel)
External O_2 and H_2 resistant coating	Zinc
Wick structure	Nb-1 wt% Zr alloy (stainless steel)
Working fluid	Potassium (sodium)

Table 3.2: Reference heat pipe materials. The substances inside the brackets indicate other choices of materials for the heat pipe components.

Alkali heat pipes penetrate the top reflector and the graphite moderator to extract thermal energy to the secondary coolant loop. Table 3.1 and Table 3.2 present the dimensions and materials of the heat pipe design. The heat pipe has a thin wall of 0.7 mm thickness of niobium alloy or stainless steel which ensures high-temperature resistance. A composite wick of 0.7 mm thick adhering to the pipe wall provides capillarity needed to pump the liquid from upper condenser region to the lower evaporator region in addition to gravity, performs to uniform the liquid distribution on the inner surface of the pipe wall, and also acts as a protection layer of the liquid content from the fast reversely-moving vapour (Fig. 3.3).

There is approximately a 150 grams of potassium in a heat pipe, most of which fills and penetrates the wick, while only less than a gram of potassium is in the vapour space.

The pressure inside the heat pipes is less than the atmospheric pressure at design operating temperatures. A helium cover gas is applied to improve heat transfer between the heat pipe condenser and the secondary loop (the vaporizer), and maintain an inert environment inside the core [24]. Note that there is no covering gas between heat pipes and moderator/reflector blocks inside the reactor core.

Reactor power	2400 kW(t)
Orientation	vertical (gravity assist)
Power per pipe	15.1-16.6 kW
Max radial heat flux	9.76 W/cm^2
Max axial heat flux	917 W/cm^2
Assumed vapour temperature	500 °C
Toluene temperature at vaporizer exit	383 °C
Temperature increase in toluene	158 °C
Total heat removed from vaporizer	9720 W

Table 3.3: Nominal operating conditions for the heat pipes. The total heat removed from vaporizer is determined by the heat transfer efficiency between the heat pipe condenser and the vaporizer where toluene absorbs heat and turns into vapour.

Chapter 4

Heat Pipe Limits Analysis

The maximum power that a heat pipe can attain is limited by a number of factors, resulting in five limitations: sonic limit, boiling limit, viscous limit, entrainment limit, and capillary limit. Determining the heat transfer limits is important to set the desired operation margin of the heat pipe, and may have indications on the configuration of the reactor core. In this chapter, various heat pipe limits and theories are discussed in detail and the calculated limit curves are compared with those provided by the vendor Advanced Cooling Technology, Inc..

4.1 Sonic Limit

Sonic limit is reached when the vapour accelerates to the speed of sound at the end of the evaporator section, i.e. Mach number Mach $= \frac{U}{C_{\mathrm{son}}} = 1$ at the end of evaporator. Here the vapour is said to be "choked", which means its velocity cannot exceed the sonic speed and the maximum heat flux is thus attained. Sonic limit is usually prominent in liquid metal heat pipes under startup or low temperature conditions when the vapour density is low [32], and according to the formula of heat flux carried by the vapour $q = L\rho_{\mathrm{v}}U$, the vapour velocity has to increase to sustain the same amount of heat flux.

Equations have been developed to calculate the sonic limit. One is derived by Chi [33] by assuming 1) the vapour is an ideal gas, 2) inertial effects dominate, and 3) frictional effects can be neglected [32]. These assumptions are reasonable since sonic limit usually occurs when the vapour density is low and the velocity is high [33], [34]. The equation is expressed as:

$$Q = L\rho_0 A_{\mathrm{v}} \sqrt{\frac{\gamma R_{\mathrm{g}} T}{2(\gamma + 1)}}. \tag{4.1}$$

$L(T)$	latent heat of vaporization, decreases with temperature

$\rho_0(T)$	stagnation density of vapour, taken to be the saturation density at a given temperature, increases with temperature
$\gamma(T)$	specific heat ratio defined as $\frac{c_\mathrm{p}}{c_\mathrm{v}}$, dimensionless, decreases with temperature
A_v	cross-section of vapour flow
R_g	specific gas constant defined as universal gas constant R divided by the molar mass M of the vapour

The parameters should be evaluated at the exit of the evaporator section except ρ_0, which should be taken as the stagnation density of vapour. The notation (T) means the variable is dependent on temperature, and $\sqrt{\gamma R_\mathrm{g} T}$ is the standard expression of speed of sound C_son for an ideal gas:

$$C_\mathrm{son} = \sqrt{\gamma R_\mathrm{g} T}. \tag{4.2}$$

From assumption 1) we get:

$$\frac{P_0}{\rho_0 T_0} = \frac{P}{\rho_\mathrm{v} T} \tag{4.3}$$

where P, T and ρ_v denote the pressure, temperature, and density of vapour generally; the subscript 0 refers to the beginning of evaporator where the vapour velocity is null and also the stagnation state of vapour. The term $\sqrt{2(\gamma+1)}$ in Eq. 4.1 comes from the conservation of momentum and energy of an ideal gas [35]:

$$P_0 = P + \rho_\mathrm{v} U^2, \tag{4.4}$$

$$\dot{m} c_\mathrm{p} T_0 = \dot{m}(c_\mathrm{p} T + \frac{U^2}{2}), \tag{4.5}$$

where P_0 and T_0 are the pressure and temperature at the evaporator entrance (the beginning of evaporator) respectively. These two equations can also be formulated as:

$$\frac{P_0}{P} = 1 + \gamma Mach^2, \tag{4.6}$$

$$\frac{T_0}{T} = 1 + \frac{\gamma - 1}{2} Mach^2, \tag{4.7}$$

remembering that $c_\mathrm{p} = \frac{\gamma}{\gamma - 1}$, and $\dot{m} = A_\mathrm{v} \rho_\mathrm{v} U$. When $Mach = 1$ at the evaporator exit:

$$\frac{P_0}{P} = \gamma + 1, \tag{4.8}$$

$$\frac{T_0}{T} = \frac{\gamma + 1}{2}, \tag{4.9}$$

and γ is typically between 1 and 2. For potassium, at 800 K, $\sqrt{2(\gamma+1)}$ equals to 2.3.

Substituting Eq. 4.6 and Eq. 4.7 into Eq. 4.3, the stagnation density is to be expressed as:

$$\frac{\rho_0}{\rho_{\mathrm{v}}} = \frac{1+\gamma Mach^2}{1+\dfrac{\gamma-1}{2}Mach^2}. \tag{4.10}$$

When $Mach = 1$ at the evaporator exit:

$$\frac{\rho_0}{\rho_{\mathrm{v}}} = 2, \tag{4.11}$$

which means when sonic limit is reached at the end of evaporator, the density there is half of the stagnation density at the beginning of the section.

Another expression is developed by Busse [36] by assuming isothermal dry vapour:

$$\frac{P}{\rho_{\mathrm{v}}} = \frac{P_0}{\rho_0} = \frac{RT_0}{M}. \tag{4.12}$$

Again the subscript 0 refers to the beginning of the evaporator section. By solving $\dfrac{dq}{dP} = 0$ we get a formula for sonic limit:

$$Q = 0.474 \times LA_{\mathrm{v}}\sqrt{\rho_0 P_0}. \tag{4.13}$$

$L(T)$	latent heat of vaporization, decreases with temperature
$\rho_0(T)$	stagnation density of vapour, increases with temperature
$P_0(T)$	stagnation pressure of vapour, increases with temperature
A_{v}	cross-section of vapour flow

Busse observed similar relationships presented in Eq. 4.8, 4.9, and 4.11. The vapour pressure at the evaporator exit is roughly half of the pressure at the beginning of evaporator P_0 when sonic limit is reached [36], and according to Eq. 4.12, the density at the evaporator exit is about half of ρ_0 as well. To get to T from P Eq. 4.12 is needed.

If we simply use:

$$Q = L\dot{m} = L\rho_{\mathrm{v}}A_{\mathrm{v}}U, \tag{4.14}$$

where $U = C_{\mathrm{son}}$. The parameters should be evaluated at the end of evaporator where sonic limit is reached. The vapour velocity U is dependent on the input power and constrained by the maximum power the heat pipe can reach at a given temperature, so U is implicitly related to T.

4.2 Boiling Limit

Nucleate boiling occurs when a certain liquid superheat is reached, which brings down the local thermal conductivity and can cause damage to the heat pipe. The temperature difference between the liquid on the pipe wall and the liquid far from the wall must verify the Laplace equation:

$$P_{\mathrm{b}} - P_{\mathrm{l}} = \frac{2\sigma}{r_{\mathrm{b}}}, \tag{4.15}$$

where P_{b} and r_{b} are the pressure and radius of a bubble respectively. By integrating the Clausius-Clapeyron equation, which describes the relationship between liquid temperature and its vapour pressure, the corresponding superheat needed to attain this pressure difference in a wick is calculated to be [37]:

$$\Delta T_{\mathrm{boil}} = \frac{2\sigma T_{\mathrm{inf}}}{L\rho_{\mathrm{v}}}(\frac{1}{r_{\mathrm{b}}} - \frac{1}{r_{\mathrm{eff}}}), \tag{4.16}$$

where T_{inf} is the liquid temperature far from the wall and is assumed to be equal to the vapour temperature, r_{eff} is the effective radius of the wick pores which depends on the dimension of the pores and the wetting angle of the liquid on the wick [18]. Applying the Fourier's law to a cylindrical pipe, the heat transfer rate is found as:

$$Q = 2\pi l_{\mathrm{eva}}\lambda\|\vec{\nabla}T\| = 2\pi r l_{\mathrm{eva}}\lambda\frac{dT}{dr}, \tag{4.17}$$

where r is the radial coordinate, l_{eva} is the length of evaporator, and λ is the thermal conductivity. For a wick filled with liquid, we have:

$$\lambda = poro_{\mathrm{rad}}\lambda_{\mathrm{wick}} + (1 - poro_{\mathrm{rad}})\lambda_{\mathrm{l}}. \tag{4.18}$$

Here $poro_{\mathrm{rad}}$ is the porosity of the wick, λ_{wick} is the thermal conductivity of wick, and λ_{l} is the thermal conductivity of liquid. Integrating from the radius of vapour space r_{v} to the inner radius of pipe wall r_{i} yields [18]:

$$Q = \frac{2\pi l_{\mathrm{eva}}\lambda\Delta T_{\mathrm{boil}}}{\ln\left(\frac{r_{\mathrm{i}}}{r_{\mathrm{v}}}\right)}. \tag{4.19}$$

The dependencies on temperature of variables contained in Eq. 4.19 are:

$\lambda(T)$	thermal conductivity of wick, increases with temperature
$\rho_{\mathrm{v}}(T)$	density of vapour inside the bubble, taken to be the saturation density, increases with temperature
$\sigma(T)$	surface tension of liquid, decreases with temperature

$L(T)$	latent heat of vaporization of the liquid, decreases with temperature

Otherwise the quantities are constants.

4.3 Entrainment Limit

Entrainment limit is reached when the drag force exerted by vapour to the liquid is strong enough to tear the liquid out of the wick. This may cause dryout and decrease of heat pipe power. The relative magnitude of the drag force to the surface tension force that holds liquid in the wick is characterized by the Weber number We:

$$We = \frac{2r_{\mathrm{h,s}}\rho_{\mathrm{v}}U^2}{\sigma}, \tag{4.20}$$

where $r_{\mathrm{h,s}}$ is the hydraulic radius of the wick, defined as:

$$r_{\mathrm{h,s}} = \frac{2A_{\mathrm{s}}}{C_{\mathrm{s}}}, \tag{4.21}$$

where A_{s} is the area and C_{s} the wetted perimeter of individual surface pores of the wick. For our wick design $r_{\mathrm{h,s}}$ is the radius of the pores in the inner layer of wick (adjacent to vapour). When $We = 1$ at the area where the velocity is largest, usually at the evaporator exit, the entrainment limit is considered reached [32]. Equating Eq. 4.20 to 1 and substituting into Eq. 4.14, we get the expression for entrainment heat transport limit:

$$Q = LA_{\mathrm{v}}\sqrt{\frac{\sigma\rho_{\mathrm{v}}}{2r_{\mathrm{h,s}}}}. \tag{4.22}$$

The variables that changes with temperature are:

$L(T)$	latent heat of vaporization
$\sigma(T)$	surface tension
$\rho_{\mathrm{v}}(T)$	density of vapour, evaluated at the end of evaporator

4.4 Capillary Limit

The small pores of the wick provide a pressure difference between the vapour and the liquid by capillarity, pumping the liquid from the condenser to the evaporator. The maximum pressure difference that can be achieved this way is:

$$\Delta P_{\mathrm{cap,max}} = \frac{2\sigma}{r_{\mathrm{eff}}}, \tag{4.23}$$

where r_{eff} is the effective radius of wick.

Capillary limit is the main restricting factor of heat pipe power. To be able to pump the liquid to the evaporator, the capillary pressure must verify:

$$\Delta P_{\text{cap,max}} \geq \Delta P_{\text{vis}} + \Delta P_{\text{i}} + \Delta P_{\text{l}} + \Delta P_{\text{z}}, \tag{4.24}$$

where ΔP_{vis} is the viscous vapour pressure drop, ΔP_{i} is the inertial pressure drop, ΔP_{l} the viscous liquid pressure drop, and ΔP_{z} the hydrostatic pressure drop. These pressure drops are integrated over the length of the heat pipe. ΔP_{vis} and ΔP_{l} are taken as positive. ΔP_{i} is positive in the condenser, negative in the evaporator, the sum always being positive. Determined by the tilt angle of the heat pipe, ΔP_{z} can be positive (evaporator higher than condenser) or negative (condenser higher than evaporator). In our case it is negative and the heat pipe is placed vertically.

Solving Eq. 4.24 at its equality for velocity by assuming the capillary pressure can just provide the pressure difference needed to pump liquid to evaporator despite of other pressure drops, and by applying $Q = L\dot{m} = L\rho_{\text{v}}A_{\text{v}}U$, the heat pipe power at capillary limit can be calculated. Note that here the velocity U is the maximum velocity in the adiabatic section, which is discussed later in Sec. 4.5.

4.4.1 Pressure Drops of Vapour

Set $x = 0$ at the beginning of the evaporator. The vapour pressure is calculated by:

$$P_{\text{v}}(x + dx) = P_{\text{v}} - dP_{\text{vis}} - dP_{\text{i}}, \tag{4.25}$$

where dP_{vis} is the viscous vapour pressure drop and dP_{i} the inertial vapour pressure drop.

According to Fanning equation, the viscous vapour pressure drop due to friction with the wick is written as:

$$dP_{\text{vis}} = \tau \cdot \frac{\textit{contact area}}{\textit{cross}-\textit{sectional area}} = \tau \cdot \frac{2\pi r_{\text{v}} dx}{\pi r_{\text{v}}^2} = \tau \cdot \frac{2dx}{r_{\text{v}}}, \tag{4.26}$$

where r_{v} is the radius of the vapour space, τ is the sheer stress at the wick. The Fanning friction factor is defined as:

$$f = \frac{\tau}{\rho_{\text{v}} \cdot \frac{U^2}{2}}, \tag{4.27}$$

then Eq. 4.26 can be written as:

$$dP_{\text{vis}} = f\rho_{\text{v}}U^2\frac{dx}{r_{\text{v}}} \tag{4.28}$$

The friction factor shows a dependency on the Reynolds number:

$$f = \begin{cases} \frac{16}{Re} \quad if\ Re < 2000 \\ \\ \frac{0.079}{Re^{0.25}} \quad if\ Re > 2000 \end{cases} \qquad \text{where } Re = \frac{\rho_{\text{v}} U d}{\mu_{\text{v}}}. \tag{4.29}$$

Another expression of f makes correction to incompressible flow when the Mach number is greater than 0.2 [33]:

$$f_{\text{c}} = f \cdot (1 + \frac{\gamma - 1}{2} Mach^2)^{-\frac{3}{4}}. \tag{4.30}$$

Dependencies on temperature:

$\rho_{\text{v}}(T)$	density of vapour, increases with temperature
$\mu_{\text{v}}(T)$	vapour viscosity, increases with temperature
$\gamma(T)$	vapour specific heat ratio, decreases with temperature
$C_{\text{son}}(T)$	contained in the $Mach$ number, increases with temperature

Since we are looking at the maximum power the heat pipe can achieve, usually $Mach > 0.2$, and therefore the corrected expression f_{c} is used.

The inertial pressure drop is related to the radial Reynolds number which characterizes the ratio of the rate of mass injection or removal to the viscous effect:

$$Re_{\text{r}} = \frac{1}{2\pi\mu_{\text{v}}} \frac{d\dot{m}}{dx}, \tag{4.31}$$

where $\dot{m}$ is the axial mass flow.

For inertial pressure drop, Cotter [38] developed a first order approximation for a laminar incompressible flow in a cylindrical pipe by assuming a uniform mass injection or removal rate on the length dx:

$$\frac{dP_{\text{i}}}{dx} = \begin{cases} \frac{6\mu_{\text{v}}\dot{m}Re_{\text{r}}}{\pi\rho_{\text{v}}r_{\text{v}}^4} \quad if\ \left|Re_{\text{r}}\right| < 1 \\ \\ \frac{S\dot{m}}{4\rho_{\text{v}}r_{\text{v}}^4}\frac{d\dot{m}}{dx} \quad if\ \left|Re_{\text{r}}\right| > 1 \end{cases}$$

$$\text{where } S = \begin{cases} 1 \quad \text{in evaporator section} \\ \frac{4}{\pi^2} \quad \text{in condenser section} \end{cases}$$

The difference of S between the evaporator and the condenser stems from the different radial distributions of the axial velocity: it is parabolic in the evaporator where the vapour is injected, and cosinusoidal in the condenser where the vapour is removed. For high heat transfer heat pipes, $\left|Re_{\mathrm{r}}\right| > 1$ at evaporator and condenser ($\left|Re_{\mathrm{r}}\right| = 1$ at the adiabatic section because the vapour mass flow doesn't change here), which is the case for the heat pipe design investigated in this research, only $\frac{4}{\pi^2} \approx 40\%$ of the pressure loss by inertial effect is recovered in the condenser [18].

Variables dependent on temperature are:

$\rho_{\mathrm{v}}(T)$	density of vapour
$\mu_{\mathrm{v}}(T)$	vapour viscosity

4.4.2 Pressure Drops of Liquid

Here let $x = 0$ at the end of the condenser since the vapour and liquid flow in opposite directions. The liquid pressure is calculated by:

$$P_{\mathrm{l}}(x + dx) = P_{\mathrm{l}}(x) - dP_{\mathrm{l}} - dP_{\mathrm{z}}, \tag{4.32}$$

where dP_{l} and dP_{z} are the viscous liquid pressure drop and hydrostatic pressure drop respectively. The viscous liquid pressure drop can be evaluated with Darcy's law for a fluid flowing through a porous media:

$$dP_{\mathrm{l}} = \frac{\mu_{\mathrm{l}}\dot{m}}{\rho_{\mathrm{l}} A_{\mathrm{l}} k} dx. \tag{4.33}$$

Here,

$\mu_{\mathrm{l}}(T)$	liquid viscosity
$\rho_{\mathrm{l}}(T)$	liquid density
k	permeability of wick
A_{l}	liquid flow cross-section area

The hydrostatic pressure drop is simply expressed as:

$$dP_{\mathrm{z}} = -\rho_{\mathrm{l}} g \sin\theta dx. \tag{4.34}$$

In the case of CNB, the condenser is above the evaporator and $\theta = 90^\circ$ (gravity assist).

There is another power limit called the viscous limit, which mainly occurs at low temperatures and fluids with high viscosities [18]. The potassium heat pipe design for

CNB is targeted at temperatures around 500 °C, and the wick of the heat pipe provides corrugation channels as flow passages. Thus the viscous limit is neglected in this research.

4.5 Velocity Profile

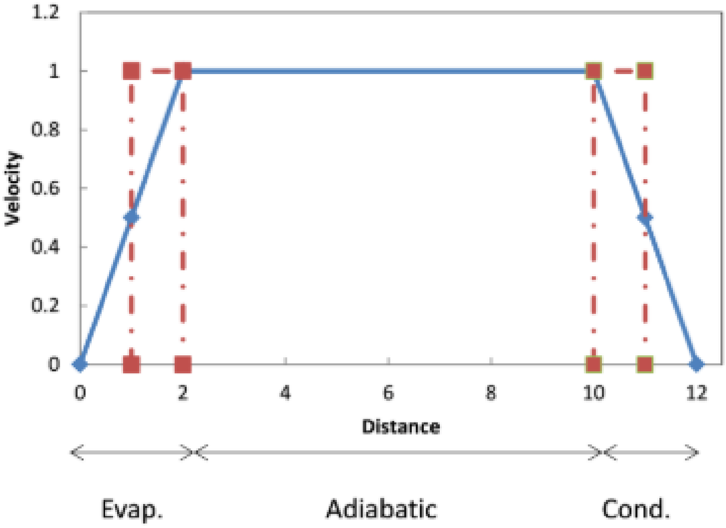

Figure 4.1: Velocity profile along a heat pipe. From ACT website [39].

Fig. 4.1 shows an approximate profile of vapour velocity. Along the evaporator, vapour is generated and accelerated, and the energy flow carried by the vapour increases until it arrives at the adiabatic section, where the velocity and energy flow remain at their maximums (neglect frictional effects). Then in the condenser, vapour gradually slows down and gives up its energy to the secondary loop by condensation. For the heat pipe design of CNB, the adiabatic section is short which means the velocity remain at its maximum for a shorter period, but this doesn't affect the utilization of this assumed velocity profile since it is already an approximation to the actual distribution and the frictional effects are still neglected.

To compensate for the varying velocity at the evaporator and condenser region, an effective length l_{eff} is taken as:

$$l_{\text{eff}} = \frac{l_{\text{eva}}}{2} + l_{\text{adi}} + \frac{l_{\text{con}}}{2}. \tag{4.35}$$

Along this effective length, the full velocity at the adiabatic section is used to calculate various pressure drops [39], except the inertial vapour pressure drop where the change in vapour flow should be counted along the evaporator and condenser. In this report l_{eff} is taken as the gravity assist length 1.875 m in the update correspondence from the vendor ACT (l_{eff} is 1.725 m from Eq. 4.35). The full velocity at the adiabatic region is calculated as:

$$U = \frac{Q}{L\rho_{\mathrm{v}}A_{\mathrm{v}}}. \tag{4.36}$$

4.6 Results and Discussion

l_{eva}/m	l_{adi}/m	l_{con}/m	l_{eff}/m	r_{v}/m	r_{i}/m	A_{v}/m^2	R/(J/K·mol)
1.5	0.6	0.75	1.875	0.024	0.0247	18.1e-4	8.31

Table 4.1: Table of constants

Table 4.1 lists the some of the dimensions of the heat pipe and constants used in calculation; for the variables please refer to the appendix. Vapour is assumed to be generated in saturation state at the beginning of the evaporator, which means the stagnation vapour density and pressure can be regarded the same with the saturation density and pressure as stated before, i.e., $\rho_0 = \rho_{\mathrm{s}}$ and $P_0 = P_{\mathrm{s}}$. Additionally, the heat pipe is designed to operate at temperatures around 500 °C, so the focus of examination of the power limits should be in this range.

4.6.1 Sonic Limit

Equation	Sonic Limit /kW
Busse	26
Chi	31
$Q = L\rho_{\mathrm{v}}A_{\mathrm{v}}U$	34

Table 4.2: Sonic limit at 800 K (527 °C) calculated with different equations. Note the power calculated by $Q = L\rho_{\mathrm{v}}A_{\mathrm{v}}U$ uses experimental sonic speed values.

The sonic limit at 800 K (527 °C) is calculated to be as shown in Table 4.2. The sonic limit evaluated with Chi's equation is 5 kW higher than that with Busse's equation, and the value from the formula $Q = L\rho_{\mathrm{v}}A_{\mathrm{v}}U$ (Eq. 4.14) is 8 kW higher than that from Busse's. Since Buss's equations gives the lowest and most conservative value of the sonic limit, it is adopted as the final equation for sonic limit. The curves drawn by the equations are shown in Fig. 4.2.

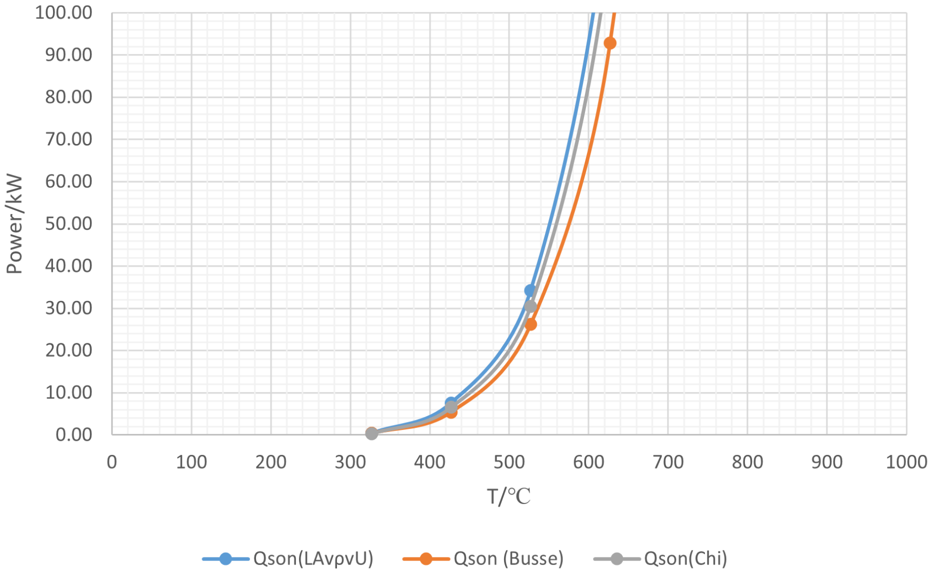

Figure 4.2: Sonic limit of the heat pipe calculated with various equations. The data of the calculated sonic limit at seven temperatures as well as other limits shown in the following sections can be found in Appendix A.

4.6.2 Boiling Limit

r_b/m		r_{eff}/m	ΔT_{boil}/K	Q/kW
2.54e-7	r_{po}	1.0e-4	6983	N/A
	r_{pi}	1.25e-5	6858	N/A
	d	5.0e-5	6965	N/A
2.54e-5	r_{po}	1.0e-4	52	735
	r_{pi}	1.25e-5	<0	N/A
	d	5.0e-5	34	484

Table 4.3: Boiling limit at 800 K (527 °C).

The wick of the heat pipe has a two-layer structure. In Table 4.3, r_{po} and r_{pi} refer to the pore radius of the outer wick and the inner wick respectively, and d is the depth of the individual crosshatch channels on the inside surface of the tube wall. Due to lack of information, several values of parameters are applied. Here r_{eff} is taken as r_{po}, r_{pi}, and d. The radius of the bubble is chosen from a range of 2.54×10^{-7} m to 2.54×10^{-5} m

[32].

It is found that the superheat ΔT_{boil} needed to attain nucleate boiling is either too high to achieve or even negative; when ΔT_{boil} is negative it means a bubble of the radius 2.54×10^{-5} m cannot form in a wick with the effective radius of r_{pi}. The boiling limit is either too high or irrelevant in our case, and is therefore neglected further on.

4.6.3 Entrainment Limit

	$r_{\text{h,s}}$/mm	Entrainment Limit/kW
r_{pi}	0.0125	32
$0.42r_{\text{po}}$	0.042	21

Table 4.4: Entrainment limit at 800 K (527 °C).

The hydraulic radius of the wick $r_{\text{h,s}}$ is chosen to be r_{pi} and $0.42r_{\text{po}}$ respectively. The value of $0.42r_{\text{po}}$ comes from the effective radius of the sintered wick structure [40]:

$$r_{\text{eff}} = 0.21 d_{\text{s}}, \tag{4.37}$$

where d_{s} is the sphere diameter of a sintered wick, and is here taken to be the diameter of the pores on the outside layer of the wick. Actually this equation doesn't apply to the two-layer wick structure for the heat pipe design of CNB, but since we want to approximate and figure out ACT's results, and the entrainment limit calculated with this r_{eff} value is almost the same to that of ACT (21 kW at 527 °C), it is thus included here as reference. Remember that the vapour density at the exit of evaporator is found through Eq. 4.10, where ρ_0 is taken to be the saturation density at 527 °C.

Finally r_{eff} is chosen to be 0.0125 mm. The limit curve is shown in Fig. 4.3.

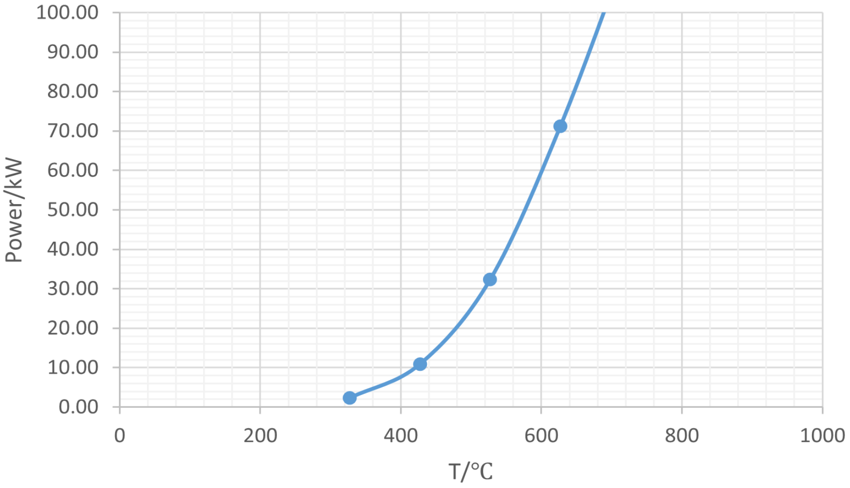

Figure 4.3: Entrainment limit, $r_{\mathrm{h,s}} = 0.0125$ mm.

4.6.4 Capillary Limit

r_{eff}/mm	k	σ/(N/m)	Capillary Limit/kW
0.1	5e-9	0.0862	29
0.05			31

Table 4.5: Capillary limit at 800 K (527 °C).

Capillarity is provided by the crosshatch channels on the inside surface of the pipe wall, and the r_{eff} here is thus associated with the dimension of this structure.

For a rectangular groove, when the wetting angle is zero for maximum capillarity and the groove depth is greater than half of the groove width, it can be proved that the effective radius of the groove r_{eff} is equal to the groove width w, i.e. $r_{\mathrm{eff}} = w$ [32]. This is applied to the crosshatch channels to calculate its r_{eff}. Due to the uncertainty of the width of the individual crosshatch channels, the width is assumed to be equal to the depth d and $2d$ (d=0.05 mm), then r_{eff} is of d and $2d$ respectively. The permeability k is assumed to be the permeability of a wick with a porosity of 0.7.

As shown in Table 4.4, $r_{\mathrm{eff}} = 2d$ gives a lower value of the capillary limit. The curve of capillary limit when $r_{\mathrm{eff}} = 2d$ is presented in Fig. 4.4.

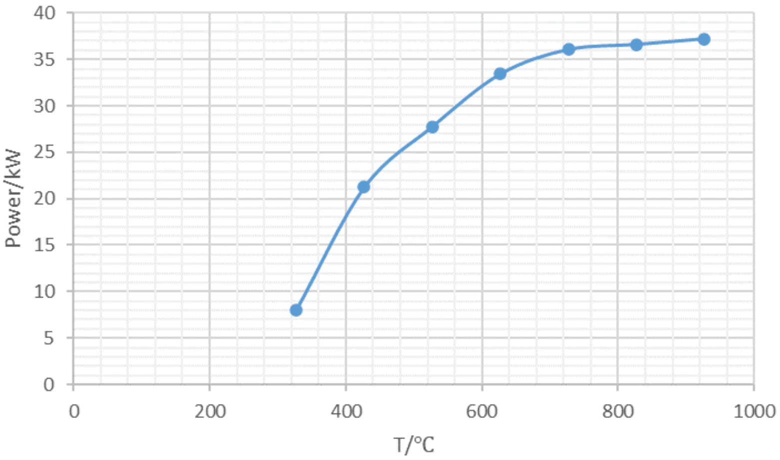

Figure 4.4: Capillary limit. r_{eff} is taken to be twice the crosshatch channel depth, i.e. $r_{\text{eff}} = 2d = 0.1$ mm.

4.6.5 Comparison with ACT

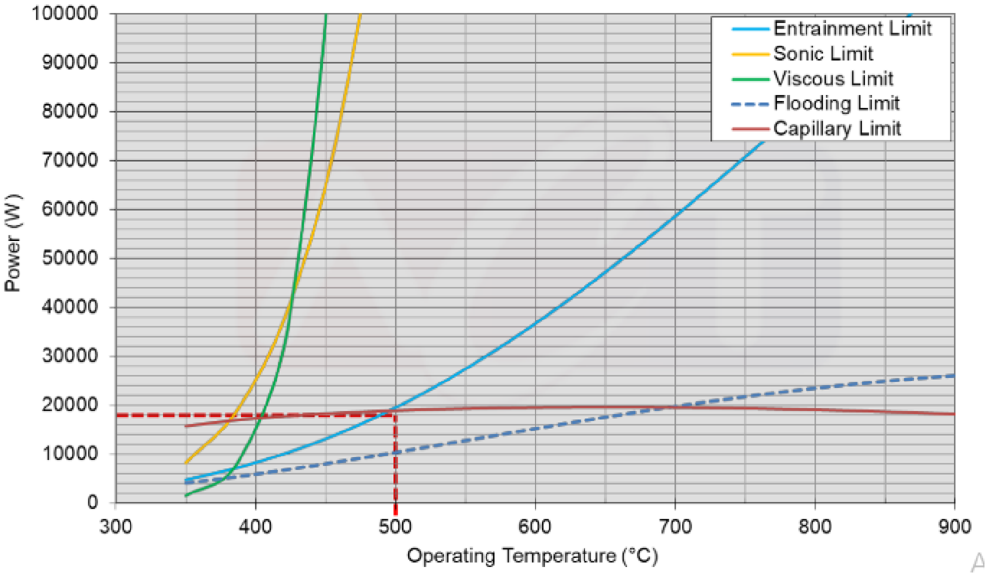

Figure 4.5: Operation limits of the heat pipe by ACT.

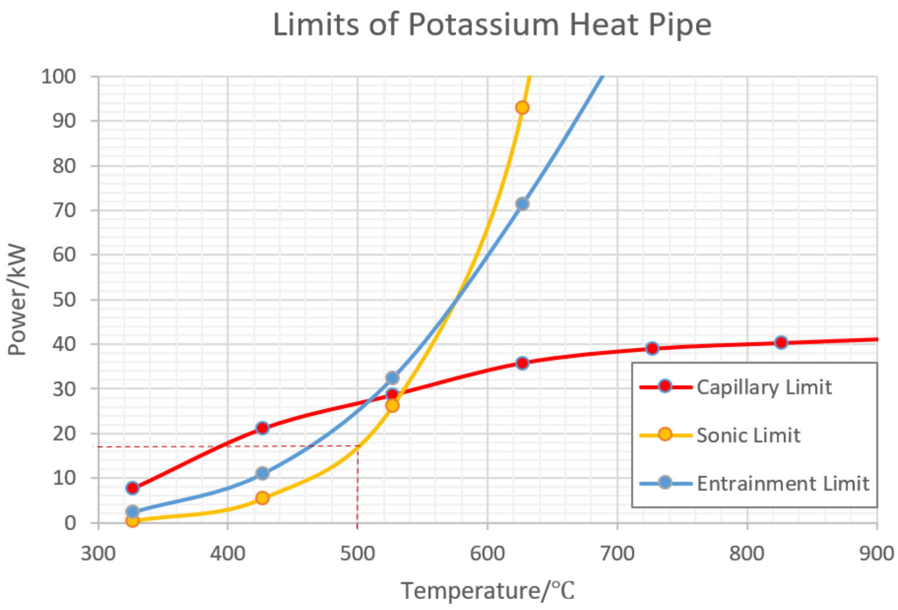

Figure 4.6: Calculated verification curves in this work.

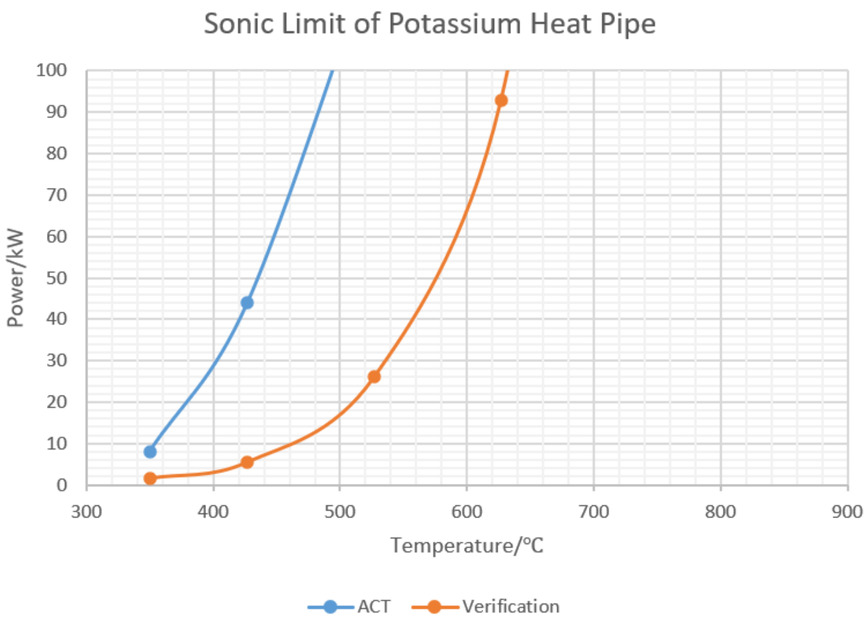

Figure 4.7: Compare the calculated verification sonic limit in this work with ACT's.

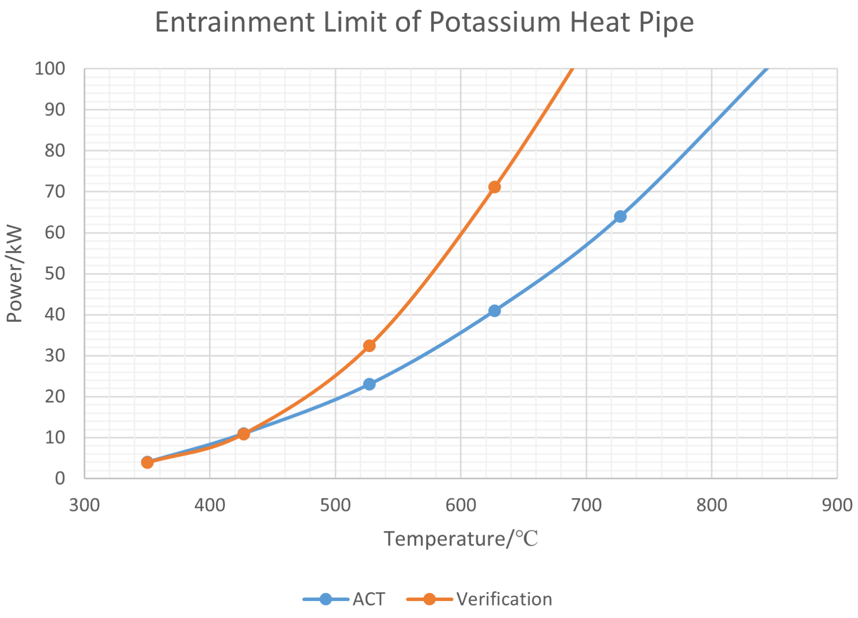

Figure 4.8: Compare the verification entrainment limit in this work with ACT's.

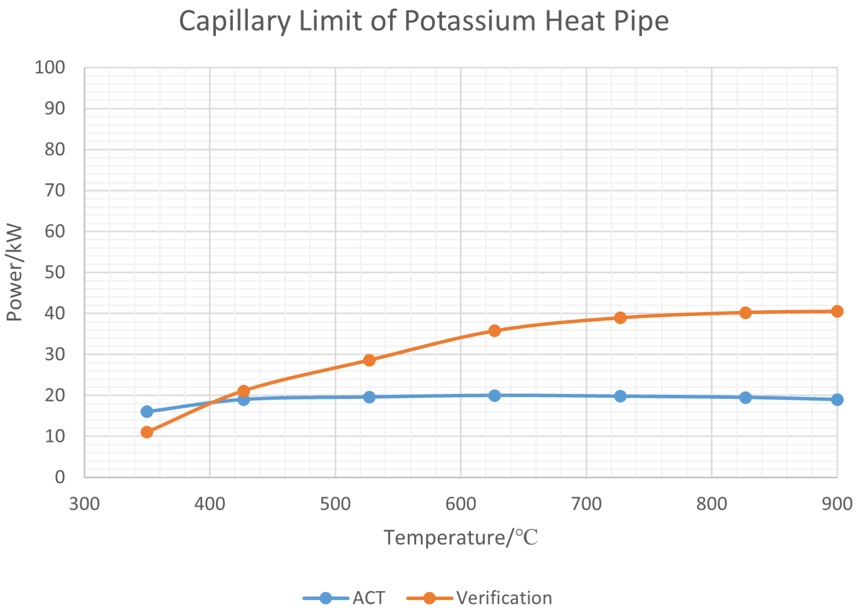

Figure 4.9: Compare the verification in this work capillary limit with ACT's.

Fig. 4.5 shows the limit curves by ACT and Fig. 4.6 presents the curves calculated from the equations and parameters that lead to the most conservative values (lowest values). For ACT's curves the maximum allowable power at 500 °C is 19 kW, while for the verification curves it is about 17 kW; to reach 19 kW the operation temperature needs to be brought up to 510 °C. The curves of each power limit in the two figures demonstrate a similar tendency of variation, which can be seen more clearly in the figures of individual limits, Fig. 4.7, 4.8, and 4.9.

However, the power limit showing the largest discrepancy between the calculated verification results and ACT's is the sonic limit. The sonic limit by ACT is always higher: the verification limit is about 17 kW at 500 °C, while for ACT it is above 100 kW. The differences in the entrainment limit and the capillary limit are relatively smaller, both limits being lower for ACT's curves at most temperatures; at lower temperatures ACT's curves are higher especially for the capillary limit. Note that the flooding limit mainly applies to heat pipes without a wick, and the viscous limit is primarily relevant for very low temperatures or high viscosity fluids [18], both irrelevant for the heat pipe design for CNB.

The resulted consequence of the various power limits is that, for the verification calculation as presented in Fig. 4.6, the maximum power of the heat pipe is determined by the sonic limit at lower temperatures and by the capillary limit at higher temperatures; while for ACT's evaluation shown in Fig. 4.5, it is the entrainment limit at lower temperatures and the capillary limit at higher temperatures that restrict the operating power. Nevertheless, the maximum power at 500 °C allowed in the verification curves does not differ a lot from that in ACT's curves; to attain a power of 19 kW the operating temperature only needs to increase by 10 °C for the verification calculation.

4.7 Compare Potassium with Sodium as Working Liquid

Another option of working fluid is sodium (Na). It has a lower absorption cross section for neutrons of 0.0528 barn in comparison of 2.098 barn for potassium (K). In this section, the power limits of sodium heat pipe are compared with those of the potassium heat pipe. The boiling limit of sodium is still too high to achieve and is therefore neglected.

Property	Potassium	Sodium
M/(g/mol)	39	23
P_0/Pa	6116	876
$\rho_\mathrm{v}/(\mathrm{kg/m^3})$	0.03524	0.00327
$\rho_\mathrm{l}/(\mathrm{kg/m^3})$	713.6	825.6
$\mu_\mathrm{v}/(\mathrm{Pa \cdot s})$	1.682e-5	1.827e-5
$\mu_\mathrm{l}/(\mathrm{Pa \cdot s})$	1.819e-4	2.298e-4
γ_g	1.644	1.625
L/(J/kg)	2.077e+6	4.237e+6
σ/(N/m)	0.0862	0.1521
C_son(theoretical)/(m/s)	528.9	685.5

Table 4.6: Properties of potassium and sodium at 527 °C.

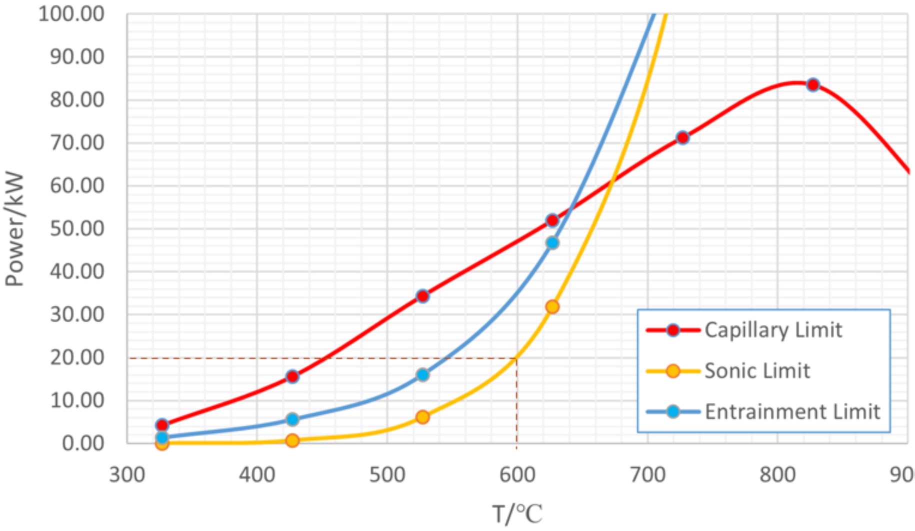

Figure 4.10: Calculated curves with the most conservative formulas. The inflection of capillary limit at 827 °C is due to the competing between increasing and decreasing variables with temperature.

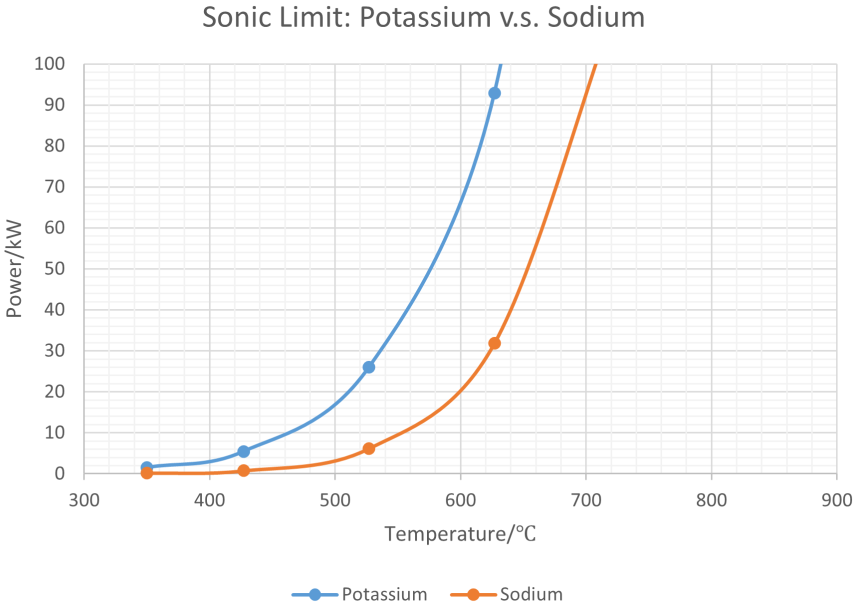

Figure 4.11: Sonic limit: potassium v.s. sodium.

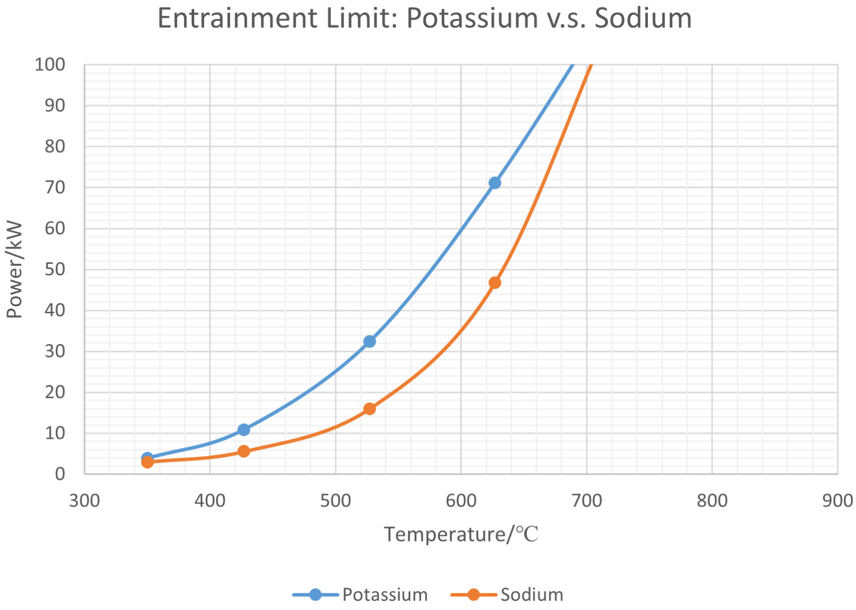

Figure 4.12: Entrainment limit: potassium v.s. sodium.

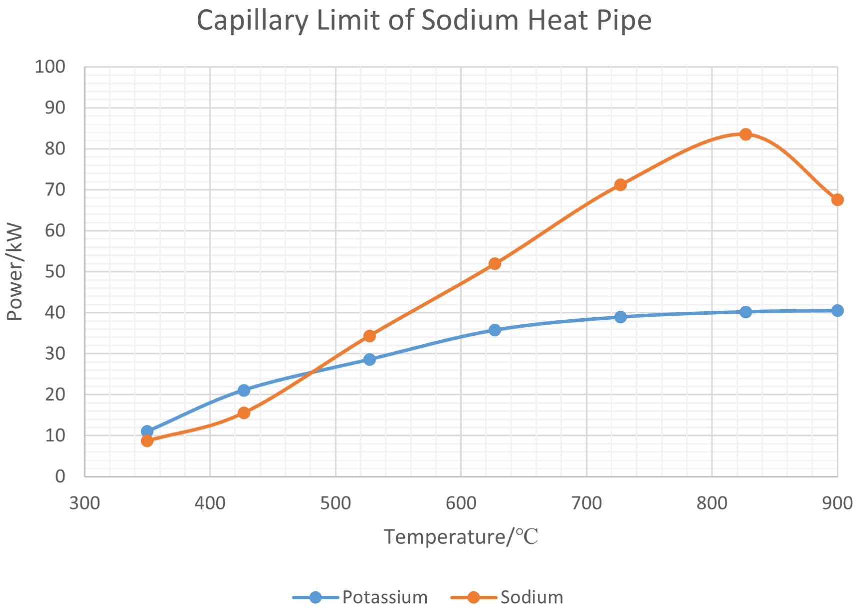

Figure 4.13: Capillary limit: potassium v.s. sodium.

Now examine the power limits individually. For sonic limit, citing again Busse's formula:

$$Q = 0.474 \times LA_{\mathrm{v}}\sqrt{\rho_0 P_0}. \tag{4.38}$$

Sodium has a much lower vapour density and saturation vapour pressure, and a much higher latent heat. As demonstrated in Fig. 4.11, the ultimate effect is that it has a lower sonic limit compared to potassium.

The formula for entrainment limit is:

$$Q = LA_{\mathrm{v}}\sqrt{\frac{\sigma\rho_{\mathrm{v}}}{2r_{\mathrm{h,s}}}}. \tag{4.39}$$

The latent heat and surface tension of sodium are much higher while the vapour density is much lower, resulting in a lower entrainment limit than potassium presented in Fig. 4.12.

For capillary limit, we need to first consider the various pressure drops separately.

In CNB's scenario, the capillary pressure and and gravity pressure drop act as pressure assists that help to bring liquid back to evaporator, while the viscous vapour pressure drop, inertial vapour pressure drop, and the liquid viscous pressure drop function as pressure losses which hinders the circulation of working fluid. In order to be consistent with the previously mentioned expressions of capillarity limit and gravity pressure drop, here we rewrite the capillary limit as:

$$\Delta P_{\mathrm{cap,max}} - \Delta P_{\mathrm{z}} \geq \Delta P_{\mathrm{vis}} + \Delta P_{\mathrm{i}} + \Delta P_{\mathrm{l}}, \tag{4.40}$$

which means if the pressure assists are greater than pressure losses, the heat pipe can operate. Note here $-\Delta P_{\mathrm{z}}$ is positive.

For capillary pressure:

$$\Delta P_{\mathrm{cap,max}} = \frac{2\sigma}{r_{\mathrm{eff}}}. \tag{4.41}$$

Since sodium has a much higher surface tension than potassium, its has a larger capillary pressure, i.e., $\Delta P_{\mathrm{cap,max}}(\mathrm{Na}) > \Delta P_{\mathrm{cap,max}}(\mathrm{K})$.

Integrated over the effective length, the gravity assist is:

$$\Delta P_{\mathrm{z}} = -\rho_{\mathrm{l}} g \sin\theta l_{\mathrm{eff}}. \tag{4.42}$$

Because of the higher liquid density, the gravity assist is greater for sodium, $\Delta P_{\mathrm{z}}(\mathrm{Na}) > \Delta P_{\mathrm{z}}(\mathrm{K})$.

If we solve for the viscous pressure drop of vapour Eq. 4.28 with Eq. 4.30 and Eq. 4.29 when $Re > 2000$, we find:

$$\Delta P_{\mathrm{vis}} = \frac{0.079\rho_{\mathrm{v}}^{0.75}\mu_{\mathrm{v}}^{0.25} l_{\mathrm{eff}}}{r_{\mathrm{v}} d_{\mathrm{v}}^{0.25}} \left(1 + \frac{\gamma - 1}{2(\frac{\gamma RT}{M})} U^2\right)^{-0.75} U^{1.75}. \tag{4.43}$$

Under the same velocity, sodium's viscous pressure drop is lower due to the overall effect of higher vapour viscosity and much lower vapour density, which can be verified by calculation. So $\Delta P_{\mathrm{vis}}(\mathrm{Na}) < \Delta P_{\mathrm{vis}}(\mathrm{K})$. Remember that this equation is attained with the assumption of effective length l_{eff}, which means the vapour velocity is assumed to remain at its maximum value U along l_{eff}, instead of a relatively realistic velocity profile as discussed in Sec. 4.5.

Similarly, for inertial pressure drop we have (typically $|Re_{\mathrm{r}}| < 1$):

$$\Delta P_{\mathrm{i}} = (\frac{\pi^2}{4} - 1)\rho_{\mathrm{v}} U^2. \tag{4.44}$$

Since sodium has a much lower vapour density, its inertial vapour pressure drop is consequently lower, i.e., $\Delta P_{\mathrm{i}}(\mathrm{Na}) < \Delta P_{\mathrm{i}}(\mathrm{K})$.

The viscous liquid pressure drop becomes:

$$\Delta P_{\mathrm{l}} = \frac{\mu_{\mathrm{l}} l_{\mathrm{eff}}}{\rho_{\mathrm{l}} A_{\mathrm{l}} k} \rho_{\mathrm{v}} A_{\mathrm{v}} U. \tag{4.45}$$

By virtue of the much lower vapour density and higher liquid density despite of the higher liquid viscosity, the liquid viscous pressure drop of sodium is lower at the same velocities $P_{\mathrm{l}}(\mathrm{Na}) < \mathrm{P}_{\mathrm{l}}(\mathrm{K})$.

In conclusion, the overall effect is that the sum of pressure assists of sodium is greater than those of potassium, while the sum of pressure losses is lower for sodium than for potassium at the same velocities and temperatures. As a result, sodium heat pipes are allowed to operate at higher velocities and powers given the same temperature; the capillary limit of sodium heat pipes is higher than that of potassium heat pipes.

Furthermore, it is obvious that sodium heat pipes can't operate at the nominal operation temperature of 500 °C. If we were to adopt sodium heat pipes, the operation temperature would need to be raised to 600 °C; or the radius of the pipes is increased to reduce the friction between vapour and liquid as well as the inertial pressure drop and to enlarge the cross-section of vapour space so that the power limits are raised.

Chapter 5

Thermodynamics Simulation of CNB

The thermodynamics of the hexagonal unit cell (or its 1/12 partition by virtue of the symmetry) and the 1/12 core geometry of CNB are simulated with STAR-CCM+. As shown in Figure 5.1, the core has a six-fold symmetry and each 1/6 partition has a reflective symmetry in itself. The black hexagon with 1 heat pipe and 6 half fuel rods (3 whole fuel rods) is chosen to be the unit cell model for the simulations. The detailed geometry is presented in Figure 5.2.

The thermophysical properties of various reactor materials are listed in Table 5.1 and 5.2. The properties of fuel stacks are calculated with a packing fraction of 0.55 (the volume of all TRISO fuel particles to the total volume of fuel rod), which means the properties of fuel stacks are volume weighted values of the properties of UO_2 and matrix graphite assuming the whole TRISO particle is filled with UO_2. Only the density ρ is calculated with the detailed compositions of TRISO (i.e., UO_2, SiC, buffer, and PyC) as shwon in Eq. 5.1, because the differences in densities of the compositions are large.

$$\rho_{\text{fuel stack}} = f_{\text{UO2}} \times \rho_{\text{UO2}} + f_{\text{buffer}} \times \rho_{\text{buffer}} + f_{\text{SiC}} \times \rho_{\text{SiC}} + f_{\text{PyC}} \times \rho_{\text{PyC}}, \tag{5.1}$$

where f is volume fraction.

Note that in all simulations the heat pipes are regarded as superconductors, inputted as 1×10^7 W/m-K to STAR-CCM+. There is no thermal-hydraulics in those simulations. The purpose of the thermodynamics simulations is to examine the temperature and the heat pipe power distributions throughout the core at BOL (Beginning of Life), MOL (Middle of Life), and EOL (End of Life), and to evaluate the temperature changes during power expedition transients. The heat pipe failure accidents are preliminarily examined at BOL as examples to understand the extent and propagation of heat pipe failures. Those works provide first information about the thermodynamics of the reactor core during early development stage of the project.

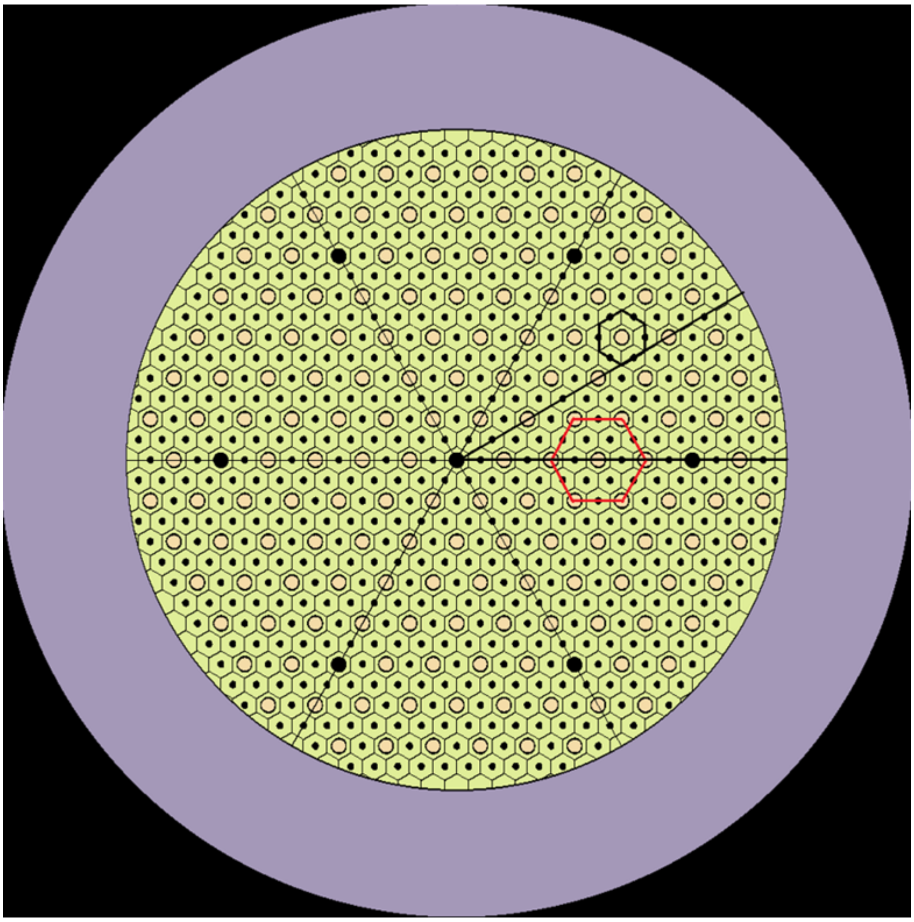

Figure 5.1: The core layout of CNB. The core has a six-fold symmetry and each 1/6 partition has a reflective symmetry in itself. The small black dots are fuel rods, the large yellow dots are heat pipes, and the large black dots indicate control rods. The black hexagon is chosen as the unit cell model.

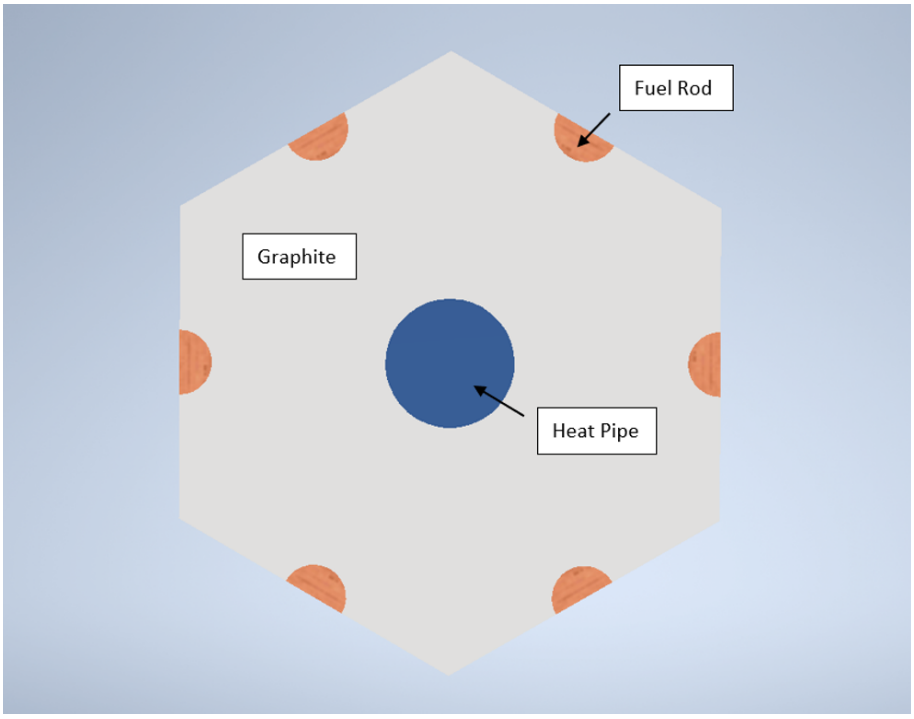

Figure 5.2: Geometry of the hexagonal unit cell with one heat pipe and six half fuel rods (three whole fuel rods).

Initially, the CNB core had helium gaps between heat pipes and the moderator; later this feature was removed and instead a helium cover gas of 4 cm thickness is added to the exterior surfaces of the top, bottom, and side reflectors. In this material, only the simulations of the core geometry with helium gaps on reflectors are presented.

Material	Property	Input	Note
UO_2	ρ	$11,000$	[41]
	k	$k = \frac{100}{7.5408 + 17.692t + 3.6142t^2} + \frac{6400}{t^{5/2}} exp\left(\frac{-16.35}{t}\right)$	[42], t=(T[C]+273)/ 1000
	c_p	$c_p = 52.1743 + 87.951t - 82.2411t^2 + 31.542t^3 - 2.6334t^4 - 0.71391t^{-2}$	[42], t=(T[C]+273)/ 1000
Matrix Graphite	ρ	1,892	TBD
	k	20	TBD
	c_p	$c_p = \frac{1.75 \times 10^6}{\rho}(0.645 + 3.14t - 2.809t^2 + 0.959t^3)$	[5], t=T[C]/1000
Fuel Stack	ρ	2444	volume weighted
	k	Table 7.14	UO_2& graphite
	c_p	$c_p = 5\text{e-}7T^3 - 0.0014T^2 + 1.5831T + 421.07$	T[C], Table 7.16, UO_2& graphite
Moderator Graphite	ρ	1873.9	[43]
	k	Table 7.13	[43]
	c_p	$c_p = 9\text{e-}7T^3 - 0.0025T^2 + 2.9252T + 662.46$	[43], T[C], Table 7.13
Helium	ρ	0.08398	[44]
	k	Table 7.11	[45]
	c_p	5193	[44]

Table 5.1: Table of properties of materials. ρ [kg/m^3], k [W/m-K], c_p [J/kg-K]. TBD: to be determined. Note that all thermal conductivities are input as tables, specfic heat c_p's are input as functions either directly from literature or fitted from tables, and ρ's are input as constants.

Material	Property	Input	Note
SiC	ρ	3180	[41]
	k	13.9	[41]
	$\mathrm{c_p}$	$c_\mathrm{p} = 925.65 + 0.3772t - 7.9259\text{e-}5t^2 - 3.1946\text{e+}7/t^2$	[8], t=T[C]+273
PyC	ρ	1900	[41]
	k	4	[41]
	$\mathrm{c_p}$	720	[41]
Buffer	ρ	1000	[41]
	k	0.5	[41]
	$\mathrm{c_p}$	720	[41]

Table 5.2: Table of properties of materials continued. ρ [kg/m^3], k [W/m-K], c_p [J/kg-K].

5.1 Cylindrical Model Verification

A simplified model of cylindrical geometry abstracted from the original hexagonal unit cell is investigated through both calculation and simulation at steady state in order to verify the precision of the simulating function of STAR-CCM+. The model keeps only the key features of the hexagonal geometry, consisting of a cylindrical vapour core, a graphite moderator, and a fuel layer as shown in Table 5.3. The thermal conductivities of the materials are presented in Table 5.4. The conditions are:

- the outmost fuel layer has a volumetric heat generation rate of 1.3×10^7 W/m^3. The volume of fuel and total heat generation are the same with that in the actual hex unit cell
- the vapour core is set at a constant temperature of T_v= 500 °C. For STAR-CCM+, the interface of vapour/graphite is set at 500 °C because the whole vapour core cannot be fixed at a constant temperature
- all exterior surfaces of the cylindrical assembly are adiabatic

Parameter	Value/m
Height	1.5
Radius of vapour core r_v	0.0207
Outer radius of graphite moderator r_g	0.099
Outer radius of fuel layer r_f	0.1

Table 5.3: Parameters of the simple model without helium gap

Material	Thermal conductivity/(W/m-K)
Vapour	1×10^7
Graphite	90
Fuel	15

Table 5.4: Thermal conductivities

The general heat diffusion equation in cylindrical coordinates is written as:

$$\frac{1}{r}\frac{\partial}{\partial r}\left(kr\frac{\partial T}{\partial r}\right)+\frac{1}{r^2}\frac{\partial}{\partial \phi}\left(kr\frac{\partial T}{\partial \phi}\right)+\frac{\partial}{\partial z}\left(k\frac{\partial T}{\partial z}\right)+q_\mathrm{v}=\rho c_\mathrm{p}\frac{\partial T}{\partial t}. \tag{5.2}$$

In the case of the cylindrical model, there is only one degree of freedom r and the problem is steady-state. The equation reduces to:

$$\frac{1}{r}\frac{d}{dr}\left(kr\frac{dT}{dr}\right)+q_\mathrm{v}=0. \tag{5.3}$$

The general solution is:

$$T_\mathrm{f}(r)=-\frac{q_\mathrm{v}r^2}{4k_\mathrm{f}}+C_1\mathrm{ln}r+C_2, \tag{5.4}$$

where T_f is the temperature distribution in fuel, k_f is the thermal conductivity of fuel.

In the graphite there is no heat source, and the equation becomes:

$$\frac{1}{r}\frac{d}{dr}\left(kr\frac{dT}{dr}\right)=0. \tag{5.5}$$

The solution is:

$$T_\mathrm{g}(r)=C_3\mathrm{ln}r+C_4, \tag{5.6}$$

where T_g is the temperature distribution in graphite.

The boundary conditions are:

$$r = r_{\mathrm{f}}, \qquad \frac{dT_{\mathrm{f}}}{dr} = 0. \tag{5.7}$$

$$r = r_{\mathrm{g}}, \qquad T_{\mathrm{g}}(r_{\mathrm{g}}) = T_{\mathrm{f}}(r_{\mathrm{g}}), \tag{5.8}$$

$$r = r_{\mathrm{g}}, \qquad -k_{\mathrm{g}}\frac{dT_{\mathrm{g}}}{dr} = -k_{\mathrm{f}}\frac{dT_{\mathrm{f}}}{dr}, \tag{5.9}$$

$$r = r_{\mathrm{v}}, \quad T_{\mathrm{g}}(r_{\mathrm{v}}) = T_{\mathrm{v}}, \tag{5.10}$$

Solving these equations, we get the expressions of the coefficients:

$$C_1 = \frac{q_{\mathrm{v}} r_{\mathrm{f}}^2}{2k_{\mathrm{f}}}, \tag{5.11}$$

$$C_2 = T_1 + \ln\left(\frac{r_{\mathrm{g}}}{r_{\mathrm{v}}}\right)\frac{q_{\mathrm{v}}(r_{\mathrm{f}}^2 - r_{\mathrm{g}}^2)}{2k_{\mathrm{g}}} + \frac{q_{\mathrm{v}}(r_{\mathrm{g}}^2 - 2r_{\mathrm{f}}^2 \ln r_{\mathrm{g}})}{4k_{\mathrm{f}}}, \tag{5.12}$$

$$C_3 = \frac{q_{\mathrm{v}}(r_{\mathrm{f}}^2 - r_{\mathrm{g}}^2)}{2k_{\mathrm{g}}}, \tag{5.13}$$

$$C_4 = T_1 - \ln r_{\mathrm{v}} \frac{q_{\mathrm{v}}(r_{\mathrm{f}}^2 - r_{\mathrm{g}}^2)}{2k_{\mathrm{g}}}. \tag{5.14}$$

Values of the coefficients are to be as shown in Table 5.5.

C_1/K	4333.33
C_2/K	12779.90
C_3/K	86.23
C_4/K	834.38

Table 5.5: Values of coefficients.

The radial temperature profiles by calculation and simulation are presented in Figure 5.3. The result from STAR-CCM+ agrees well with calculation. Thus we can conclude for the simple cylindrical model the simulating capacity of STAR-CCM+ is reliable.

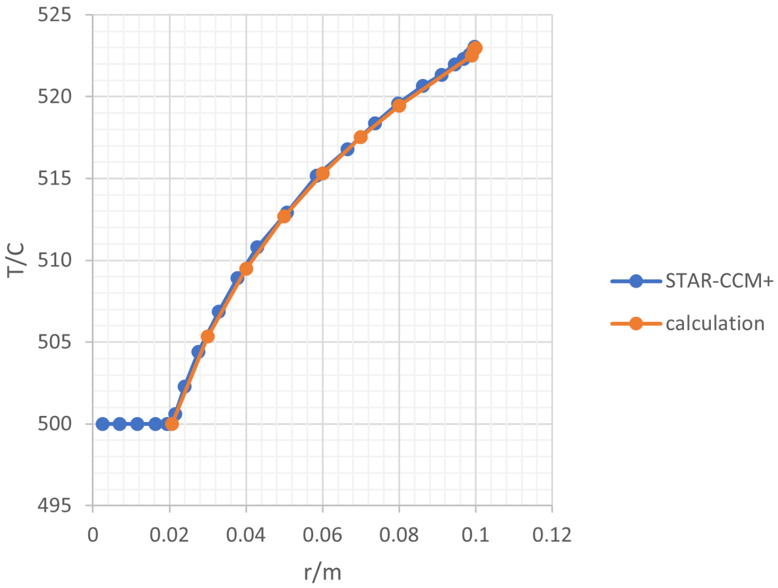

Figure 5.3: Radial temperature profiles by calculation and STAR-CCM+.

Now examine a cylindrical model with n layers (n $\geq$ 3): from the outmost layer to the centre cylinder the numbering of the layers is 1, 2, ..., n. The outmost layer has a constant volumetric heat q_v, thermal conductivity k_1, and outer radius r_1; layer i (1 < i < n) has a outer radius r_i and thermal conductivity k_i without heat source in it; and the centre cylinder is of a constant temperature T_n and radius r_n. The formulas of temperatures are:

$$T_1(r) = -\frac{q_\mathrm{v} r^2}{4k_\mathrm{f}} + C_1 \ln r + C_2, \tag{5.15}$$

$$T_2(r) = C_3 \ln r + C_4, \tag{5.16}$$

......

$$T_{\mathrm{n}-1}(r) = C_{2(\mathrm{n}-1)-1} \ln r + C_{2(\mathrm{n}-1)}. \tag{5.17}$$

The boundary conditions are:

$$r = r_1, \qquad \frac{dT_1}{dr} = 0, \tag{5.18}$$

$$r = r_2, \qquad T_2(r_2) = T_1(r_2), \tag{5.19}$$

$$r = r_2, \qquad -k_2\frac{dT_2}{dr} = -k_1\frac{dT_1}{dr}, \tag{5.20}$$

......

$$r = r_{\mathrm{n}-1}, \qquad T_{\mathrm{n}-1}(r_{\mathrm{n}-1}) = T_{\mathrm{n}-2}(r_{\mathrm{n}-1}), \tag{5.21}$$

$$r = r_{\mathrm{n}-1}, \qquad -k_{\mathrm{n}-1}\frac{dT_{\mathrm{n}-1}}{dr} = -k_{\mathrm{n}-2}\frac{dT_{\mathrm{n}-2}}{dr}, \tag{5.22}$$

$$r = r_{\mathrm{n}}, \qquad T_{\mathrm{n}-1}(r_{\mathrm{n}}) = T_{\mathrm{n}}. \tag{5.23}$$

There are in total 2(n − 1) coefficients, C_1, C_2, ..., and $C_{2(\mathrm{n}-1)}$. Each formula of temperature has two coefficients in it. The general solutions to the coefficients are:

$$C_1 = \frac{q_{\mathrm{v}} r_1^2}{2k_1}, \tag{5.24}$$

$$C_2 = T_{\mathrm{n}} + \ln\left(\frac{r_{\mathrm{n}-1}}{r_{\mathrm{n}}}\right)\frac{q_{\mathrm{v}}(r_1^2 - r_2^2)}{2k_{\mathrm{n}-1}} + ... + \ln\left(\frac{r_2}{r_3}\right)\frac{q_{\mathrm{v}}(r_1^2 - r_2^2)}{2k_2} + \frac{q_{\mathrm{v}}(r_2^2 - 2r_1^2\ln r_2)}{4k_1}, \tag{5.25}$$

for m is odd and 1 < m < 2(n − 1):

$$C_{\mathrm{m}} = \frac{q_{\mathrm{v}}(r_1^2 - r_2^2)}{2k_{\frac{\mathrm{m}+1}{2}}}, \tag{5.26}$$

for m is even and 2 < m < 2(n − 1):

$$C_{\mathrm{m}} = T_{\mathrm{n}} + \ln\left(\frac{r_{\mathrm{n}-1}}{r_{\mathrm{n}}}\right)\frac{q_{\mathrm{v}}(r_1^2 - r_2^2)}{2k_{\mathrm{n}-1}} + ... + \ln\left(\frac{r_{\frac{\mathrm{m}}{2}+1}}{r_{\frac{\mathrm{m}}{2}+2}}\right)\frac{q_{\mathrm{v}}(r_1^2 - r_2^2)}{2k_{\frac{\mathrm{m}}{2}+1}} - \ln r_{\frac{\mathrm{m}}{2}+1}\frac{q_{\mathrm{v}}(r_1^2 - r_2^2)}{2k_{\frac{\mathrm{m}}{2}}}, \tag{5.27}$$

and

$$C_{2(\mathrm{n}-1)} = T_{\mathrm{n}} - \ln r_{\mathrm{n}}\frac{q_{\mathrm{v}}(r_1^2 - r_2^2)}{2k_{\mathrm{n}-1}}. \tag{5.28}$$

5.2 One-Twelfth Hexagonal Unit Cell Model

The steady state and a hypothetical transient of double nominal power are simulated for the 1/12 hexagonal unit cell model (with 1/12 heat pipe and a quarter fuel rod) to examine the thermodynamic behaviours of the core, especially the temperature distributions in comparison to the melting temperature of fuel. The selection of one-twelfth of the unit cell is to save computation time. The conditions and results are discussed in this section.

5.2.1 Nominal Steady State of 1/12 Unit Cell

The one-twelfth unit cell is simulated for steady-state nominal operation. The heat pipe is modeled as a super conductor column without wall and wick structure as those details hardly influence the overall heat distribution. The heat pipe is in direct contact with graphite. A 4 cm helium gap is added to each exterior surface of the reflectors. The simulation conditions are as follows:

- 495 °C condenser surface of the heat pipe
- 100 °C helium gap exterior surfaces
- a power distribution along the 10 fuel segments as shown in Table 5.6. The average power density is 8.48×10^6 W/m^3, and the total power is 17.3 kW

Fuel segment/cm	$q_v/(W/m^3)$
75, 60	6.31e6
60, 45	6.73e6
45, 30	7.85e6
30, 15	8.95e6
15, 0	10.25e6
0, -15	10.32e6
-15, -30	9.02e6
-30, -45	8.95e6
-45, -60	8.64e6
-60, -75	7.75e6

Table 5.6: Axial power density distribution. The average power density is 8.48×10^6 W/m^3. The total power is 17.3 kW.

The maximum and volume average temperatures of various components are presented in Table 5.7. The maximum temperature is 569 °C, well below the melting temperature of fuel (∼1600 °C).

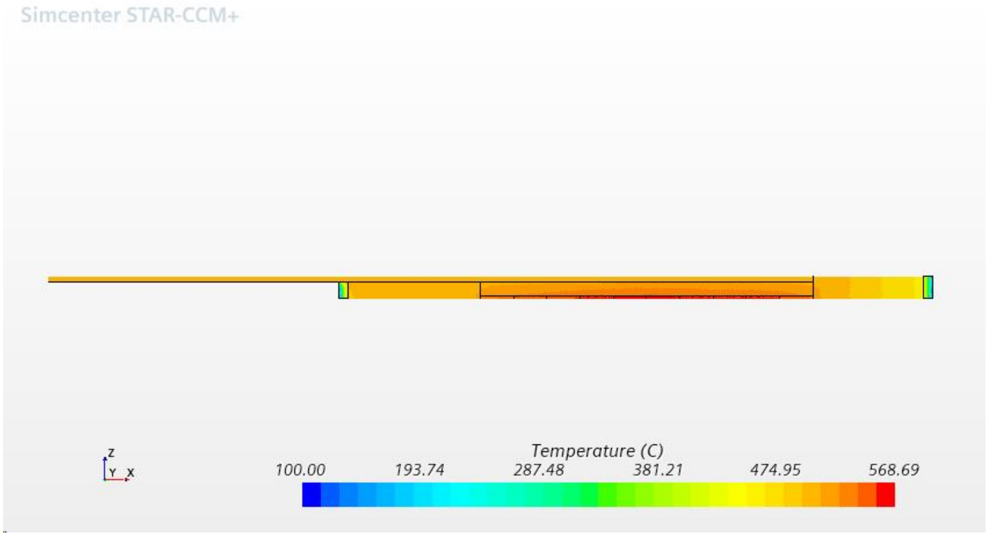

Figure 5.4: Steady-state simulation of 1/12 hexagonal unit cell.

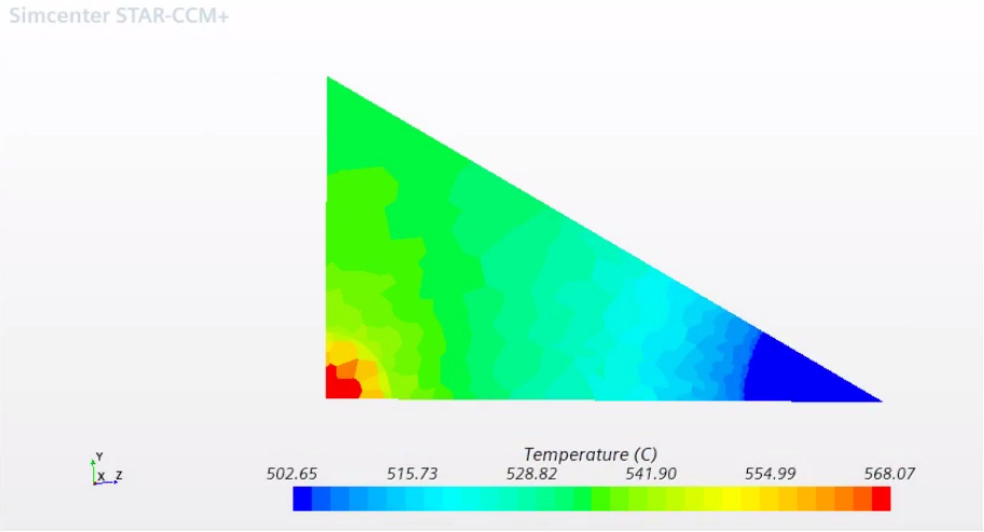

Figure 5.5: Cross-section of the steady-state simulation of 1/12 hexagonal unit cell.

Temperature	Value/°C
T_{max}	569
T_{ave} (fuel)	546
T_{ave} (moderator)	525
T_{ave} (bottom reflector)	487
T_{ave} (top reflector)	502
T_{ave} (bottom helium)	311
T_{ave} (top helium)	342

Table 5.7: Maximum and volume average temperatures of core components at nominal steady state.

5.2.2 Double Power Transient of 1/12 Unit Cell

A hypothetical transient of double nominal power is simulated. Actually, such transient is not valid because the heat pipe would fail if the power raises to 200 %. But it still provides information about the thermal response of the core components assuming heat transfer is perfect. The conditions are:

- double values of power densities at nominal steady state shown in Table 5.6
- volume average temperatures at nominal state in Table 5.7 are used as initial temperatures
- other conditions remain the same with nominal state

The time plot of the maximum and volume average temperatures of various geometry components are presented in Figure 5.8. The maximum temperature is 643 °C compared to the 569 °C at steady state, still well below the melting temperature of fuel.

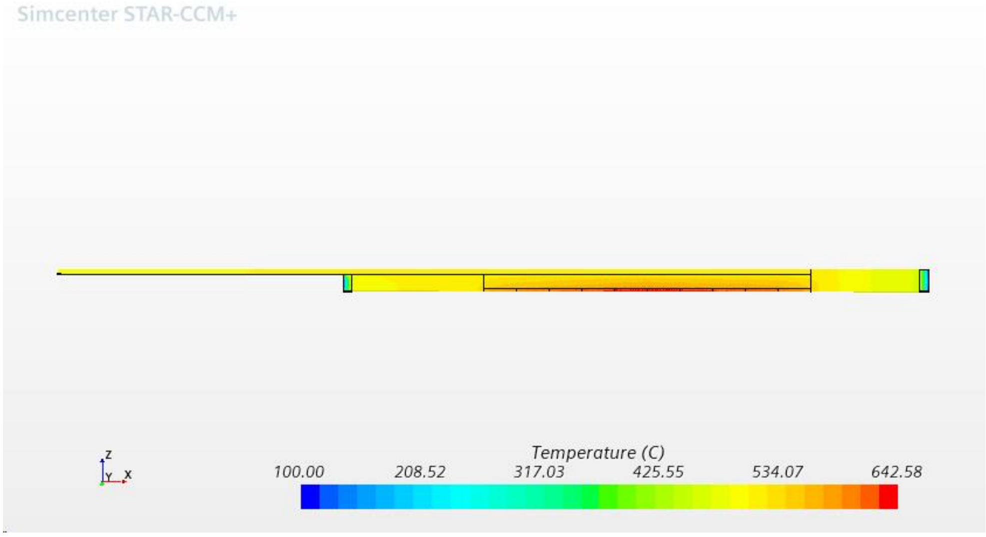

Figure 5.6: Transient simulation of 1/12 hexagonal unit cell at the end of time.

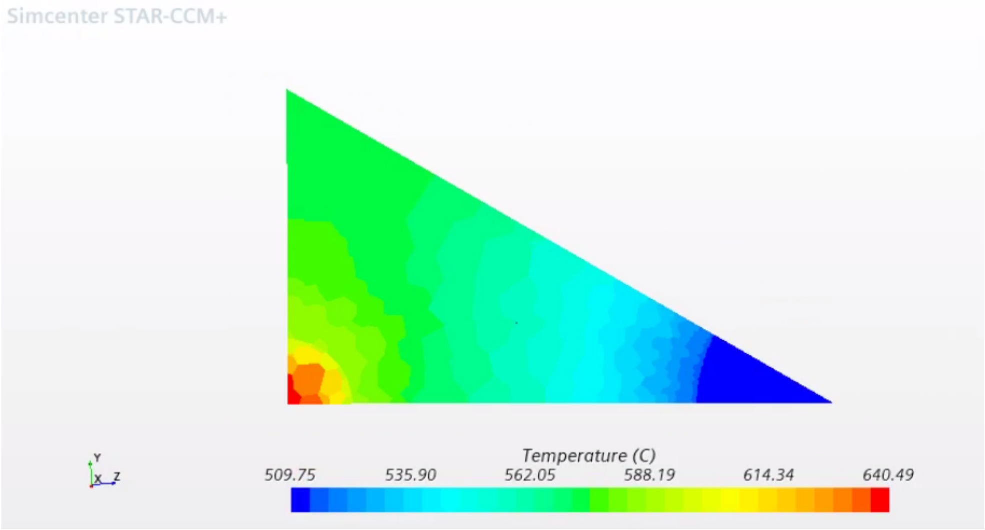

Figure 5.7: Cross-section of the transient simulation of 1/12 hexagonal unit cell at the end of time.

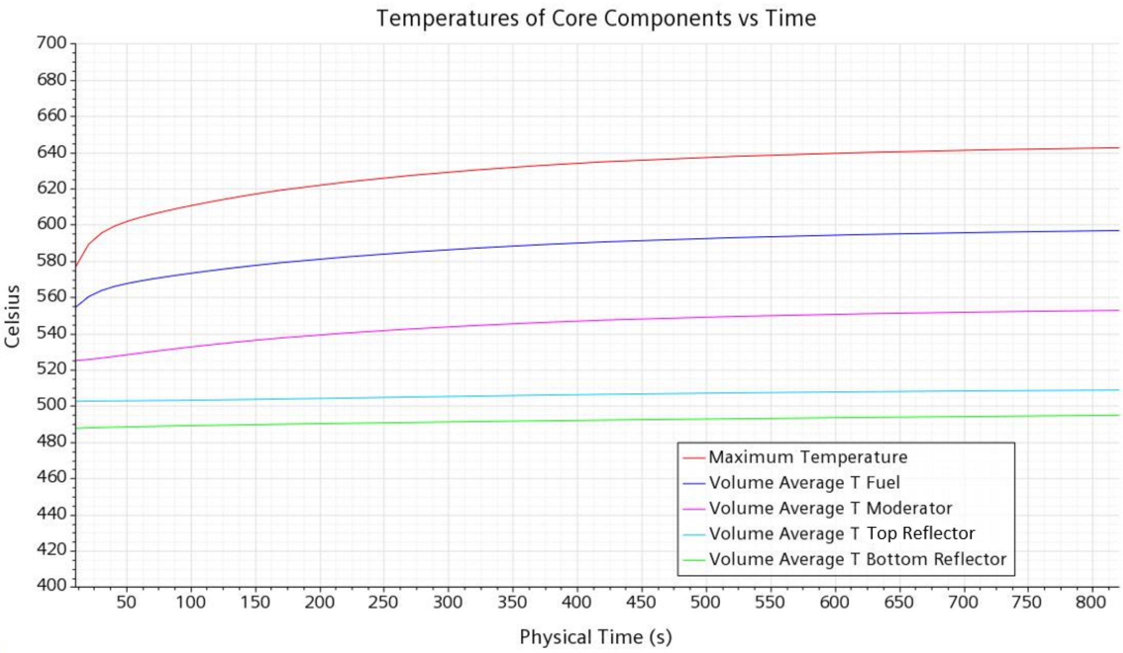

Figure 5.8: Time plot of the maximum temperature in fuel and volume average temperatures of core components.

5.3 TRISO Particle

A single TRISO particle is simulated at the nominal state and the hypothetical double power transient. Both simulations show that the temperature difference throughout a TRISO particle is small, usually less than 3 °C. The geometry parameters are listed in Table 5.8.

Radius	Value/μm
Radius of kernel r_1	212.5
Outer radius of buffer r_2	312.5
Outer radius of IPyC r_3	352.5
Outer radius of SiC r_4	387.5
Oter radius of OPyC r_5	427.5

Table 5.8: Radiuses of TRISO particle geometry [46]

5.3.1 TRISO Particle at Nominal Steady State

The single TRISO particle model at nominal state is investigated. The conditions are:

- the initial temperatures of materials and the external surface of OPyC layer are set to be the maximum temperature in the 1/12 unit cell nominal state, 569 °C
- the volumetric heat of the fuel kernel is 9.9×10^7 W/m^3

The results show that the maximum temperature is 570 °C, and the temperature difference in the particle is less than 1 °C, which means for the neutronics calculations performed in Serpent, the temperature input of TRISO particle can be the same with the temperature input of fuel.

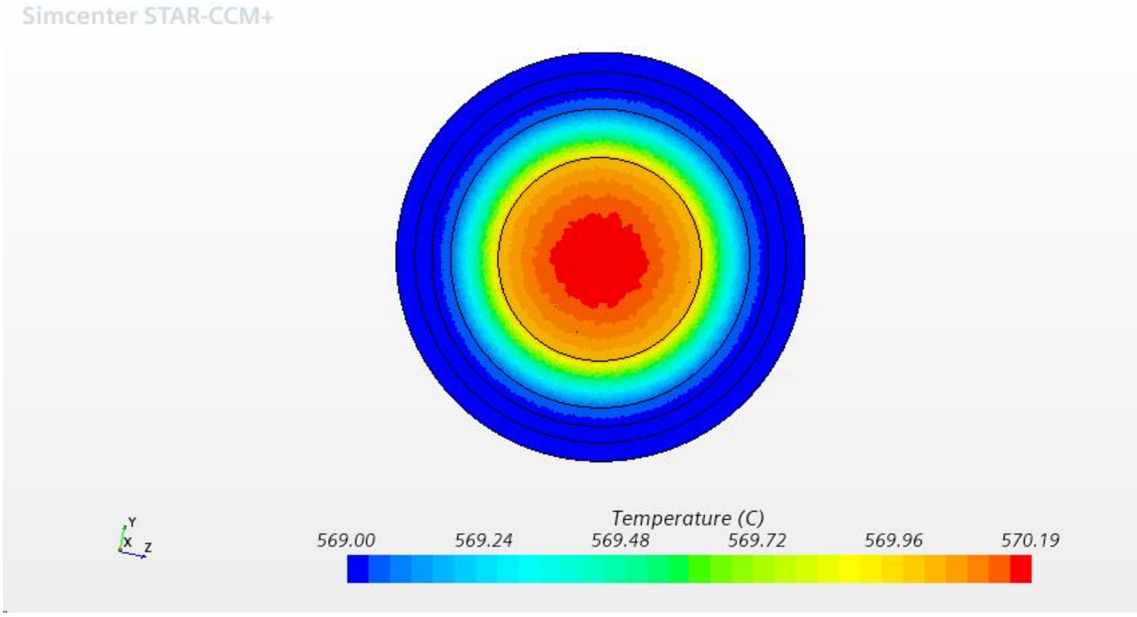

Figure 5.9: TRISO particle at nominal steady state.

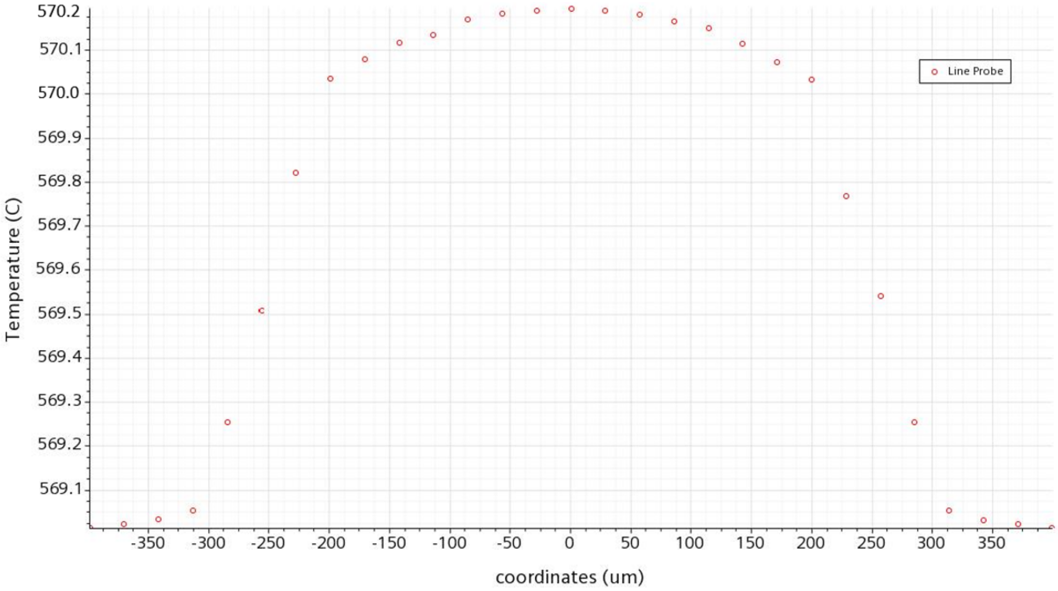

Figure 5.10: TRISO steady-state temperature plot along the diameter.

5.3.2 TRISO Particle at Double Power Transient

The temperature distribution of a TRISO particle at the hypothetical double power transient is simulated. The conditions are:

- double kernel volumetric heat of 19.8×10^7 W/m^3
- the static temperature distribution of TRISO particle is used as the initial temperature distribution
- the temperature of the external surface of OPyC uses the maximum temperature in fuel as a function of time in the 1/12 hex cell transient, $\mathrm{T}_{\mathrm{max}}(\mathrm{t})$

In this case, the maximum temperature $T_{\max}$ is 645 °C in comparison to the 643 °C in fuel in the 1/12 hex cell transient. There is only a small difference of $\sim$ 2 degree as expected, since the TRISO particle is very small and the temperature variation across it shouldn't be large.

The difference between the steady-state temperature distribution and that at the stable period of the transient, as well as the timescale of the particle transient are mainly determined by the fuel temperature input $T(t)$ from the 1/12 hex cell transient; the microscopic processes such as the heat transfer within the particle imposes a smaller influence. Note that here the timescale of heat transfer within the particle is not investigated.

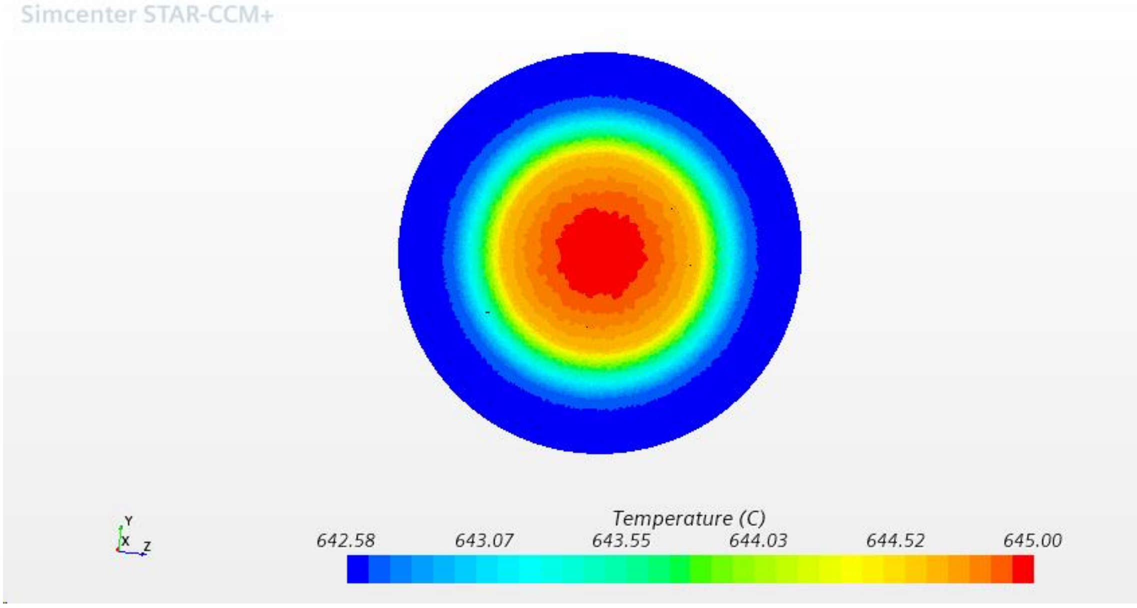

Figure 5.11: TRISO particle at the end of simulation time.

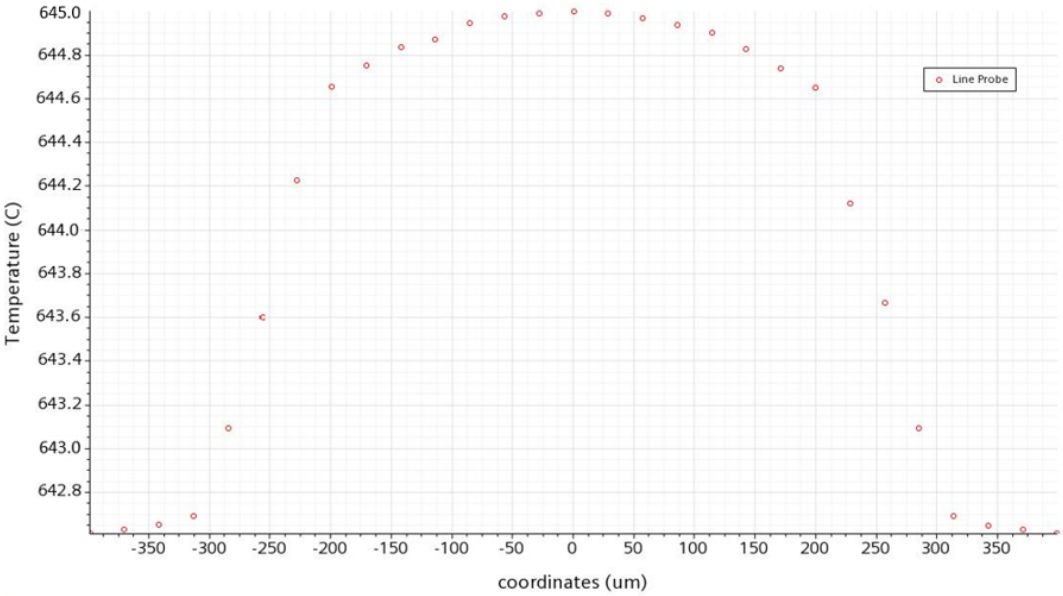

Figure 5.12: TRISO transient temperature profile along the diameter at the end of simulation time.

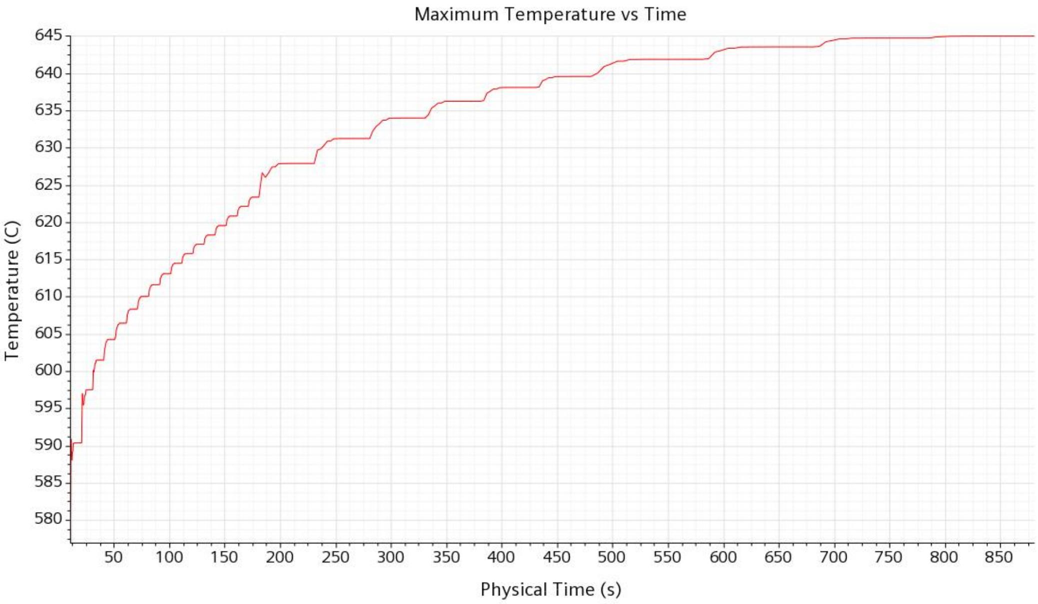

Figure 5.13: Time plot of the maximum temperature of the TRISO particle. The discontinuity of the curve is due to the time-step simulation approach of STAR-CCM+.

5.4 One-Twelfth Core Model

In this section, the one-twelfth of the whole core is simulated at steady state to observe the temperature distribution throughout the core. A five-digit numbering scheme is applied to the reactor core to differentiate the positions of rods as presented in Figure 5.14. The first digit indicates one of the six partitions of the hexagonal core geometry; the next two digits refer to the number of the row; the last two digits refer to the column, i.e. SRRCC. Exceptionally, the number of the centre control rod is 101.

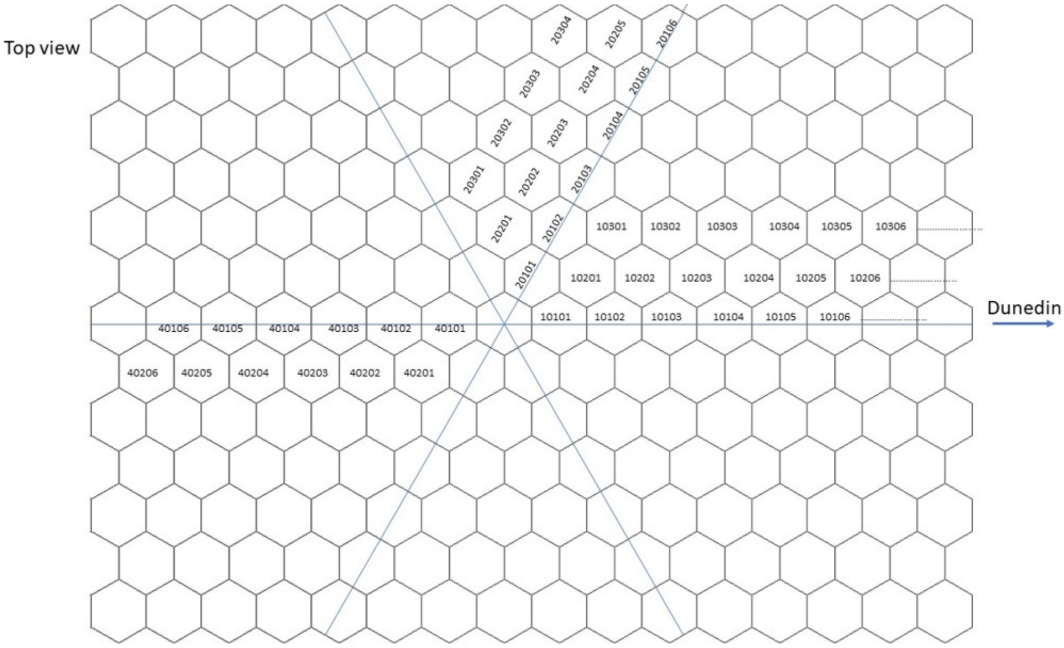

Figure 5.14: Numbering scheme.

5.4.1 Nominal Steady State of 1/12 Core

Two meshes are tested for the simulation. Mesh 1 is coarser while mesh 2 is finer. The base sizes of various geometry components are the same, but the actual sizes of mesh cells are also influenced by the prism layers, which are layers of mesh grown on the interfaces between components to buffer the meshing from the edge to the centre of the component where bulk meshing is applied. The settings of prism layers can be found in Appendix D.

It is found that the temperature distributions at BOL nominal state are nearly the same. The centreline temperature profiles of fuel rod 10406 in the two meshes are shown in Figure 5.21, which agree well with each other. Finally, mesh 2 is used as the mesh for following simulations.

The simulating conditions are:

- 500 °C condenser wall temperature
- 100 °C helium gap exterior surfaces
- a detailed power density distribution in the core, which varies both axially along the fuel rods and radially across fuel rods, is implemented as the heat source

Geometry component	Base mesh size/m
Reflectors	0.03
Helium gaps and fuel rods	0.005
Heat pipes	0.01

Table 5.9: Base mesh sizes for mesh 1 and mesh 2. The mesh size is also influenced by the prism layers that form at the interfaces of geometry components.

Mesh 1:

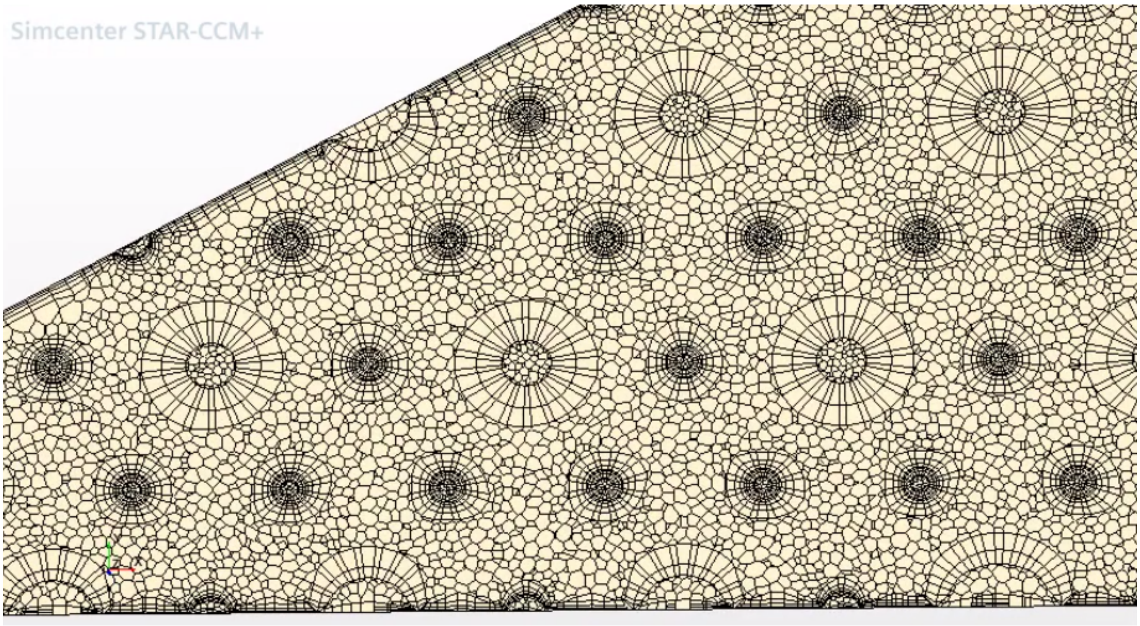

Figure 5.15: Mesh 1.

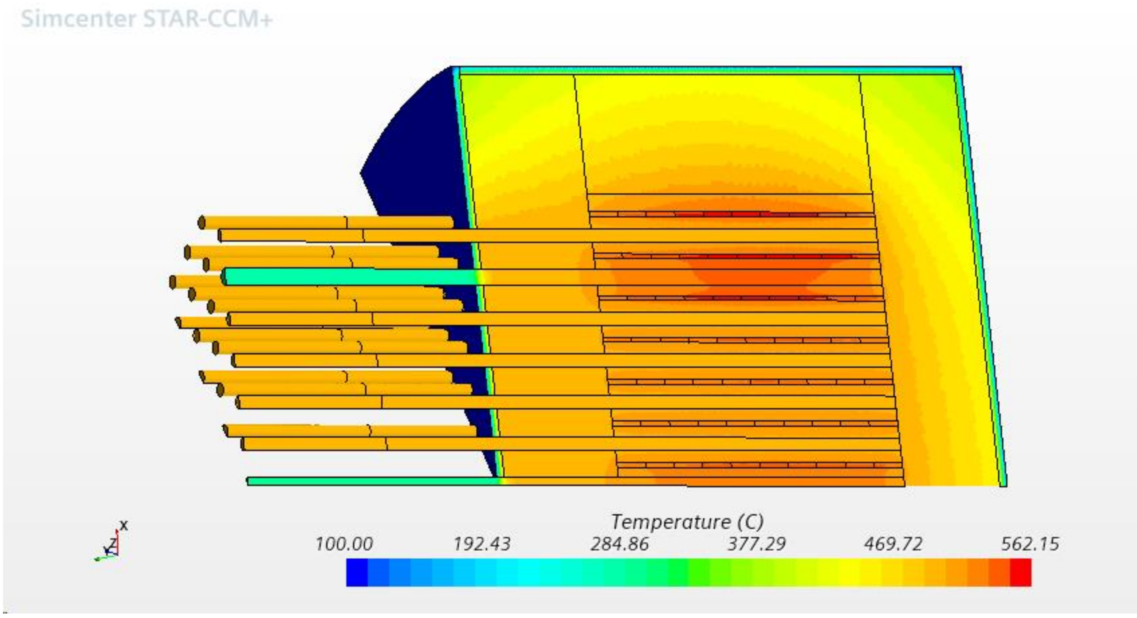

Figure 5.16: Temperature distribution at nominal state BOL in Mesh 1.

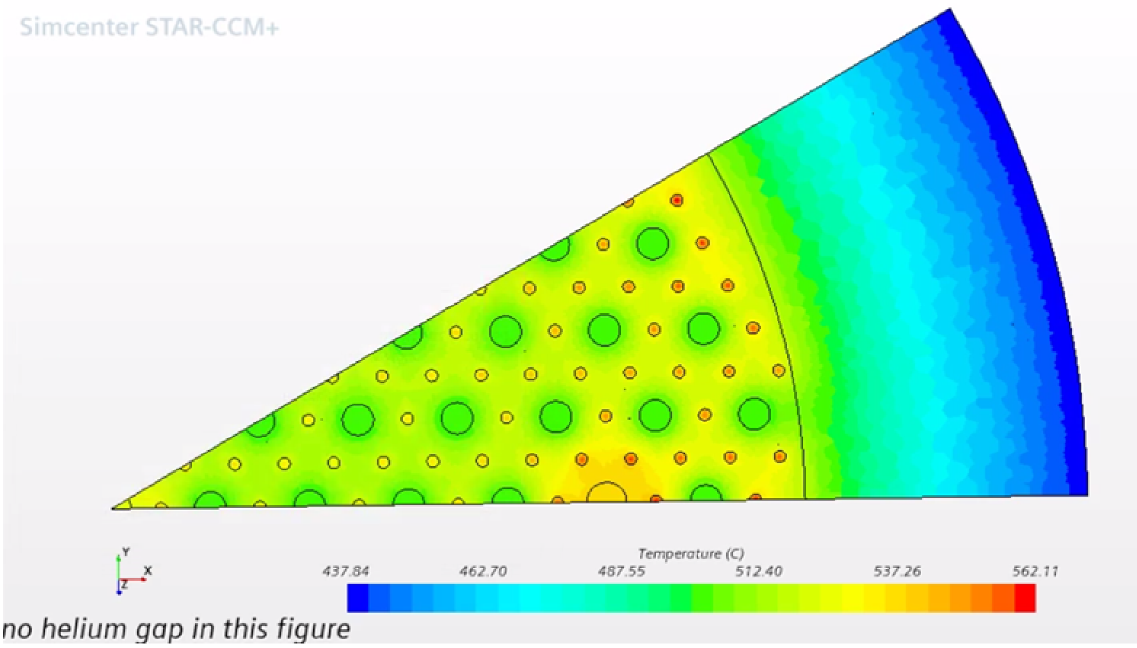

no helium gap in this figure

Figure 5.17: Cross-section at the middle of the core at BOL in Mesh 1. Note the large orange rod in the lowest row (10110) and the rod at the centre (101) are control rods. They don't take away heat so the temperature is higher at those two positions.

Mesh 2:

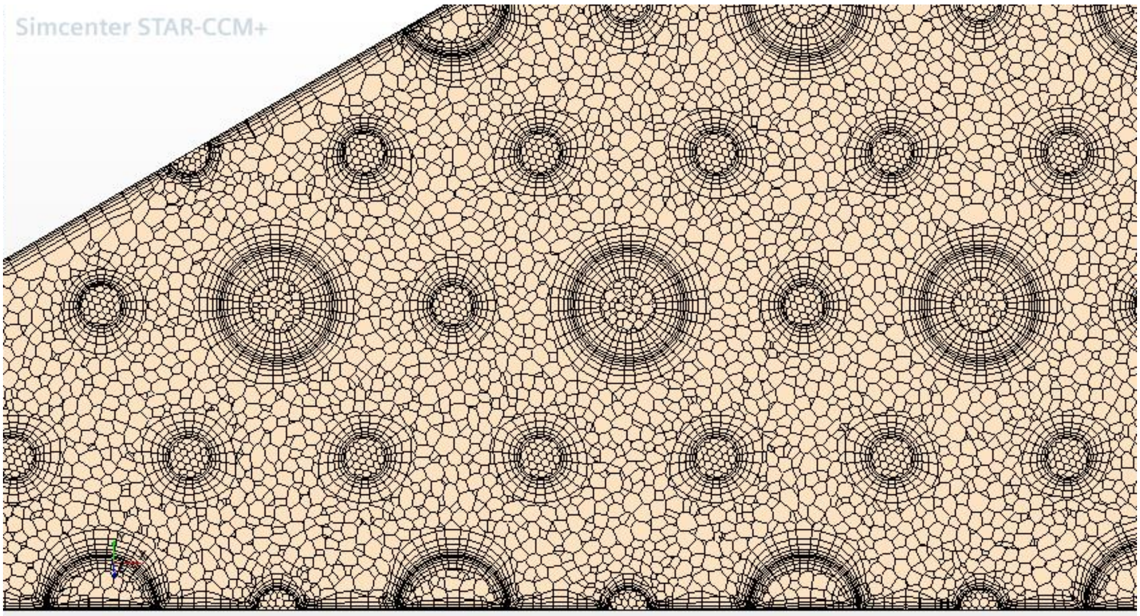

Figure 5.18: Mesh 2.

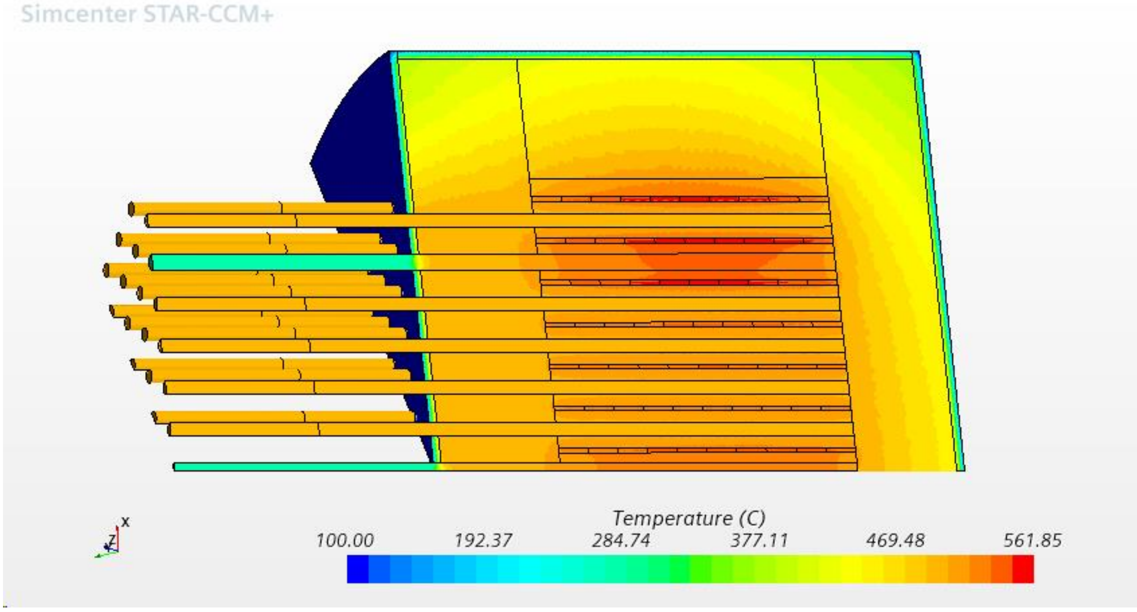

Figure 5.19: Temperature distribution at nominal state BOL Mesh 2.

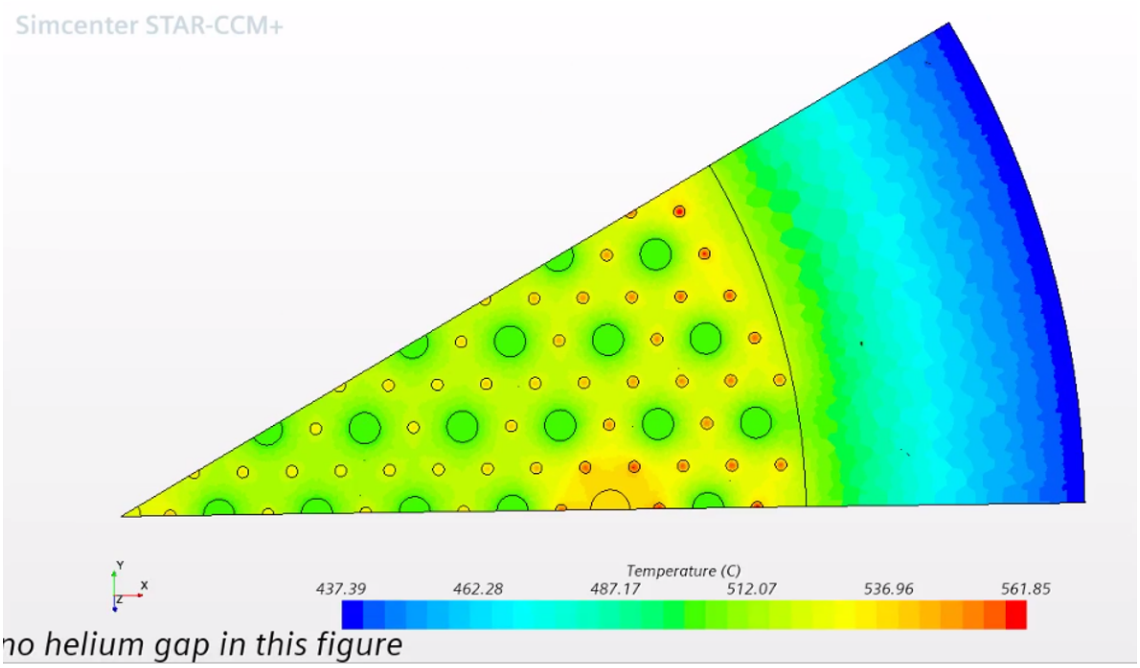

Figure 5.20: Cross-section at the middle of core at BOL in Mesh 2.

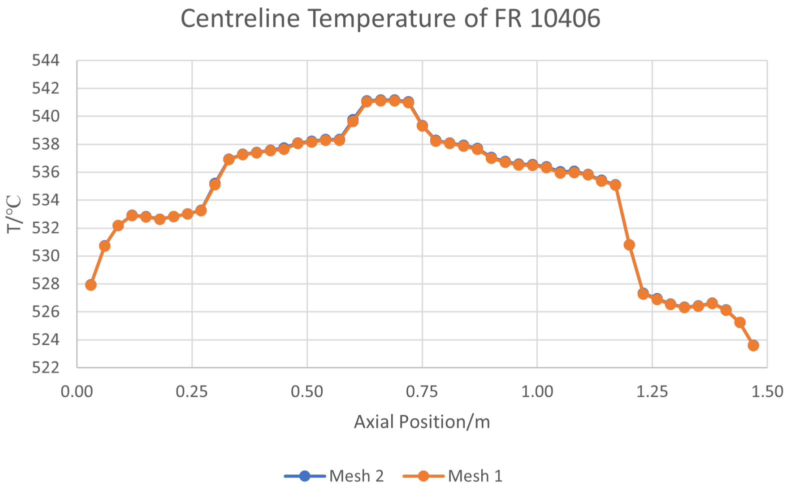

Figure 5.21: Fuel centreline temperatures at BOL of fuel rod 10406.

As shown in Figure 5.21, the segmented temperature profile is in alignment with the segmented geometry of fuel rods. Each of the fuel rods is divided into ten axial segments, and each segment has a different power density calculated by Serpent. All neutronics calculations presented in this work were performed with a Serpent model generated by

Sameer Reodikar [47], and carried out by him and other group members. The results were communicated to the author.

The fuel volume average temperature, power density, and temperature-to-power-density ratio distributions of row 01 are plotted axially in the following figures. It is observed that the profiles of temperature are smoother than those of power densities: the range of temperatures ($550 - 515 = 35$ °C, 6.4% of 550 °C) is smaller compared to their quantities than that of power densities ($10 - 3.9 = 6.1$ W/cc, 61% of 10 W/cc). This should be accounted by the independent heat transfer mechanism from the neutronics aspects.

At BOL, powers are higher at the outer region of the core and so are temperatures, which is because the poison is arranged in the inner region of the core to suppress the high power densities in the centre. The rod 10111 demonstrates a higher temperature profile than its outer neighbor 10113 since it is adjacent to a control rod instead of a heat pipe. Axially, the power densities and temperatures tend to be lower at the top of the core than at the bottom, which should be resulted from the vertical insertion of heat pipes and control rods through top reflector and the moderator block.

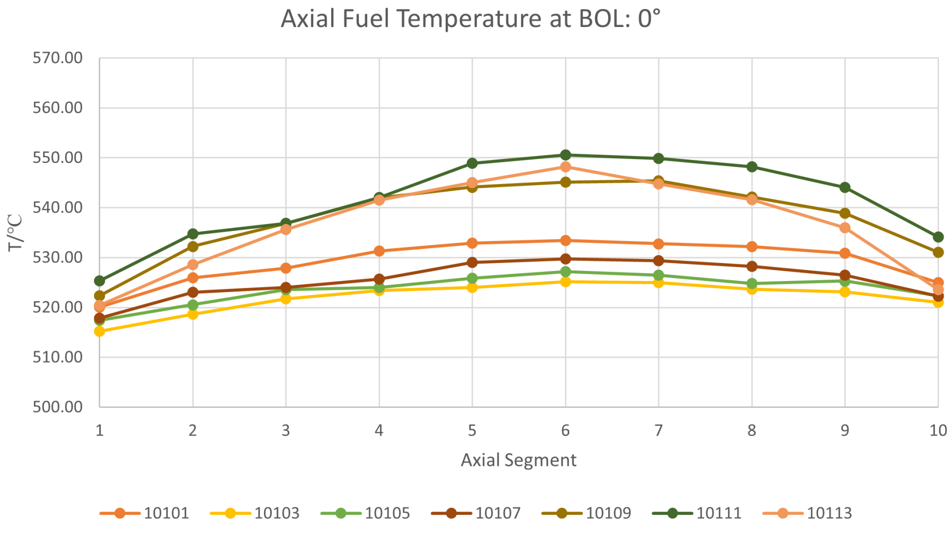

Figure 5.22: Axial fuel average temperature plot of row 01. Segment 1 is at the top of the core; segment 10 is at the bottom.

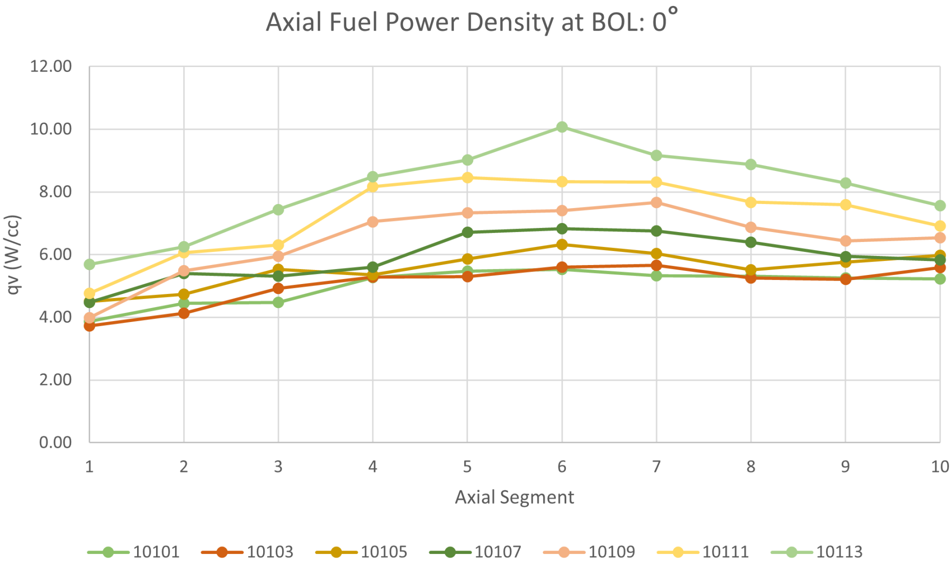

Figure 5.23: Axial fuel power density plot of row 01. Segment 1 is at the top of core; segment 10 is at the bottom. “cc” means cubic centimeter, cm^3.

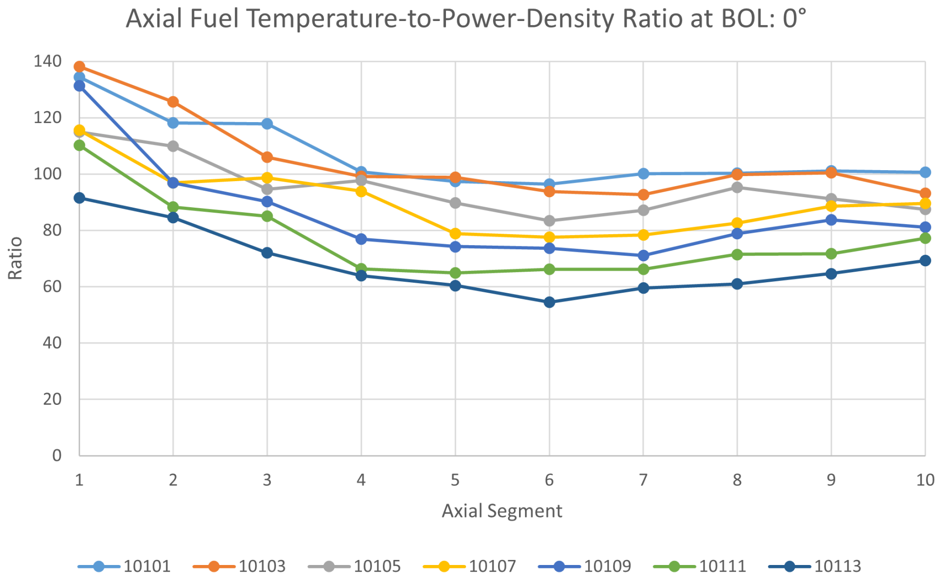

Figure 5.24: Axial fuel temperature-to-power-density plot of row 01. Segment 1 is at the top of core; segment 10 is at the bottom.

For the temperature-to-power-density ratios, the rods at the inner region have higher values than those at the outer region, indicating that for unit power generated in unit volume the inner rods tend to deposit more heat in fuel. This is to compensate for the lower power densities at the centre to reach a more uniform temperature distribution. Similarly, for the axial direction, the ratios are higher at the top in order to form a more symmetrical temperature distribution because of the lower power densities there.

5.4.2 Temperature Distributions at MOL and EOL

The temperature distributions at MOL and EOL are shown in the following figures and plots. As expected, the peak of power density as well as that of temperature migrate from the edge to the centre of core from BOL to EOL as the poison in the central region burns up.

In Figure 5.30, at EOL, the temperature profile of the central fuel rod 10101 and the side fuel rod 10113 depart significantly from those of other fuel rods. It is because for 10101, it is at the centre of the core and adjacent to a control rod which does not take away heat; when the maximum of power density moves to the central region, the temperatures of 10101 increase, and by virtue of its position next to a control rod the temperatures rise much higher than those of its neighbor fuel rod 10103.

As for 10113, it is the outmost rod in row 01 and sits next to a heat pipe, so when the peak of power moves into the reactor centre, its temperatures drop down; while for the adjacent fuel rod 10111 the temperatures decrease more slightly as it is positioned next to a control rod that doesn't take away heat. As a result, the temperatures of 10113 are substantially lower than the other rods.

We can also observe that at EOL the power density profile for each fuel rod differentiates significantly from each other in comparison with at MOL, which should be accounted for by the uneven accumulation of fission products, poison's function to depress central power and its depletion over reactor lifetime.

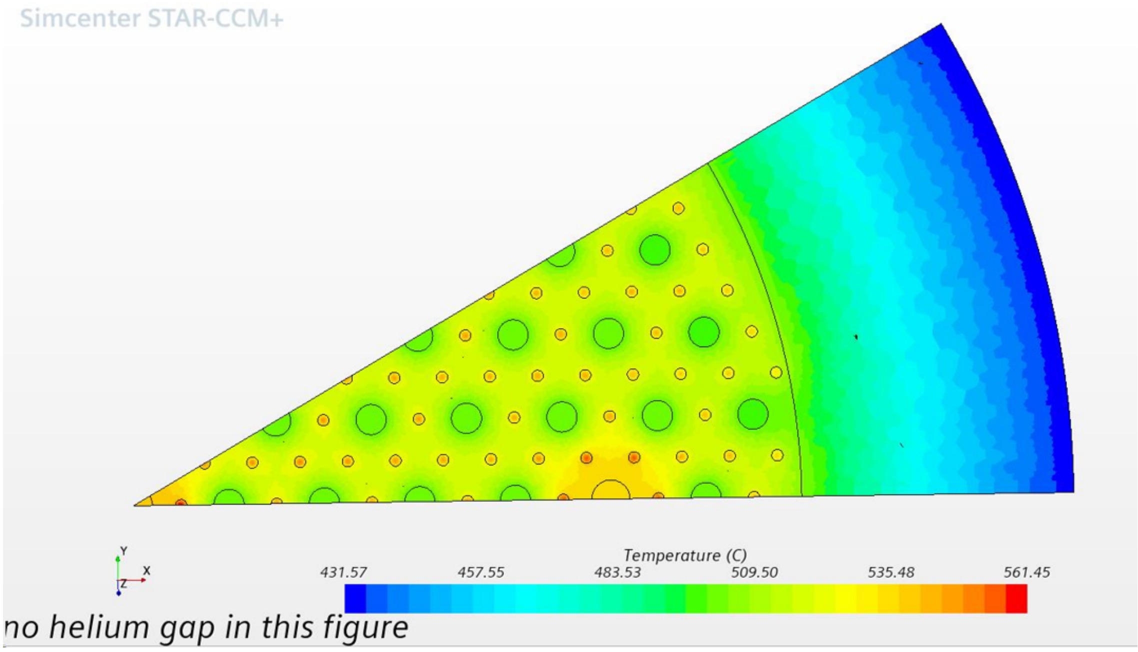

Figure 5.25: Heat map at MOL.

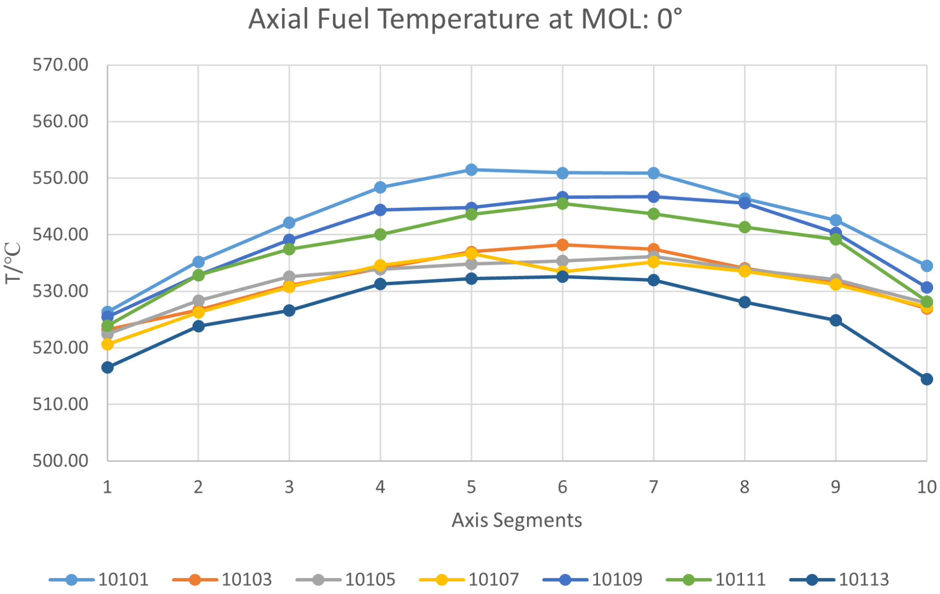

Figure 5.26: Axial fuel temperature plot at MOL.

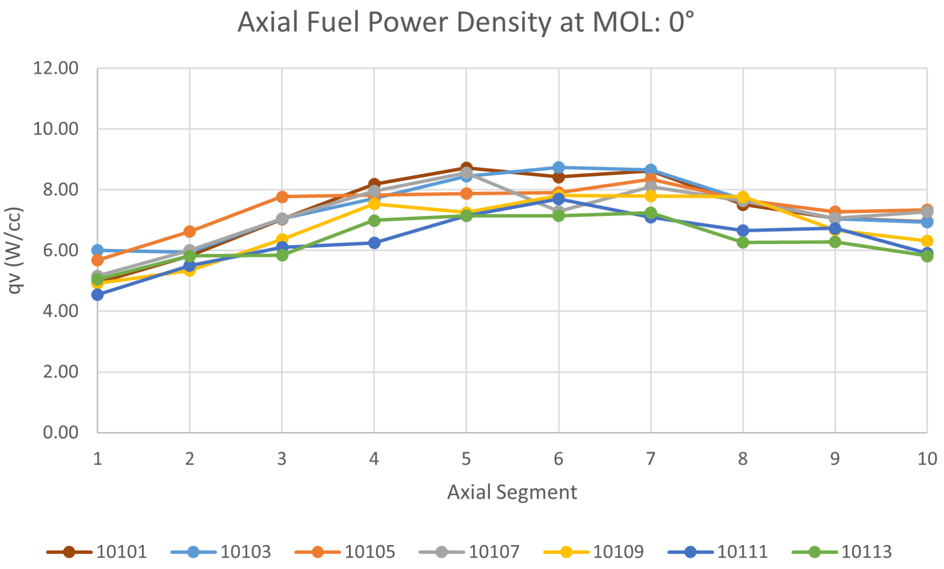

Figure 5.27: Axial fuel power density plot at MOL.

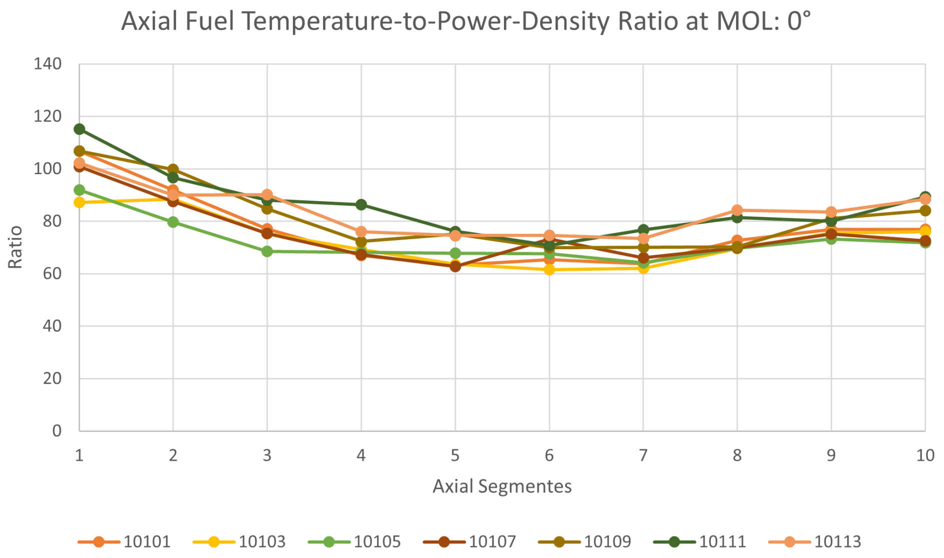

Figure 5.28: Axial fuel temperature-to-power-density ratio plot at MOL.

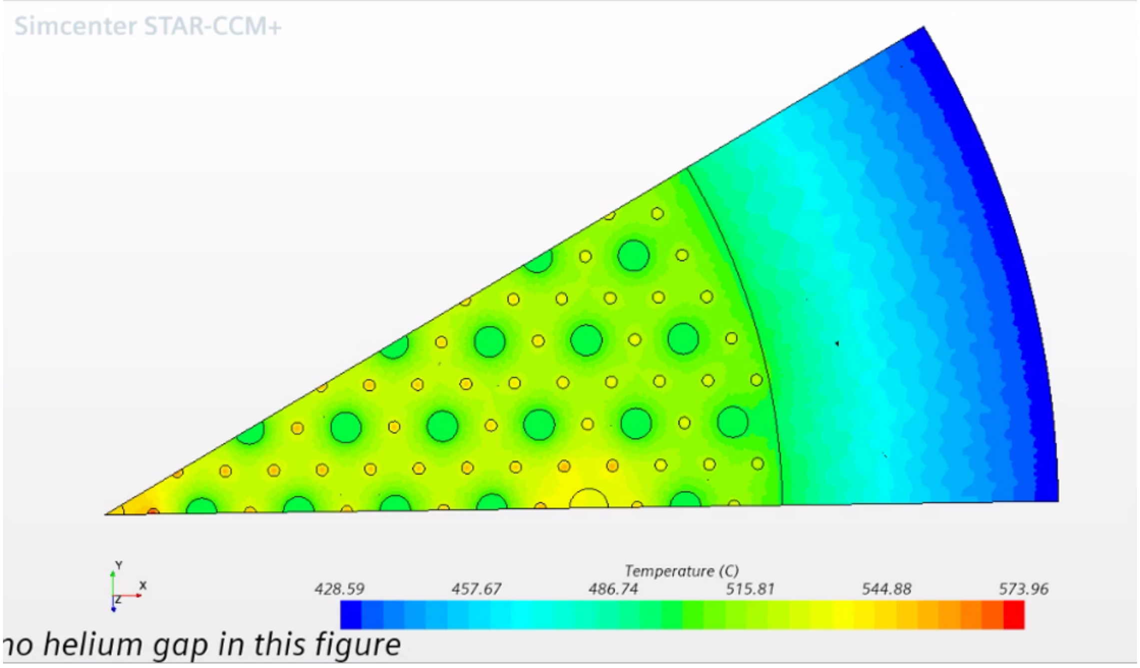

Figure 5.29: Heat map at EOL.

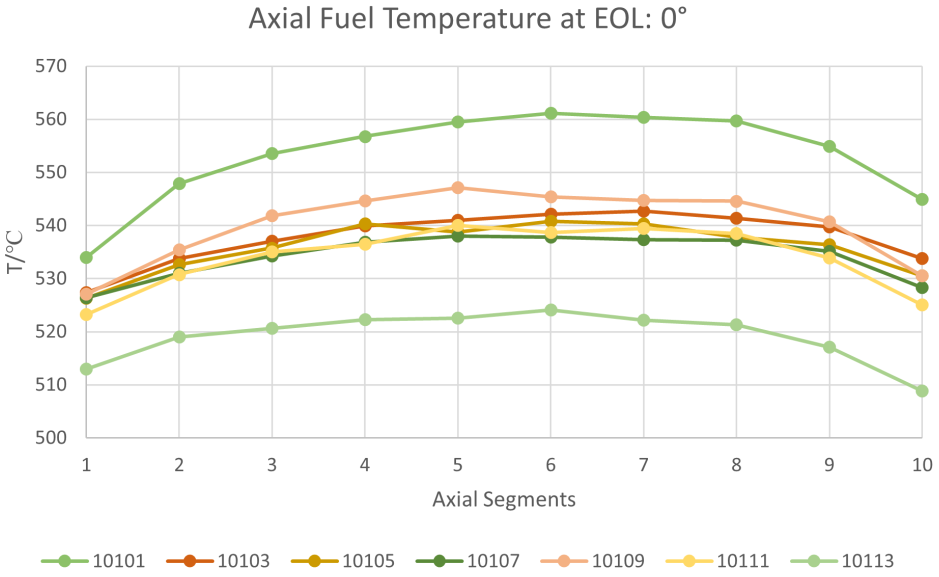

Figure 5.30: Axial fuel temperature plot at EOL.

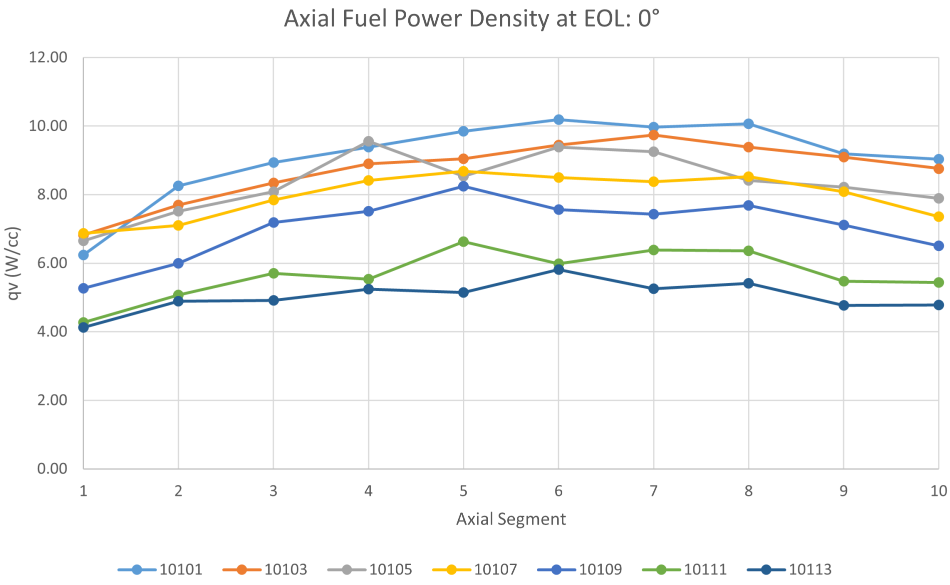

Figure 5.31: Axial fuel power density plot at EOL.

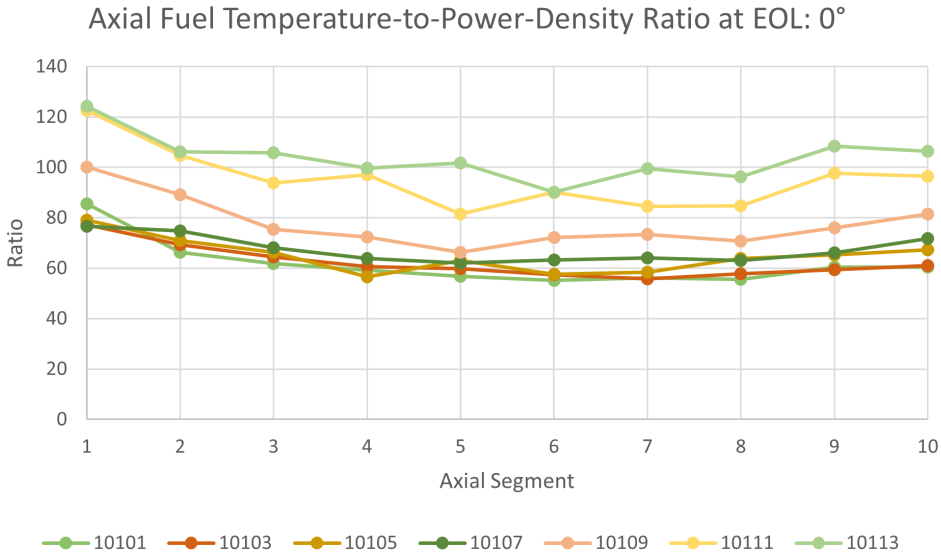

Figure 5.32: Axial fuel temperature-to-power-density ratio plot at EOL.

5.4.3 Heat Losses from Helium Cover Gas

There is a helium gap covering each of the top, bottom, and axial reflectors. The heat losses from various helium gaps and the total value are listed in Table 5.4.3. To be exact, those quantities are evaluated by the heat flows from reflectors to their respective covering helium gaps, because STAR-CCM+ can't produce the heat flux directly flowing out of the external surface of a helium gap since there is nothing in the environment for heat to flow to.

The total heat loss from helium gaps is 37.3 kW, and the total power generated by fuel in the 1/12 core model is 203 kW. The minor difference from one-twelfth nominal power, 200 kW, should be accounted for by the power fluctuation over reactor lifetime. When it comes to the whole core, the total heat loss from helium gaps would be 447 kW, 18.6% of nominal power (2,400 kWth). This is a high proportion to the total power, owing to the perfect heat transfer from the reflectors to the helium which is simulated as solid slabs in STAR-CCM+, and the condition of 100 °C set at the external surfaces of the helium gaps.

He Gap	Heat Loss (kW)
Top	8.8
Bottom	7.9
Radial	20.6
Total for 1/12 core	37.3
Total for whole core	447 (18.6% of nominal power)

Table 5.10: Heat losses at BOL from He gaps. The nominal power is 2,400 kWth.

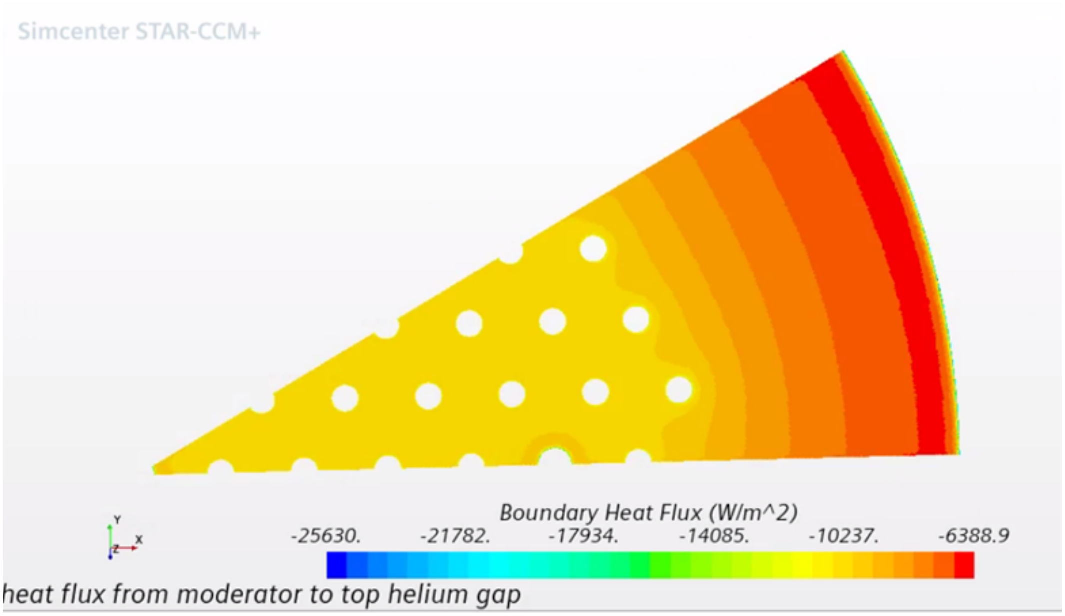

Figure 5.33: Heat flux from the top helium gap (the figure shows the interface of the helium gap in contact with the reflector, same with the following figures). The negative sign means heat flows into the helium gap.

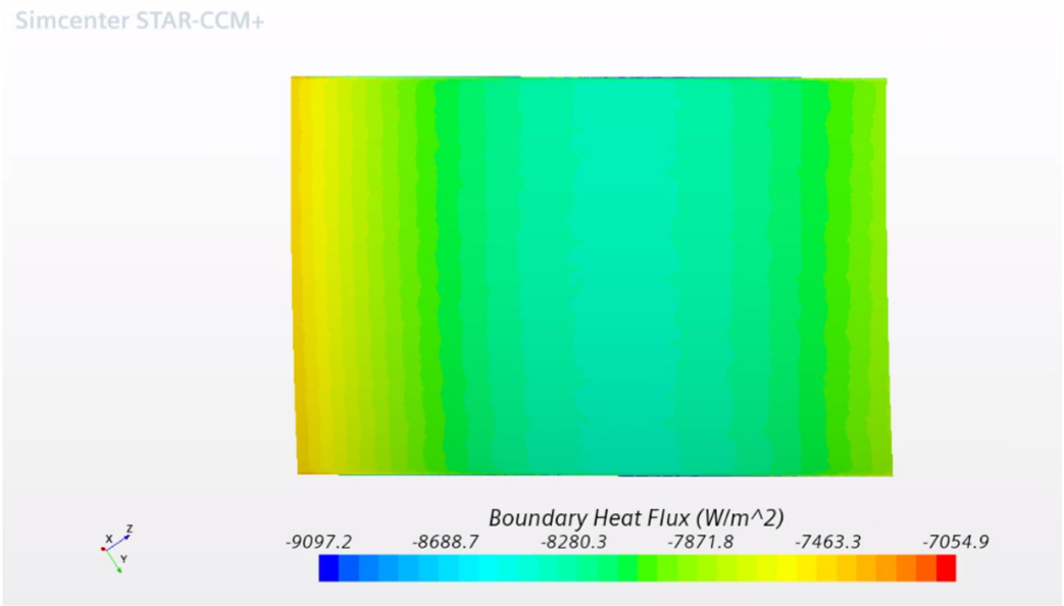

Figure 5.34: Heat flux from the radial helium gap. The negative sign means heat flows into the helium gap.

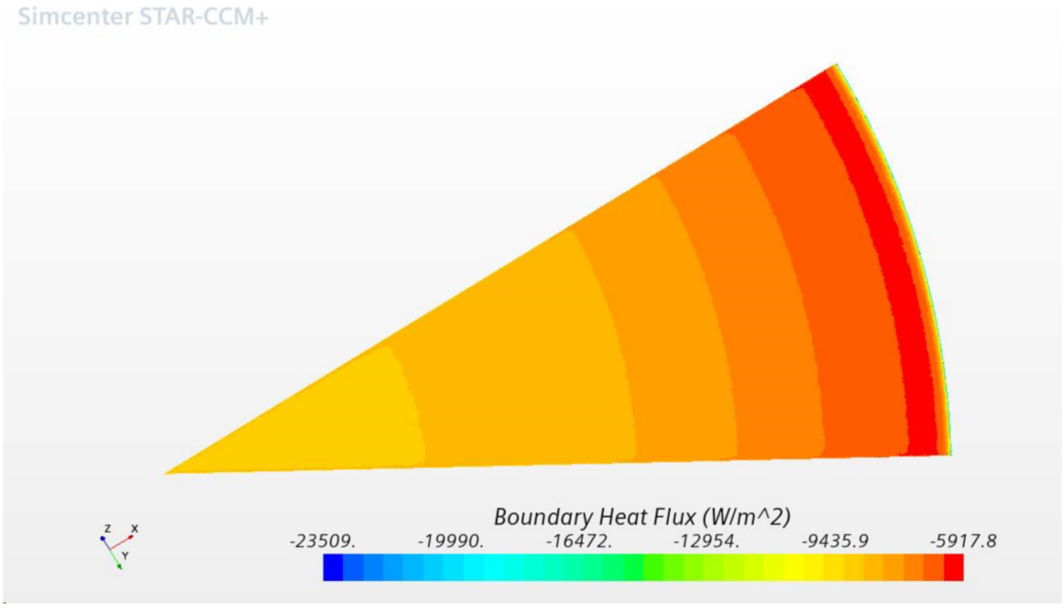

Figure 5.35: Heat flux from the bottom helium gap. The negative sign means heat flows into the helium gap.

5.4.4 Heat Pipe Power Distributions at BOL, MOL, and EOL

The heat pipe power distributions at BOL, MOL, and EOL are examined. Note that in the following figures, the powers of half heat pipes at the edge of 1/12 geometry are the values in their whole forms, i.e. the powers of half heat pipes are multiplied by two to get whole pipe powers. With burnup increasing, the maximum heat pipe power moves from the periphery to the centre of the core as expected.

At BOL, the maximum power $P_{\text{max}} = 16.6$ kW at heat pipe (HP) 10112, which is below the maximum operating power of the potassium heat pipe, 19 kW. The total heat pipe power in 1/12 core is 169.5 kW (half pipes remain as half values).

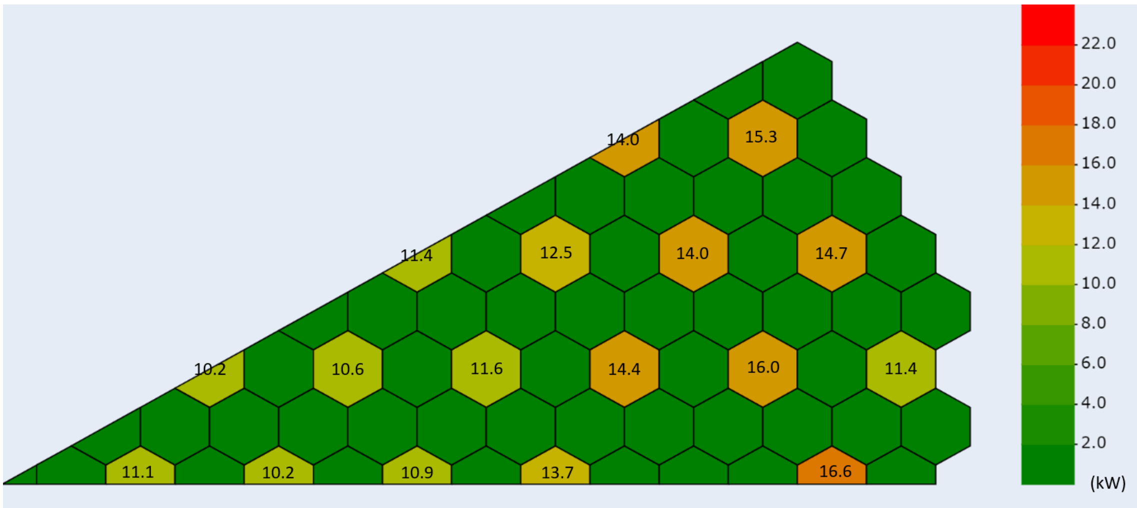

Figure 5.36: Heat pipe power distribution at BOL.

At MOL, the maximum power $P_{\text{max}} = 16.1$ kW at HP10308. The total heat pipe power in 1/12 core is 166.0 kW.

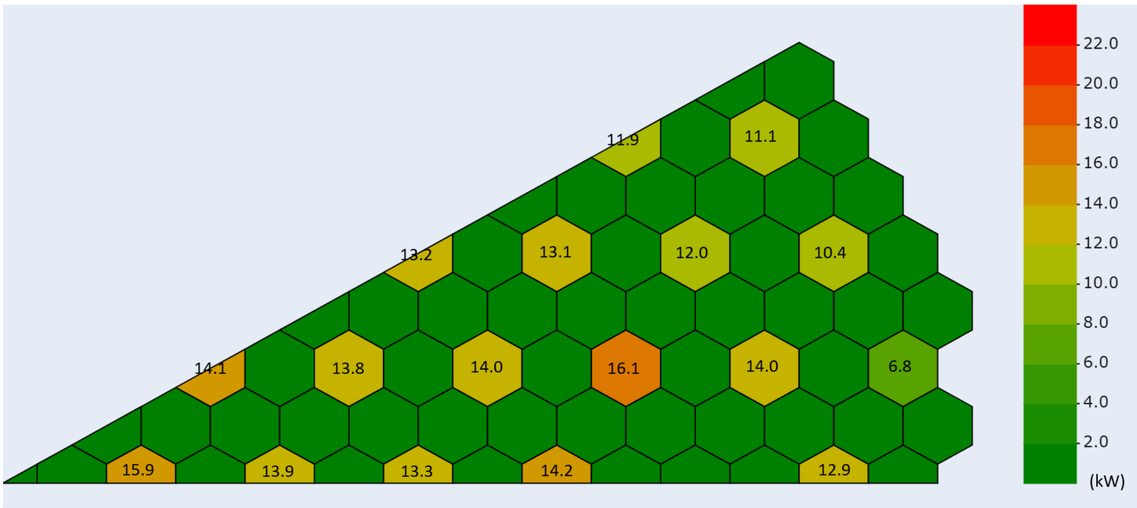

Figure 5.37: Heat pipe power distribution at MOL.

At EOL, the maximum power $P_{\text{max}} = 19.4$ kW at HP10102, slightly exceeding the maximum operation power. The total heat pipe power in 1/12 core is 166.3 kW.

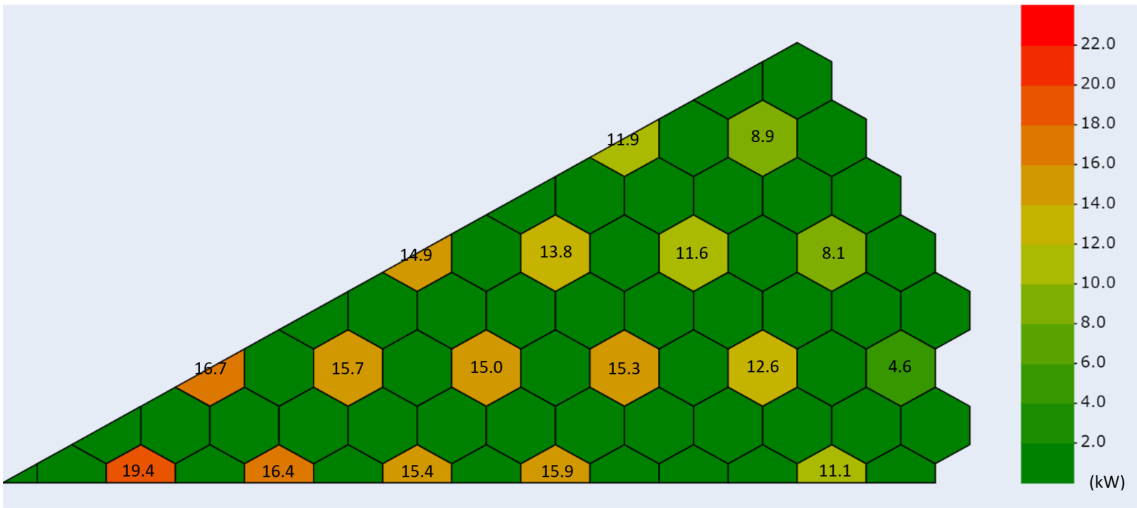

Figure 5.38: Heat pipe power distribution at EOL.

5.5 Heat Pipe Failure Accidents at BOL

Three heat pipe failure accidents at BOL are investigated in this section to evaluate the seriousness and the propagation of pipe failures in different scenarios. The failure of pipes is implemented by insulating the interfaces between the failed pipes and the core structures.

Heat Pipe Power Distribution at BOL: HP Failure 10112

The position where the power is zero indicates the failure pipe. In HP10112 failure accident $P_{\text{max}} = 18.9$ kW at 10310, which is at the maximum power of potassium heat pipe. The total heat pipe power in 1/12 core is 168.5 kW. Figure 5.40 shows the differences in powers between the accidental scenario and BOL nominal operation. The power of the failure pipe is mainly transferred to two adjacent pipes, 10104 and 10201, approximately 3 kW each. In this case, the heat pipe 10310 would probably fail after a certain time of operation, and may lead to consecutive pipe failures afterwards.

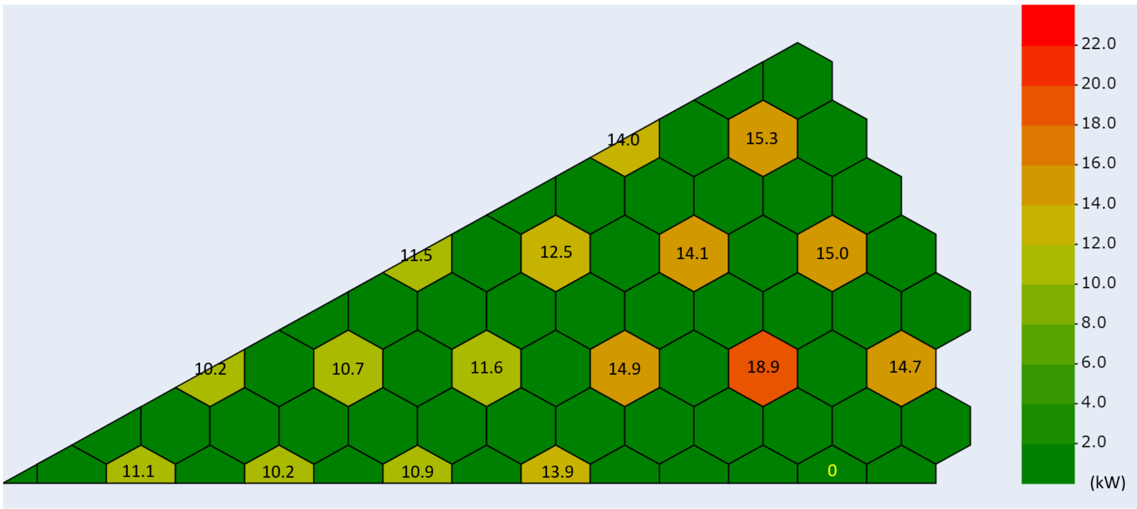

Figure 5.39: BOL HP10112 failure: heat pipe power distribution. 0 indicates the position of the failure pipe. $P_{\max} = 18.9$ kW at HP10310. Powers of half heat pipes are multiplied by 2.

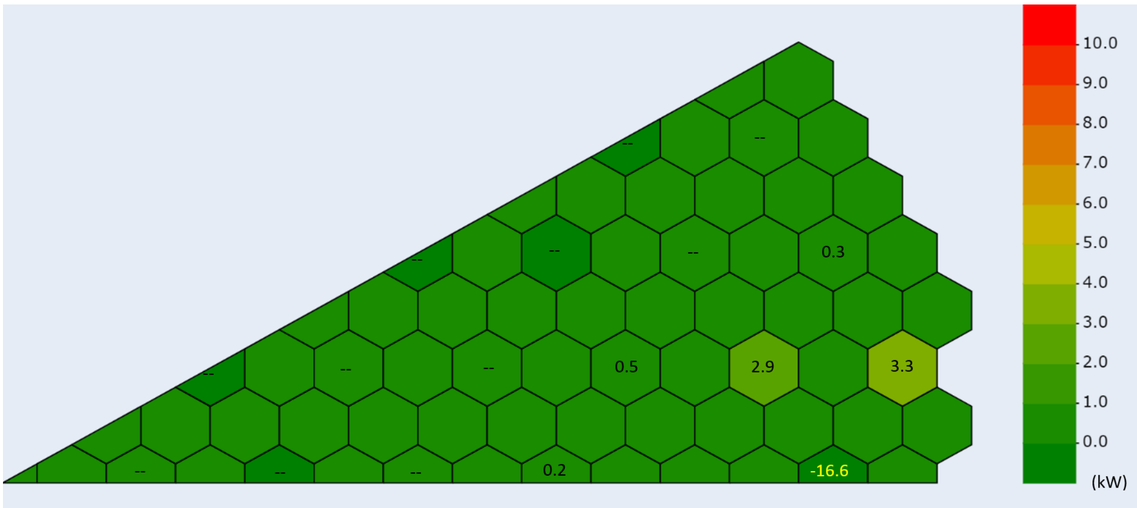

Figure 5.40: BOL HP10112 failure: heat pipe power differences between accidental scenario and normal operation. Half pipe values are multiplied by 2. "–" indicates the magnitude of the quantity is less than 0.1 kW. Total difference in 1/12 core = −0.9 kW (half pipes remain as half values), which should be accounted for by the simulation uncertainty of STAR-CCM+.

Heat Pipe Power Distribution at BOL: HP Failure 10310

For heat pipe failure 10310, $P_{\text{max}} = 22.3$ kW at HP10112, which exceeds the maximum power of the heat pipe. The total heat pipe power in 1/12 core is 168.2 kW. The power of the failure pipe is transferred to mainly five adjacent pipes, 10112 (5.8 kW), 10308 (3.1 kW), 10312 (2.8 kW), 10508 (2.5 kW), 10510 (2.5 kW). In this scenario, the heat pipe failure would propagate.

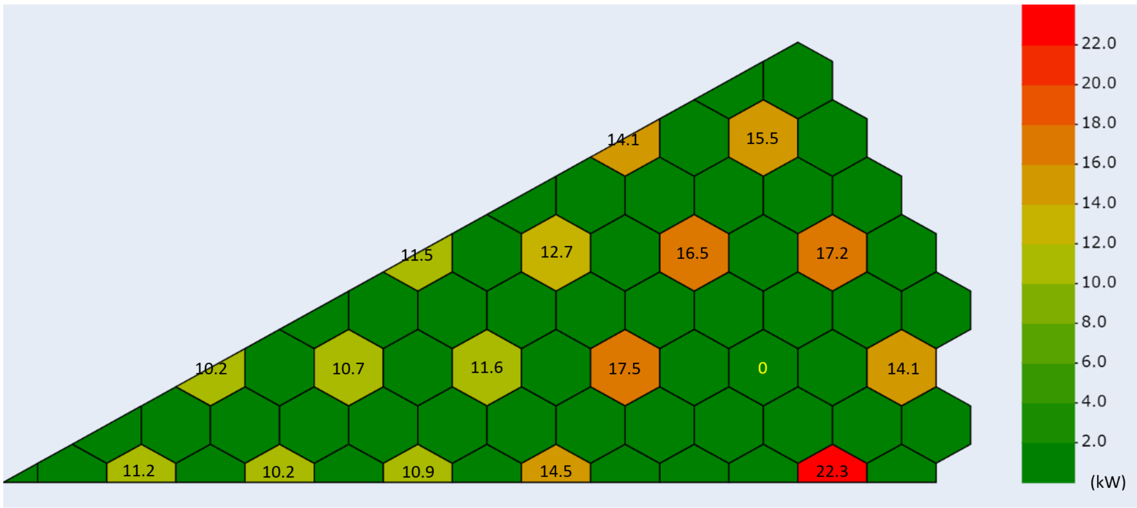

Figure 5.41: BOL HP10310 failure: heat pipe power distribution. $P_{\text{max}} = 22.3$ kW at HP10112. Powers of half heat pipes are multiplied by 2.

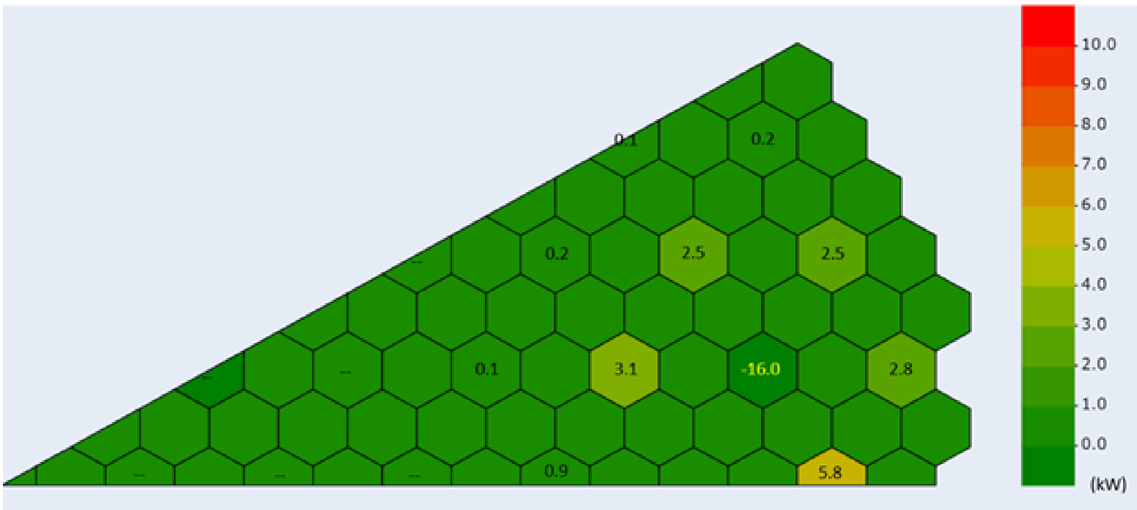

Figure 5.42: BOL HP10310 failure: heat pipe power differences between accidental situation and normal operation. Half pipe values are multiplied by 2. "–" indicates the magnitude of the quantity is less than 0.1 kW. Total difference in 1/12 core = −1.2 kW (half pipes remain as half values).

BOL: HP Failure 10112, 10310

For heat pipe failure accident 10112 and 10310, $P_{\max} = 19.8$ kW at HP10312, exceeding the maximum power of potassium heat pipe. Here we have another two pipes reaching the limit, HP10308 of 19.1 kW, and HP10510 of 18.4 kW. The total heat pipe power in 1/12 core is 167.1 kW. The power of the failure pipe is mostly transferred to four adjacent pipes, 10308 (4.7 kW), 10312 (8.4 kW), 10508 (3.3 kW), 10510 (3.7 kW).

In this case, four heat pipes would fail after 10112 and 10310, and then consecutive pipe failures would occur, destroying the primary heat transfer system of the core if no external measurements were taken.

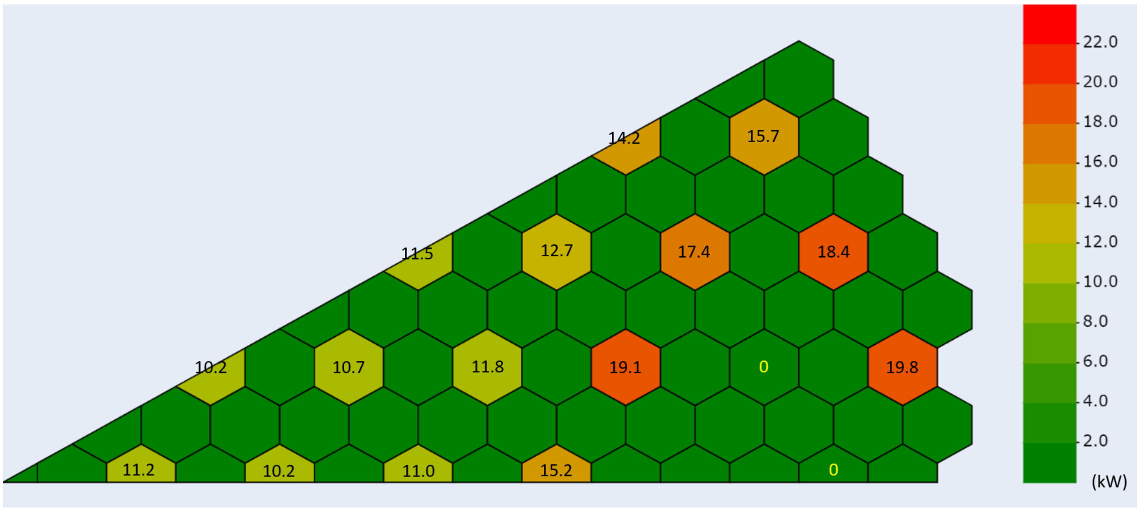

Figure 5.43: BOL HP10112, 10310 failure: heat pipe power distribution. $P_{\max}$= 19.8 kW at HP10312. Powers of half heat pipes are multiplied by 2.

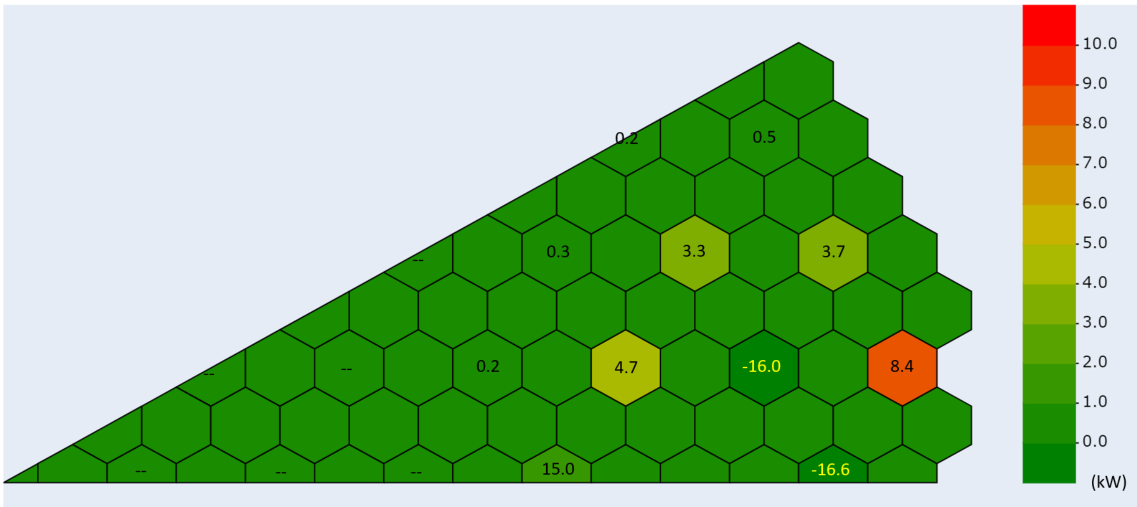

Figure 5.44: BOL HP10112, 10310 failure: heat pipe power differences between accidental situation and normal operation. Half pipe values are multiplied by 2. "–" indicates the magnitude of the quantity is less than 0.1 kW. Total difference in 1/12 core = -2.3 kW (half pipes remain as half values).

Chapter 6

Preliminary Neutronics Calculations

In this section, preliminary neutronics calculations of two hypothetical cases are carried out for the hexagonal unit cell (with one heat pipe and six half fuel rods) to evaluate the neutronics behaviours of the reactor:

- transient of double nominal power to examine the capability of temperature feedback to bring the reactivity down in case of power expedition
- power setback by 50% to evaluate the xenon behaviours in the reactor

Those calculations provide first information on the transient behaviours of the reactor core.

6.1 Double Power Transient

Recall the the point-kinetics equations in one energy group with one delayed neutron precursor group as discussed in Sec. 2.4 and 2.5 [29]:

$$\frac{\partial C}{\partial t} = \nu\beta\Sigma_\mathrm{f} v n - \lambda C, \tag{6.1}$$

$$\frac{\partial n}{\partial t} = \nu(1-\beta)\Sigma_\mathrm{f} v n - DB^2 v n - \Sigma_\mathrm{a} v n + \lambda C, \tag{6.2}$$

which can also be written in the form:

$$\frac{dn}{dt} = \frac{\rho-\beta}{\Lambda} n + \lambda C, \tag{6.3}$$

$$\frac{dC}{dt} = \frac{\beta}{\Lambda} n - \lambda C, \tag{6.4}$$

where Λ is the neutron generation time:

$$\Lambda = \frac{1}{\nu \Sigma_{\mathrm{f}} v}. \tag{6.5}$$

A general solution of n for the above equations can be derived when ρ is sufficiently small (typically $\rho < \frac{\beta}{2}$, including when $\rho < 0$):

$$n(t) = \frac{\beta}{\beta - \rho} e^{\frac{\lambda \rho}{\beta - \rho} t} - \frac{\rho}{\beta - \rho} e^{\frac{\rho - \beta}{\Lambda} t}. \tag{6.6}$$

Constant	Value
β	0.006
ρ/mk	-8.6
λ/s^{-1}	0.1
Λ/s	0.001

Table 6.1: Constants of point kinetics

The parameters used in the calculation are presented in Table 6.1. The reactivity value of -8.6 mk comes from evaluating the changes in temperature of fuel and moderator between the nominal state and the double power state from Serpent calculations with the temperature coefficients of reactivity. Fig. 6.1 shows the development of neutron density during the transient calculated with Eq. 6.6, which indicates that the negative feedback by temperature is sufficient to bring the reactor power down to normal level.

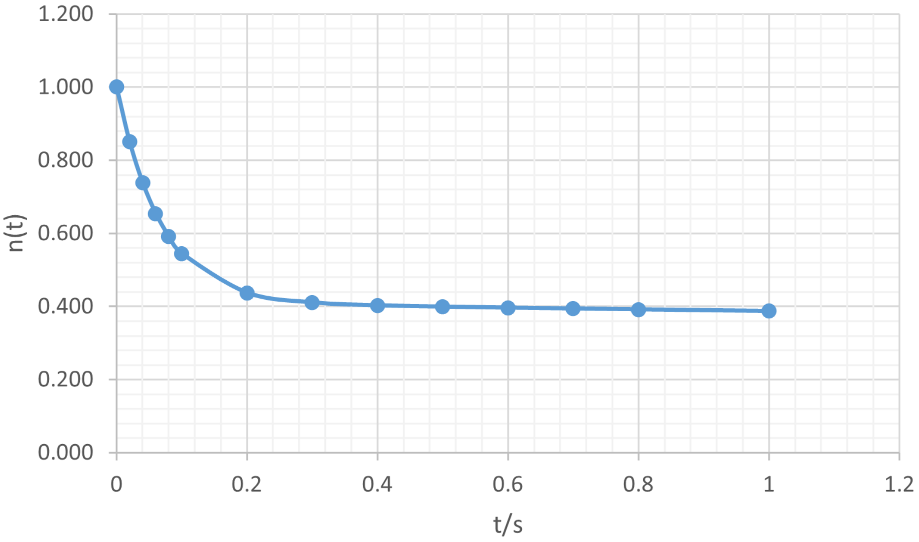

Figure 6.1: Time plot of power doubling transient calculated by point kinetics. The power is considered to multiply instantly. n(0) = 1 corresponds to the double power state.

6.2 50% Power Setback with Xenon

Xe-135 is an important saturating fission product in nuclear reactors. The name "saturating fission product" means its concentration depends on reactor power and approximates to a certain level asymptotically when neutron flux is approaching infinite. It has large absorption cross sections adding a significant amount of negative reactivity to the reactor.

Xe-135 has two ways of production and two ways of destruction. For production:

- prompt generation in fission as a fission product
- I-135 decay with a half-life of 6.585 h

in which I-135 decay is the major source of Xe-135 for most thermal reactors (∼96% in CANDU) [29].

For destruction:

- burnout by neutron absorption
- Xe-135 decay by itself with a half-life of 9.169 h

in which burnout by neutron absorption dominates the destruction of neutrons for most thermal reactors (∼91% in CANDU).

The differential equations describing xenon and iodine production and removal rates are [29]:

$$\frac{dI}{dt} = \gamma_{\mathrm{I}}\Sigma_{\mathrm{f}}\phi - \lambda_{\mathrm{I}}I, \tag{6.7}$$

$$\frac{dX}{dt} = \lambda_{\mathrm{I}}I + \gamma_{\mathrm{X}}\Sigma_{\mathrm{f}}\phi - \lambda_{\mathrm{X}}X - \sigma_{\mathrm{X}}X\phi, \tag{6.8}$$

where

I	I-135 concentration
X	Xe-135 concentration
γ_{I}	number of I-135 produced per fission
γ_{X}	number of Xe-135 produced per fission
λ_{I}	decay constant of I-135
λ_{X}	decay constant of Xe-135
σ_{X}	absorption cross section of Xe-135

From the coupled equations the steady-state values of iodine and xenon can be calculated by equating the time derivatives to zero:

$$I_{\mathrm{ss}} = \frac{\gamma_{\mathrm{I}}\Sigma_{\mathrm{f}}\phi_{\mathrm{ss}}}{\lambda_{\mathrm{I}}}, \tag{6.9}$$

$$X_{\mathrm{ss}} = \frac{(\gamma_{\mathrm{I}} + \gamma_{\mathrm{X}})\Sigma_{\mathrm{f}}\phi_{\mathrm{ss}}}{\lambda_{\mathrm{X}} + \sigma_{\mathrm{X}}\phi_{\mathrm{ss}}}. \tag{6.10}$$

The subscript "ss" refers to steady state. The relation to calculate xenon load from the instantaneous value of X is:

$$\rho_{\mathrm{X}} = \frac{X}{X_{\mathrm{ss,fp}}} * \rho_{\mathrm{X,fp}}, \tag{6.11}$$

where the subscript "fp" means full-power nominal operation. Another formula to calculate reactivity load is [48]:

$$\rho_{\mathrm{X}} = -\frac{\sigma_{\mathrm{X}}X}{\nu\Sigma_{\mathrm{f}}}, \tag{6.12}$$

which is used to calculate the initial full-power (nominal power) xenon load.

The axial and radial neutron fluxes in CNB are to be as shown in Figure 6.2:

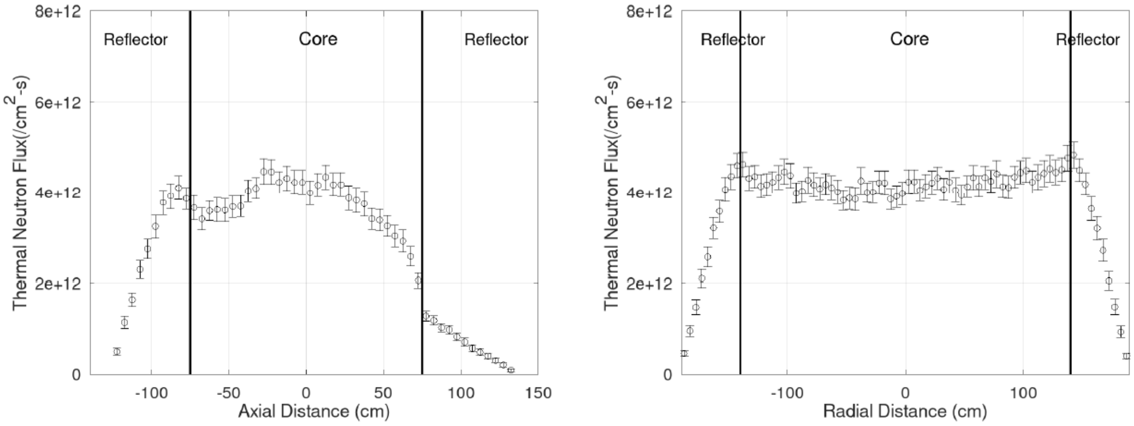

(a) Centerline Axial Flux (b) Centerline Radial Flux

Figure 6.2: Neutron flux at BOL produced by another team member, Sameer Reodikar [31].

The neutron flux at BOL is approximated to be $\phi(\text{BOL}) = 4 \times 10^{12}$ n/cm^2-s. The iodine, xenon concentrations, and reactivity load are calculated with constants in Table 6.2 and are shown in Table 6.3.

Constant	Value
$E(500\ ^\circ\text{C})/\text{eV}$	0.067
$\lambda_\text{I}/\text{s}^{-1}$	2.92e-5
$\lambda_\text{X}/\text{s}^{-1}$	2.10e-5
γ_I	0.0638
γ_X	0.00246
$\sigma_\text{X}/\text{cm}^2$	2.93e-18
$\sigma_{235\text{U}}/\text{cm}^2$	3.35e-22
$\Sigma_\text{f}/\text{cm}^{-1}$	4.49e-3
$\phi(\text{BOL})/(\text{n/cm}^2\text{-s})$	4.00e12

Table 6.2: Constants used in xenon calculation. The neutron energy and cross sections are evaluated at 500 °C (773 K). Σ_f is calculated by assuming a uniform core. Fission is only considered for U-235 in a fresh core.

Quantity	Value
$I_{\text{ss,fp}}/(\text{n/cm}^3)$	3.93e13
$X_{\text{ss,fp}}/(\text{n/cm}^3)$	3.64e13
$\rho_{\text{ss,fp}}/\text{mk}$	-9.9

Table 6.3: Calculated quantities related to xenon load at steady-state full-power operation at BOL.

The macroscopic fission cross section of the cell is atom quantity averaged value with only U-235 fission assuming fresh fuel:

$$\Sigma_{\text{f}} = \sigma_{\text{f}} n(235\text{U}) = \sigma_{\text{f}} \frac{N(235\text{U})}{V_{\text{cell}}}. \tag{6.13}$$

Here the volume of the hexagonal unit cell involves the heat pipe but no reflectors.

6.2.1 50% Setback: Analysis and Comparison with CANDU

The xenon production and destroy rates are evaluated for CNB and compared with CANDU at the steady state operation (Table 6.4) and the 50% power setback transient (Table 6.5). Note that both reactors are assumed to be homogeneous and the concentrations are for homogeneous cores as well.

The iodine concentration, xenon prompt production rate as well as the xenon burnout rate are smaller in CNB because of the lower neutron flux level. The xenon load is also lower in CNB, which should be related to the higher macroscopic fission cross section stemming from the larger U-235 enrichment compared to the natural enrichment in CANDU (Eq. 6.12). However, the xenon concentrations are similar in the two reactors due to the saturating feature, and as a result the xenon decay rates are similar in the both reactors.

It is also noticed that the major way of xenon destruction for CNB is by xenon decay, instead of burnout by neutron absorption in the case of CANDU. The burnout rate only counts for 36% in the total destruction rate. Consequently, for CNB, the capability of neutron flux to decrease xenon destruction by burnout is weaker during a power setback; the total xenon destruction is larger right after the power drop and the concentration is sustained at a lower level.

As explained above, smaller and slower changes in xenon concentration and reactivity load after the power setback are expected in CNB.

Steady-State	CNB	CANDU [29]	CNB/CANDU
$\phi_{\text{ss,fp}}$ (n/cm^2-s)	4.00e12	7.00e13	0.06
$I_{\text{ss,fp}}$ (n/cm^3)	3.93e13	3.06e14	0.13
$X_{\text{ss,fp}}$ (n/cm^3)	3.64e13	3.78e13	0.96
$\rho_{\text{X,fp}}$ (mk)	-9.9	-28	0.35
I decay rate (n/cm^3-s)	1.15e9	8.93e9	0.13
Xe prompt production (n/cm^3-s)	4.42e7	3.44e8	0.13
Xe burnout rate (n/cm^3-s)	4.27e8	8.48e9	0.05
Xe decay rate (n/cm^3-s)	7.65e8	7.95e8	0.96
Xe burnout/total destruction	0.36	0.92	N/A
Xe total production (n/cm^3-s)	1.19e9	9.27e9	0.13
Xe total destruction (n/cm^3-s)	1.19e9	9.27e9	0.13

Table 6.4: Neutronics and xenon quantities at steady-state full-power operation of CNB and CANDU assuming a homogeneous core for both reactors.

50% Setback	CNB	Setback/Steady	CANDU	Setback/Steady
ϕ (n/cm^2-s)	2.00e12	0.5	3.50e13	0.5
I (n/cm^3)	–	1	–	1
X (n/cm^3)	–	1	–	1
ρ_X (mk)	–	1	–	1
I decay rate (n/cm^3-s)	–	1	–	1
Xe prompt production (n/cm^3-s)	2.21e7	0.5	1.72e8	0.5
Xe burnout rate (n/cm^3-s)	2.13e8	0.5	4.24e9	0.5
Xe decay rate (n/cm^3-s)	–	1	–	1
Xe burnout/total destruction	0.22	N/A	0.84	N/A
Xe total production (n/cm^3-s)	1.17e9	0.98	9.10e9	0.98
Xe total destruction (n/cm^3-s)	9.78e8	0.82	5.04e9	0.54

Table 6.5: Neutronics and xenon quantities immediately after 50% setback in CNB and CANDU assuming homogeneous core for both reactors. "–" means the quantity is or nearly is unchanged right after the power drop.

6.2.2 50% Setback: Simulation Methodology

The transient of 50% power setback is simulated by written code in Octave to observe the evolution of quantities. The timescale of xenon transient is in hours, while for neutronics the timescale is in seconds. Because of the large difference, to neutrons the evolution process of xenon is imperceptible. From this neutrons are assumed to be at equilibrium state at the beginning and the end of each timestep in the timescale of xenon, and are considered to evolve by successive prompt drops following small power setbacks:

$$\frac{n}{n_\mathrm{ss}} = \frac{\beta}{\beta - d\rho}. \tag{6.14}$$

Subscript "ss" refers to the last steady state and is taken as the end of last timestep in the scale of xenon transient. $d\rho$ is the change in reactivity in current timestep, containing both xenon feedback $d\rho_\mathrm{X}$ and temperature feedback $d\rho_\mathrm{T}$. For this relation to be viable, the timestep dt must be larger than about 2 min, since this is the approximate magnitude of the stable period of a typical reactor; and shouldn't bee too large because the xenon load variation in each step should be reasonably small (say, $d\rho_\mathrm{X} < \frac{\beta}{2}$) since Eq. 6.14 is derived for small reactivity values as discussed in Sec. 2.5, and large reactivities induce large variations potentially breaking down the steady-state approximation at the onset and the end of prompt drop.

At the start and the end of each timestep, the neutrons are regarded to be at equilibrium, which means the reactivity is zero and each step only sees the reactivity induced by xenon concentration change as well as the temperature feedback in current step. At the beginning of each timestep i, the neutrons start at an old equilibrium established at the end of i − 1; during timestep i, neutrons are considered to respond to the change in reactivity instantly through prompt drop, and finally a new equilibrium is attained at the end of i.

In order to calculate the temperature feedback, the power change needs to be evaluated at each timestep. The continuity equation describes the relation among the time derivative of temperature, divergence of heat flux, as well as the heat source within a volume:

$$C_{\mathrm{p}} * \frac{\partial T}{\partial t} + \nabla \cdot \vec{J_{\mathrm{u}}} = q_{\mathrm{v}}, \tag{6.15}$$

where J_{u} is heat flux, q_{v} is volumetric heat density, C_{p} is heat capacity. Integrating over the volume of the unit cell:

$$C_{\mathrm{cell}} * l = \Delta P, \tag{6.16}$$

$$l = \frac{\partial T}{\partial t}, \tag{6.17}$$

where C_{cell} is the total heat capacity of the unit cell and is 1.4×10^5 J/K, l is the time derivative of temperature.

The flow chart of the code is presented in Figure 6.3. The code first evaluates the iodine concentration I, xenon concentration X, xenon load ρ_{X}, as well as the reactivity increment in xenon load $d\rho_{\mathrm{X}}$ in the current step; then the neutron density n is calculated by prompt drop with reactivity $d\rho_{\mathrm{X}}$, and the corresponding neutron flux ϕ, power change dP, temperature change dT are determined; after that, the resulted temperature feedback $d\rho_{\mathrm{T}}$ from dT is calculated with the temperature coefficient, and the step reactivity $d\rho$ is corrected with $d\rho_{\mathrm{T}}$ ($d\rho = d\rho_{\mathrm{X}} + d\rho_{\mathrm{T}}$); finally the neutron density n is reevaluated with the new reactivity through prompt drop, and the flux ϕ, power P, and temperature T are updated accordingly which are the final values at the timestep. The script can be found in Appendix E.

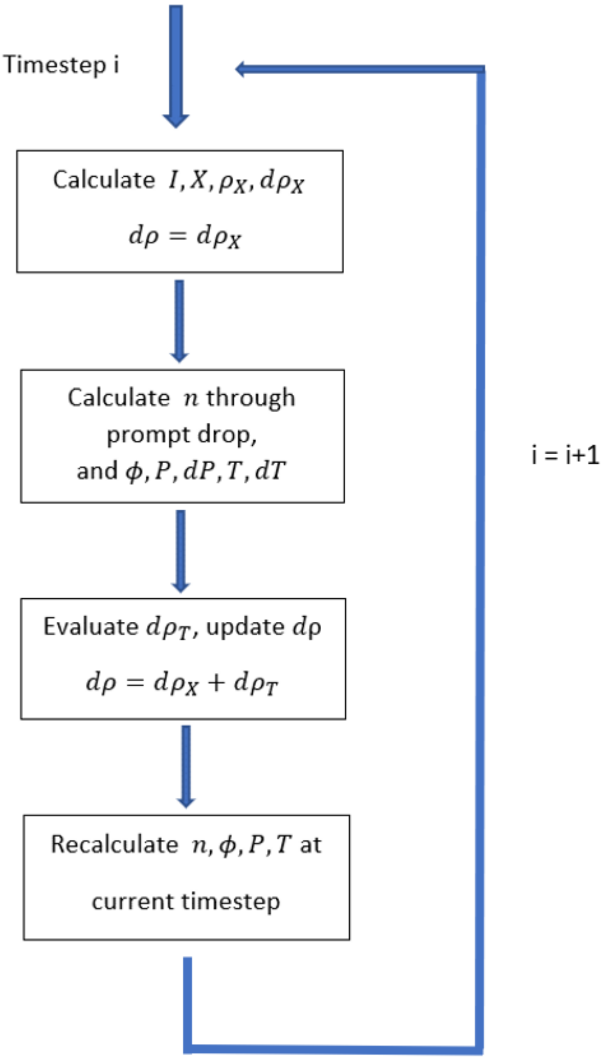

Figure 6.3: Flow chart of the setback transient code.

The thermodynamics is considered to be quasi-static under the timescale of xenon evolution, which means the heat generated in fuel is regarded to spread into the graphite moderator timely and adequately; the heat transfer to the secondary loop is also perfect. As a result, the temperature feedback can be considered to happen in the whole cell in stead of locally in fuel (this is in accordance with the assumption of homogeneous cell), and is dominated by graphite temperature coefficient C_{TGr} due to its large proportion.

The equations used in the code are listed here in order. First evaluate the iodine concentration and xenon concentration with information from the last step:

$$I = I_{\mathrm{ss}} + dt * (\gamma_{\mathrm{I}}\Sigma_{\mathrm{f}}\phi_{\mathrm{ss}} - \lambda_{\mathrm{I}}I_{\mathrm{ss}}), \tag{6.18}$$

$$X = X_{\mathrm{ss}} + dt * (\lambda_{\mathrm{I}}I_{\mathrm{ss}} + \gamma_{\mathrm{X}}\Sigma_{\mathrm{f}}\phi_{\mathrm{ss}} - \lambda_{\mathrm{X}}X_{\mathrm{ss}} - \sigma_{\mathrm{X}}X_{\mathrm{ss}}\phi_{\mathrm{ss}}). \tag{6.19}$$

Note again the subscription “ss” refers to the last steady state and is taken as the end of last timestep. Calculate the xenon load and its step change in current timestep:

$$\rho_{\mathrm{X}} = \rho_{\mathrm{X,fp}} * \frac{X}{X_{\mathrm{ss,fp}}}, \tag{6.20}$$

$$d\rho_{\mathrm{X}} = \rho_{\mathrm{X}} - \rho_{\mathrm{X,ss}}. \tag{6.21}$$

Calculate the neutron density by prompt drop and the corresponding power and temperature:

$$n = n_{\mathrm{ss}} * \frac{\beta}{\beta - d\rho_{\mathrm{X}}}, \tag{6.22}$$

$$P = P_{\mathrm{ss,fp}} * \frac{n}{n_{\mathrm{ss,fp}}}, \tag{6.23}$$

$$dP = P - P_{\mathrm{ss}}, \tag{6.24}$$

$$l = \frac{dP}{C_{\mathrm{cell}}}, \tag{6.25}$$

$$dT = l * dt, \tag{6.26}$$

$$T = T_{\mathrm{ss}} + dT, \tag{6.27}$$

The reactivity feedback from temperature is:

$$d\rho_{\mathrm{T}} = C_{\mathrm{TGr}} * dT. \tag{6.28}$$

Recalculate the step reactivity $d\rho$, neutron density n, flux ϕ, cell power P, and temperature T in the current step. Note that neutrons only see the reactivity in the current step:

$$d\rho = d\rho_{\mathrm{X}} + d\rho_{\mathrm{T}}, \tag{6.29}$$

$$n = n_{\mathrm{ss}} * \frac{\beta}{\beta - d\rho}, \tag{6.30}$$

$$\phi = \phi_{\mathrm{ss,fp}} * \frac{n}{n_{\mathrm{ss,fp}}}, \tag{6.31}$$

$$P = P_{\mathrm{ss,fp}} * \frac{n}{n_{\mathrm{ss,fp}}}, \tag{6.32}$$

$$dP = P - P_{\mathrm{ss}}, \tag{6.33}$$

$$l = \frac{dP}{C_{\mathrm{cell}}}, \tag{6.34}$$

$$dT = l * dt, \tag{6.35}$$

$$T = T_{\mathrm{ss}} + dT. \tag{6.36}$$

The subscription "ss, fp" refers to the steady-state full-power operation (core power 2,4000 kWth, cell power 20.2 kWth). $n_{\mathrm{ss,fp}}$ is taken as 1 for simplicity.

At t = 0 s, the core is considered to have become stable after the setback, and the level of neutron concentration is 50% of the steady-state full-power level which already includes the effect from temperature feedback. The initial conditions are:

$$n(0) = 0.5n_{\mathrm{ss,fp}}, \tag{6.37}$$

$$P(0) = 0.5P_{\mathrm{ss,fp}}, \tag{6.38}$$

$$\phi(0) = 0.5\phi_{\mathrm{ss,fp}}, \tag{6.39}$$

$$I(0) = I_{\mathrm{ss,fp}}, \tag{6.40}$$

$$X(0) = X_{\mathrm{ss,fp}}. \tag{6.41}$$

$$\rho_{\mathrm{X}}(0) = \rho_{\mathrm{X,fp}}. \tag{6.42}$$

Since the neutrons are regarded to be at equilibrium at t = 0 s, the reactivity:

$$\rho(0) = 0. \tag{6.43}$$

Parameters of the unit cell used in the calculation is summarized in Table 6.6.

Parameter	Value
$C_{\mathrm{TGr}}/(\mathrm{mk/K})$	-9.19e-2
$C_{\mathrm{cell}}/(\mathrm{J/K})$	1.4e15
$P_{\mathrm{ss,fp}}/\mathrm{kW}$	20.2
$V_{\mathrm{cell}}/\mathrm{m}^3$	0.052

Table 6.6: Core parameters. V_{cell} is the volume of the hexagonal unit cell within the core (with the height of fuel rods).

6.2.3 Results and Plots

The transient is simulated over a time period of 30 h = 108000 s, total timesteps of 361, and timestep period of 300 s. A range of timestep intervals are tested between 100 s to 600 s. This only involves minor or negligible influences on the magnitudes of quantities following the setback (e.g., neutron density minimum), but imposes a larger effect (within 13%) on the evolution afterwards (e.g., neutron density maximum at the end of simulation).

As shown in Figure 6.4, xenon concentration first increases due to the reduced burnout and continuous decay of iodine storage; then it turns around and drops down as iodine storage gets depleted. In Figure 6.7, neutron density first reduces when xenon builds up, and gradually recovers to a level higher than the initial level when xenon decays away.

Table 6.7 presents the maximum and minimum values of the quantities to reflect their magnitudes of changes during the transient. It can be observed that the cell temperature only increases by 6 °C, which is accounted for by the large heat capacity of graphite (Figure 6.9). The xenon load decrease after the setback is small, only -0.3 mk (-10.2 mk$-(-9.9$ mk$)$), verifying the weakened influence of neutron population on xenon destruction rate resulted from the small proportion of burnup in total destruction. It is also noticed that the step reactivity $d\rho$ in each timestep is dominated by the xenon load change $d\rho_{\mathrm{X}}$; the temperature feedback $d\rho_{\mathrm{T}}$ provides minor negative feedback to the overall reactivity (Figure 6.10, 6.11, and 6.12).

Quantity	Maximum	Minimum	Initial Condition
$n/(\mathrm{n/cm^3})$	0.65	0.48	0.50
$I/(\mathrm{n/cm^3})$	3.93e13	2.45e13	3.93e13
$X/(\mathrm{n/cm^3})$	3.74e13	2.72e13	3.64e13
$\rho_\mathrm{X}/\mathrm{mk}$	-7.4	-10.2	-9.9
$T/^\circ\mathrm{C}$	506	499	500
P/kW	13.1	9.8	10.1
$d\rho/\mathrm{mk}$	0.0086	-0.011	0
$d\rho_\mathrm{X}/\mathrm{mk}$	0.013	-0.016	0
$d\rho_\mathrm{T}/\mathrm{mk}$	0.0051	-0.0047	0

Table 6.7: Maximum and minimum values of various quantities to reflect their magnitudes of changes during the transient. Note that the quantities may not reach their individual maximums or minimums at the same timestep.

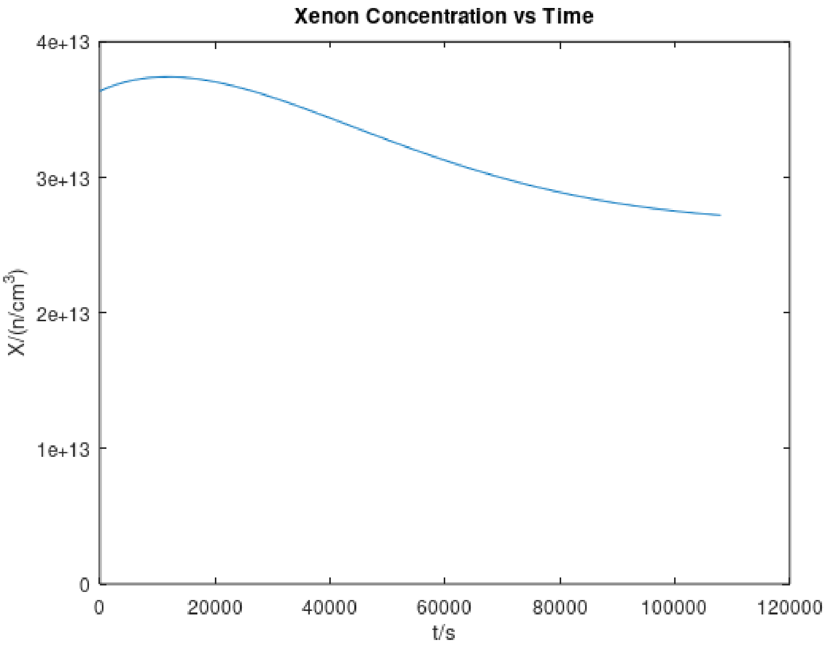

Figure 6.4: Xenon concentration during the 50% setback transient.

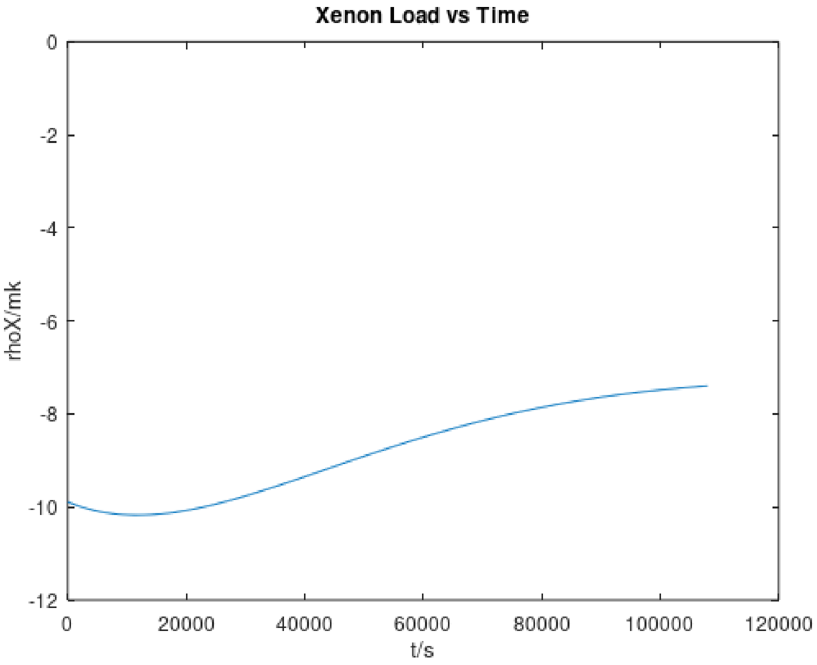

Figure 6.5: Xenon load during the 50% setback transient.

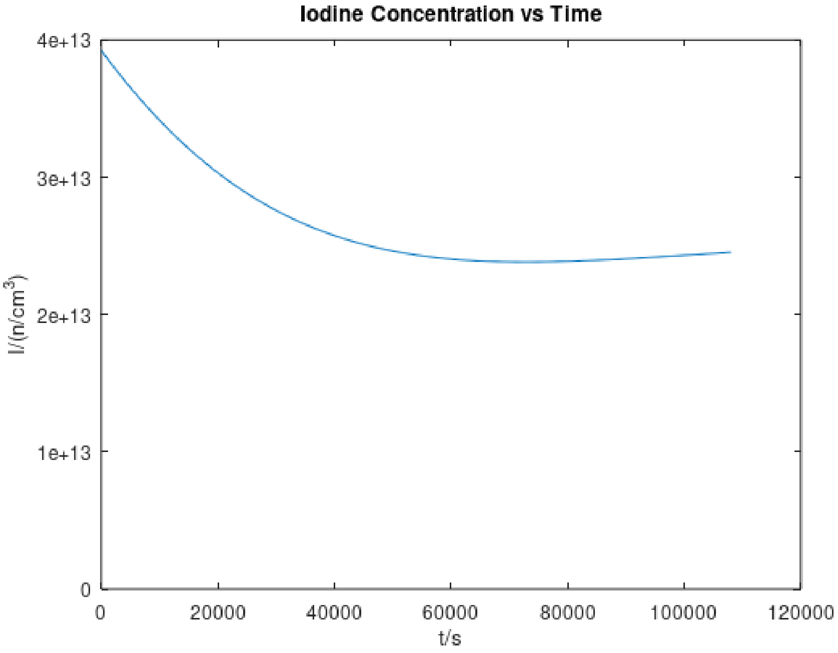

Figure 6.6: Iodine concentration during the 50% setback transient.

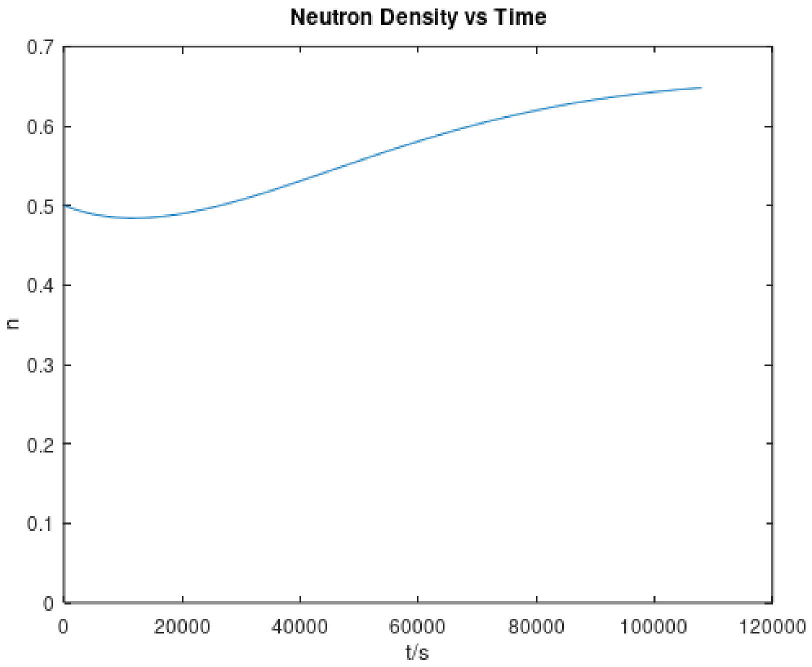

Figure 6.7: Neutron density during the 50% setback transient.

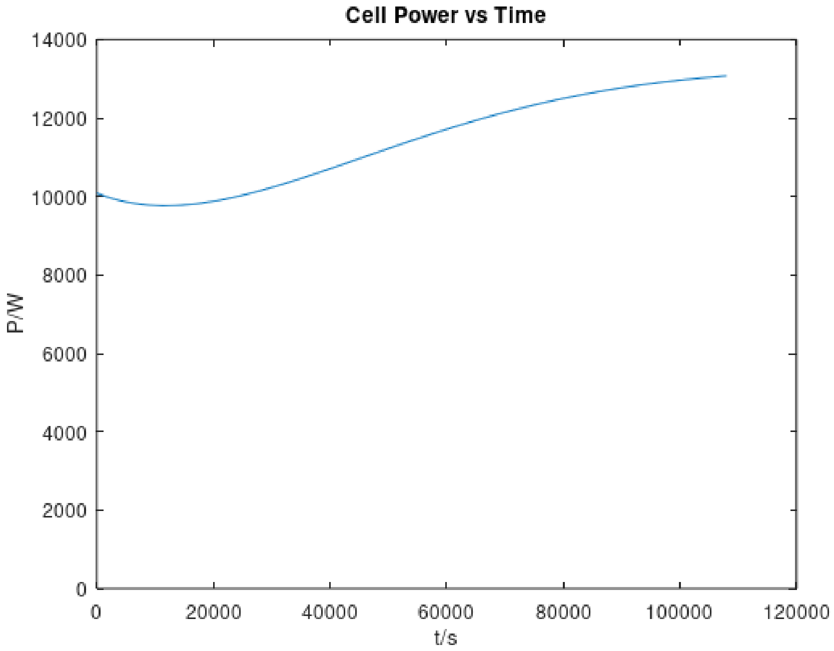

Figure 6.8: Cell power during the 50% setback transient.

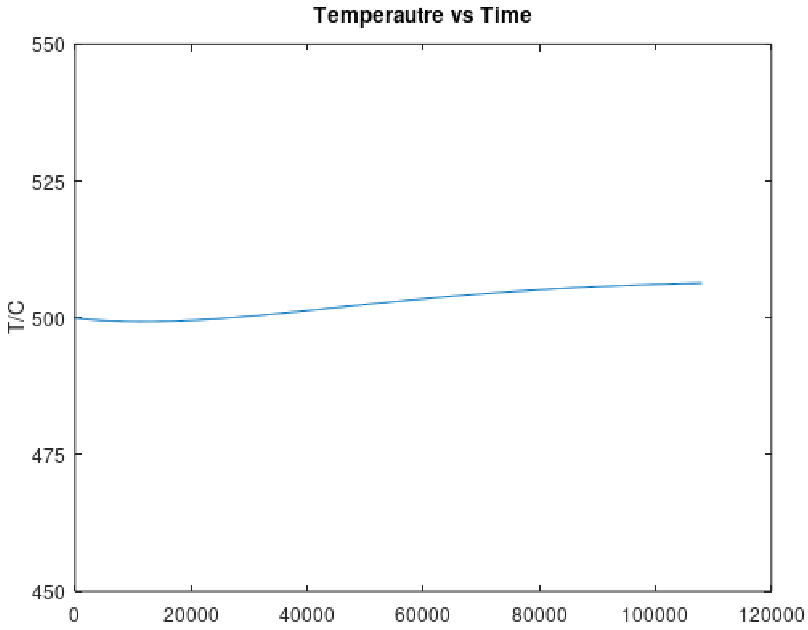

Figure 6.9: Cell temperature during the 50% setback transient.

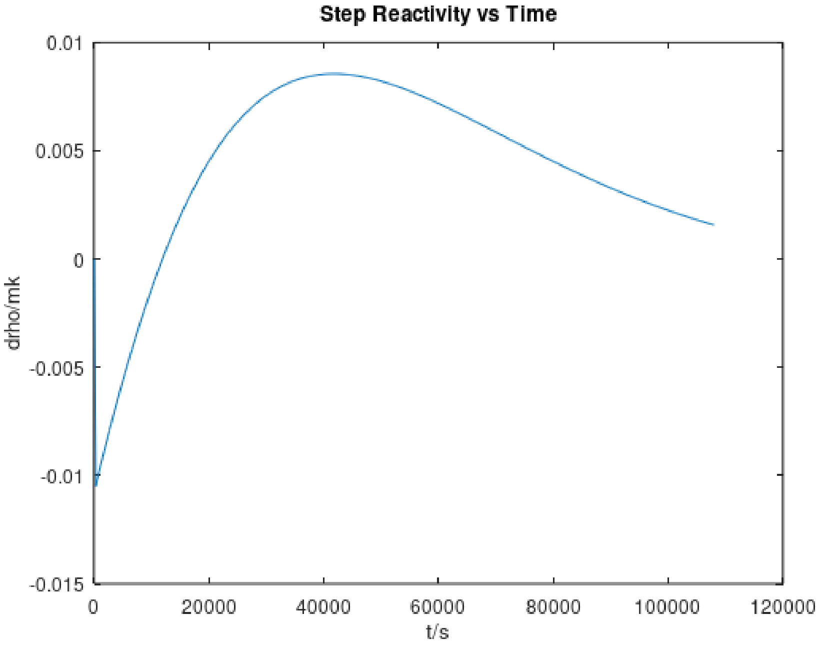

Figure 6.10: Reactivity in each timestep (300 s) during the 50% setback transient.

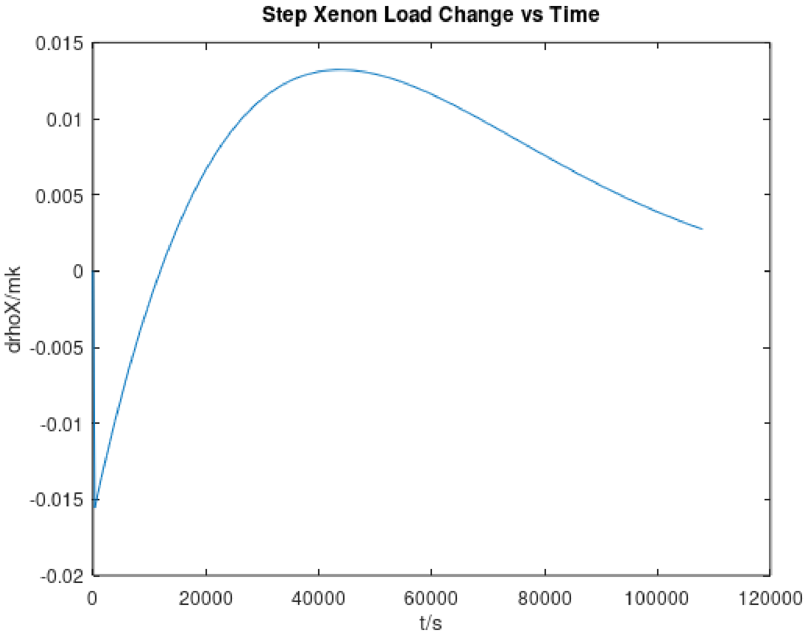

Figure 6.11: Xenon load change in each timestep (300 s) during the 50% setback transient.

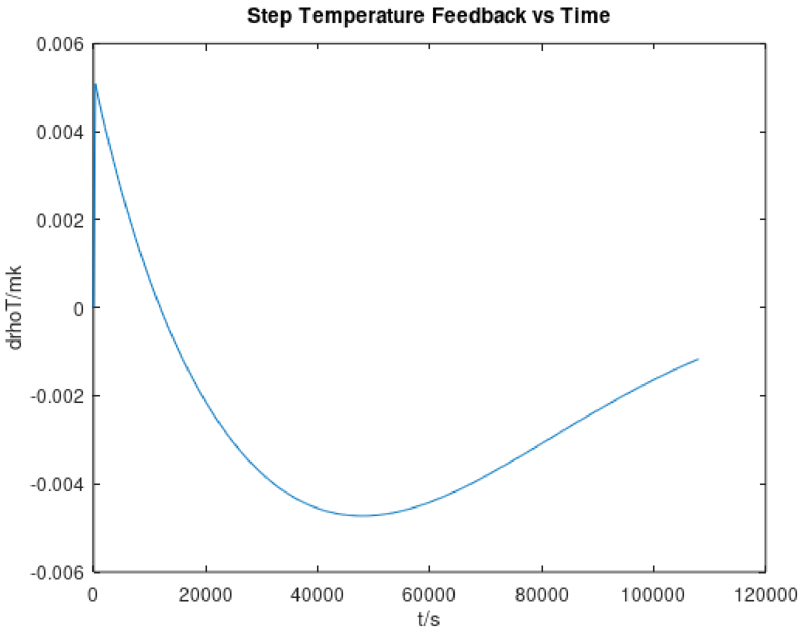

Figure 6.12: Temperature feedback in each timestep (300 s) during the 50% setback transient.

Chapter 7

Summary

In this study the thermodynamics and neutronics aspects are investigated for the Canadian Nuclear Battery$^{\mathrm{TM}}$. Various theories of the heat pipe power limits are studied through literature and the limit curves are drawn by calculations, including the sonic limit, entrainment limit, boiling limit, and capillary limit. Due to lack of information, a variety of parameters are tested, and only the formulas and parameters that give the most conservative values are finally adopted to draw the curves. The results show that the verification calculations do not agree well with the information provided by the vendor: the calculated sonic limit is lower than that of ACT; the entrainment limit is similar at temperatures below ~430 °C but higher at temperatures above than those provided by ACT; and the calculated capillary limit is smaller at temperatures below ~400 °C while larger at higher temperatures. This should be accounted for by the confidentiality and the uncertainty about the data and parameters the vendor used to carry out the evaluations. Nevertheless, the maximum allowable operation powers does not differ a lot at the nominal temperature of 500 °C: for ACT's curves the maximum power is 19 kW, while for the verification curves it is about 17 kW; to reach 19 kW the operation temperature only needs to be brought up to 510 °C. Even if the results don't comply well with each other, the theoretical investigation and calculations of the heat pipe limits in this work still provide fundamental understanding for the power limitations of heat pipes.

For core thermodynamics simulations, the nominal steady-state and a hypothetical double power transient are investigated for the 1/12 hexagonal unit cell and the TRISO particle in STAR-CCM+. Fuel segment temperatures are drawn for the 1/12 core model at BOL, MOL, and EOL to observe the change in fuel temperature profiles throughout reactor lifetime. The heat pipe power distributions are mapped out for the three nominal operation states, and several heat pipe accidents are simulated at BOL to understand the transfer of power from the failure pipe(s) to the surrounding pipes and the propagation of heat pipe failures.

Finally, neutronics calculations are carried out preliminarily for the hypothetical double power transient and 50% power setback. In the double power expedition, it is demonstrated that the negative temperature feedback from fuel and graphite is sufficient to bring the power back to nominal level. For the power setback transient the magnitudes of various quantities, such as xenon concentration, xenon load and burnout rate, before and immediately after the setback are calculated for CNB and compared with CANDU. It is found that for CNB the dominating way of xenon destruction is by xenon decay (64%) rather than xenon burnout by neutron absorption (36%) as a result of the lower neutron flux in CNB. Therefore the xenon evolution following the power drop is smoother and slower due to the weak influence of neutron population on the total xenon destruction rate.

Then the transient is simulated by assuming neutrons develop by successive prompt drops and are at equilibrium at the beginning and the end of each timestep to accommodate the large difference in timescales of neutronics and xenon decay. The curves of various quantities are plotted as a function of time. As expected, the change in xenon load following the power setback is small, only -0.3 mk (3%) of the initial value of -9.9 mk.

Overall, this study analyses the heat pipe principles and limitations, core temperature and heat pipe power distributions, as well as the neutronics and xenon transient behaviours of the Canadian Nuclear Battery$^{\text{TM}}$, providing reference information for further development of the project.

Bibliography

[1] J. Donnely and G. Penner, "Evaluation of the 500kw(e) nuclear battery core design options for uranium carbide fuel," no. SAB-TN-125, 1987.

[2] J. Donnely, "Technical note of reactor physics analysis of a 500kwe nuclear battery reactor with uranium carbide fuel," no. SAB-TN-071, 1987.

[3] J. Penner G.R. Donnely, "Technical note on evaluation of burnable poison options for the 2400-kw(t) nuclear battery," no. SAB-TN-155, 1989.

[4] T. Abram and S. Ion, "Generation-iv nuclear power: A review of the state of the science," *Energy Policy*, vol. 36, 12 2008.

[5] IAEA, "Current status and future development of modular high temperature gas cooled reactor technology," 2001.

[6] X. W. Zhou, Y. P. Tang, Z. M. Lu, J. Zhang, and B. Liu, "Nuclear graphite for high temperature gas-cooled reactors," *Xinxing Tan Cailiao/New Carbon Materials*, vol. 32, pp. 193–204, 3 2017. DOI: `10.1016/S1872-5805(17)60116-1`.

[7] B. J. Marsden and G. N. Hall, "Graphite in gas-cooled reactors," *Comprehensive Nuclear Materials*, vol. 4, pp. 325–390, 2012. DOI: `10.1016/B978-0-08-056033-5.00092-6`.

[8] A. M. Ougouag, "Improved prediction of the temperature feedback in triso-fueled reactors," Tech. Rep. INL/EXT-09-16494, 2009.

[9] J. J. Powers and B. D. Wirth, "A review of triso fuel performance models," *Journal of Nuclear Materials*, vol. 405, pp. 74–82, 1 2010. DOI: `10.1016/j.jnucmat.2010.07.030`.

[10] "Development of improved models and designs for coated-particle gas reactor fuels," The Idaho National Engineering et al., INEEL/EXT-05-02615, 2004.

[11] J. Wang, "An integrated performance model for high temperature gas cooled reactor coated particle fuel, doctoral thesis," 2004.

[12] B. H. Yan, C. Wang, and L. G. Li, "The technology of micro heat pipe cooled reactor: A review," *Annals of Nuclear Energy*, vol. 135, 2020. DOI: 10.1016/j.anucene.2019.106948.

[13] J. J. Duderstadt and L. J. Hamilton, *Nuclear Reactor Analysis*. John Wiley Sons, 1976, ch. 11, ISBN: 0-471-22363-8.

[14] Westinghouse, "Westinghouse evinci$^{\text{tm}}$*microreactor*," 2019. [Online]. Available: https://www.westinghousenuclear.com/Portals/0/new%5C%20plants/evincitm/GTO-0001_eVinci_flysheet_RSB_03-2019_003.pdf?ver=2019-04-04-140824-613.

[15] M. A. Gibson, L. Mason, and C. Bowman, "Development of nasa's small fission power system for science and human exploration," 2014. DOI: 10.2514/6.2014-3458.

[16] I. Advanced Cooling Technology. "Heat pipes for thermal management." (n.d.), [Online]. Available: https://www.1-act.com/innovations/heat-pipes/#how.

[17] B. Zohuri, *Heat pipe design and technology: Modern applications for practical thermal management, second edition*. 2016, ch. 4, ISBN: 9783319298412. DOI: 10.1007/978-3-319-29841-2.

[18] J. E. Werner, A. J. Hummel, J. C. Kennedy, *et al.*, "Preliminary assessment of two alternative core design concepts for the special purpose reactor," Idaho National Laboratory, INL/EXT-17-43212, 2018.

[19] A. Faghri, "Review and advances in heat pipe science and technology," *Journal of Heat Transfer*, vol. 134, pp. 1–18, 12 2012. DOI: 10.1115/1.4007407.

[20] L. AliExpress Alidwantop Technology CO. "90mm heat pipe 6 heatpipe desktop computer cpu cooler fan bracket ultra quiet heatsink for intel 1156/1155/1150/775." (), [Online]. Available: https://www.aliexpress.com/item/32878021500.html.

[21] I. Advanced Cooling Technology. "Heat pipes material compatibility - fluid/evelope/wick." (n.d.), [Online]. Available: https://www.1-act.com/resources/heat-pipe-resources/materials/compatibility/.

[22] Y. S. Jeong, K. M. Kim, I. G. Kim, and I. C. Bang, "Hybrid heat pipe based passive in-core cooling system for advanced nuclear power plant," *Applied Thermal Engineering*, vol. 90, 5 2015.

[23] Y. S. Jeong and I. C. Bang, "Hybrid heat pipe based passive cooling device for spent nuclear fuel dry storage cask," *Applied Thermal Engineering*, vol. 96, 2016.

[24] K. S. Kozier and H. E. Rosinger, “The nuclear battery: A solid-state, passively cooled reactor for the generation of electricity and/or high-grade steam heat,” 1988.

[25] Y. Oka, H. Madarame, and M. Uesaka, *Nuclear Reactor Design*. Springer, 2014, ISBN: 978-4-431-54898-0.

[26] F. B. Brown, *Fundamentals of monte carlo particle transport*, 2005.

[27] J. Leppänen, M. Pusa, T. Viitanen, and V. Valtavirta, “The serpent monte carlo code: Status, development and applications in 2013,” *Annals of Nuclear Energy*, vol. 82, 2014, ISSN: 0306-4549.

[28] J. C. Ragusa and V. S. Mahadevan, “Consistent and accurate schemes for coupled neutronics thermal-hydraulics reactor analysis,” *Nuclear Engineering and Design*, vol. 239, 2009. DOI: `10.1016/j.nucengdes.2008.11.006`.

[29] B. Rouben, “Course material: Nuclear reactor analysis (reactor physics),” McMaster University.

[30] J. R. Lamarsh and A. J. Baratta, *Introduction to Nuclear Engineering*. 2012, ISBN: 13: 978-0-13-276457-5.

[31] S. Reodikar, *Unpublished research report for the Canadian Nuclear Batter*$^{\text{TM}}$ *program*. 2021.

[32] B. Zohuri, *Heat Pipe Design and Technology: Modern Applications for Practical Thermal Management, Second Edition*. 2016, ISBN: 978-3-319-29840-5.

[33] S. Chi, *Heat Pipe Design and Technology*. 1976.

[34] E. Levy, “Theoretical investigation of heat pipes operating at low vapor pressures,” *Journal of Manufacturing Science and Engineering, Transactions of the ASME*, vol. 90, 1968. DOI: `10.1115/1.3604687`.

[35] D. A. Reay, P. A. Kew, and R. J. McGlen, *Heat Pipes: Theory, Design and Applications*. 2014, ch. 2, ISBN: 9780080982663. DOI: `10.1016/b978-0-08-098266-3.00002-9`.

[36] C. Busse, “Theory of the ultimate heat transfer limit of cylindrical heat pipes,” *International Journal of Heat and Mass Transfer*, vol. 16, pp. 169–186, 1 1973. DOI: `10.1016/0017-9310(73)90260-3`.

[37] P. D. Dunn and D. A. Reay, *Heat Pipes*. 1976, ISBN: 13: 9780080293554.

[38] T. Cotter, “Theory of heat pipes,” Los Alamos Scientific Laboratory, LA-3246-MS, 1965.

[39] I. Advanced Cooling Technology. "Capillary limit." (n.d.), [Online]. Available: https://www.1-act.com/resources/heat-pipe-performance/capillary-limit/.

[40] P. Nemec, "Porous structures in heat pipes," 2018. DOI: 10.5772/intechopen.71763.

[41] J. D. Hales, R. L. Williamson, S. R. Novascone, D. M. Perez, B. W. Spencer, and G. Pastore, "Multidimensional multiphysics simulation of triso particle fuel," *Journal of Nuclear Materials*, vol. 443, 2013.

[42] J. K. Fink, "Thermophysical properties of uranium dioxide," *Journal of Nuclear Materials*, vol. 279, 2000. DOI: 10.1016/S0022-3115(99)00273-1.

[43] W. D. Swank, F. I. Valentin, M. Kawaji, and D. M. McEligot, "Thermal conductivity of g-348 isostatic graphite," *Nuclear Technology*, vol. 199, pp. 103–109, 1 2017. DOI: 10.1080/00295450.2017.1317530.

[44] IAEA, "Thermophysical properties of materials for nuclear engineering: A tutorial and collection of data," Tech. Rep., 2008.

[45] P. Jain and Saxena, "Transport properties of helium in the temperature range 400 2300 k," *Chemical Physics Letters*, vol. 36, pp. 489–491, 4 1975.

[46] W. F. Skerjanc, J. T. Maki, B. P. Collin, and D. A. Petti, "Evaluation of design parameters for triso-coated fuel particles to establish manufacturing critical limits using parfume," Tech. Rep., 2016. DOI: 10.1016/j.jnucmat.2015.11.027.

[47] S. Reodikar, "Core design optimization and steady state criticality analysis of the canadian nuclear battery," 2021.

[48] W. Stacey, *Nuclear Reactor Physics*. Wiley-VCH, 2001, ISBN: 0-471-39127-1.

[49] B. E. Poling, D. G. F. George H. Thomson, R. L. Rowley, and W. V. Wilding, "Perry's chemical engineers' handbook," 1999, ch. 2. DOI: 10.1036/0071511253.

[50] W. D. Weatherford Jr, J. C. Tyler, and P. M. Ku, "Properties of inorganic energy-conversion and heat-transfer fluid for space applications," Southwest Research Institution, San Antonio, WADD-TR-61-96, 1961.

[51] H. H. Coe, "Summary of thermophysical properties of potassium," Lewis Research Center, NASA, 1965. DOI: 10.1016/b978-012373588-1/50016-4.

[52] N. B. Vargaftik, *Handbook of Physical Properties of Liquids and Gases*. Hemisphere, 1975, ISBN: 978-3-642-52506-3.

Appendix A: Variables and Power Limits of Potassium Heat Pipe

T/°C	Busse/kW	$Q = LA_{\mathrm{v}}\rho_{\mathrm{v}}U$/kW	Chi/kW
327	0.4	0.4	0.3
427	5.4	7.6	6.5
527	26.2	34.2	30.5
627	92.9	130.5	116.5
727	287.5	387.8	347.7
827	681.8	856.2	787.7
927	1374.3	1694.4	1541.4

Table 7.1: Sonic limit of potassium heat pipe calculated with various equations.

T/°C	Entrainment Limit/kW
327	2.3
427	10.9
527	32.4
627	71.2
727	118.6
827	167.0
927	216.5

Table 7.2: Entrainment limit of potassium heat pipe.

T/°C	Capillary Limit/kW
327	7.7
427	21.1
527	28.6
627	35.7
727	38.9
827	40.2
927	41.3

Table 7.3: Capillary limit of potassium heat pipe. $r_{\text{eff}} = 2d = 0.1$ mm.

T/°C	P_s/Pa	$\rho_v/(\text{kg/m}^3)$	$\rho_l/(\text{kg/m}^3)$	$\mu_v/(\text{Pa}\cdot\text{s})$	$\mu_l/(\text{Pa}\cdot\text{s})$
327	92.6	0.0003160	766.9	1.46e-5	2.687e-4
427	1022	0.007208	736.8	1.571e-5	2.191e-4
527	6116	0.03524	713.6	1.682e-5	1.819e-4
627	21829	0.1297	691.2	1.798e-5	1.530e-4
727	75293	0.3764	670.4	1.906e-5	1.364e-4
827	200093	0.8329	650.3	2.017e-5	1.240e-4
927	443969	1.602	632.2	2.112e-5	1.116e-4

Table 7.4: Table of variables 1 of potassium. Note that the yellow box indicates an extrapolated value. Sources of data: P_s [49], [50], ρ_v [49], [50], ρ_l [49], [50], μ_v [51], μ_l [51].

$T/°\mathrm{C}$	γ_g	$L/(\mathrm{J/kg})$	$\sigma/(\mathrm{N/m})$	C_son(theoretical)/(m/s)	C_son (experimental)/(m/s)
327	1.668	2.575e+6	0.0982	461.3	483.2
427	1.656	2.326e+6	0.0922	496.5	500.0
527	1.644	2.077e+6	0.0862	528.9	516.8
627	1.638	2.035e+6	0.0802	559.9	546.1
727	1.618	1.991e+6	0.0742	586.6	571.8
827	1.604	1.947e+6	0.0682	612.5	583.5
927	1.59	1.900e+6	0.0622	637.0	615.3

Table 7.5: Table of variables 2 of potassium. Note that the yellow boxes indicate extrapolated values. Sources of data: γ [50], L [50], σ [52], C_son (theoretical) Eq. 4.2 [18], C_son (experimental) [50]. There are two data curves of surface tension of liquid potassium in [51]. The curve chosen in this report is the lower one; the curve of higher values is linear to about 650 °C, and therefore it might be at least safe to extrapolate to 627 °C.

Appendix B: Variables and Power Limits of Sodium Heat Pipe

Temperature/°C	Sonic Limit/kW
327	4.2
427	15.6
527	34.4
627	51.9
727	71.2
827	83.6
927	55.0

Table 7.6: Sonic limit of sodium heat pipe calculated with Busse's equation.

T/°C	Entrainment Limit/kW
327	1.4
427	5.6
527	16.0
627	46.8
727	116.9
827	197.4
927	289.1

Table 7.7: Entrainment limit of sodium heat pipe.

T/°C	Capillary Limit/kW
327	4.2
427	15.6
527	34.4
627	51.9
727	71.2
827	83.6
927	55.0

Table 7.8: Capillary limit of sodium heat pipe. $r_{\text{eff}} = 2d = 0.1$ mm.

T/°C	P_{s}/Pa	$\rho_{\text{v}}/(\text{kg/m}^3)$	$\rho_{\text{l}}/(\text{kg/m}^3)$	$\mu_{\text{v}}/(\text{Pa}\cdot\text{s})$	$\mu_{\text{l}}/(\text{Pa}\cdot\text{s})$
327	4.7	0.000022	873.2	1.480e-5	3.276e-4
427	95.1	0.000396	849.4	1.660e-5	2.690e-4
527	876	0.00327	825.6	1.827e-5	2.298e-4
627	4876	0.0165	801.8	2.010e-5	2.018e-4
727	19220	0.05998	778.0	2.211e-5	1.809e-4
827	58428	0.1681	754.2	2.398e-5	1.645e-4
927	146540	0.3966	730.4	2.577e-5	1.514e-4

Table 7.9: Table of variables 1 of sodium. Note that the yellow box indicates an extrapolated value. Sources of data: [52]

$T/^{\circ}\mathrm{C}$	γ_{g}	$L/(\mathrm{J/kg})$	$\sigma/(\mathrm{N/m})$	C_{son}(theoretical)/(m/s)
327	1.635	4.429e+6	0.1721	595.5
427	1.635	4.341e+6	0.1621	643.2
527	1.625	4.237e+6	0.1521	685.5
627	1.604	4.131e+6	0.1421	722.4
727	1.584	4.026e+6	0.1321	756.7
827	1.565	3.925e+6	0.1221	788.9
927	1.548	3.829e+6	0.1121	819.5

Table 7.10: Table of variables 2. Note that the yellow boxes indicate extrapolated values. Sources of data: γ_{g} [50], C_{son} (theoretical) Eq. 4.2 [18], other: [52].

Appendix B: Thermophysical Properties of Core Materials

T/°C	k/(W/m-K)
25	0.412
50	0.451
100	0.54
150	0.643
200	0.762
250	0.898
300	1.053
350	1.224
400	1.414

Table 7.11: Helium thermal conductivity [45].

T /°C	c_{p}/(J/kg-K)
22.6	726
101.0	933
199.3	1154
301.6	1341
401.6	1487
501.6	1604
601.6	1697
701.7	1774
801.3	1836
900.8	1887
1000.9	1929

Table 7.12: Graphite specific heat [43]. A polynomial fitting to the data is used as the input to the specific heat of moderator graphite: $c_{\mathrm{p}} = 9E-07T^3 - 0.0025T^2 + 2.9252T + 662.46, T[C]$.

T/°C	k/(W/m-K)
22.6	133.02
101.0	128.54
199.3	117.62
300.8	104.03
401	94.57
500.9	87.05
601.0	80.37
701.1	75.02
800.9	69.92
900.7	66.68
1000.7	63.11

Table 7.13: Graphite thermal conductivity [43]

T/°C	k(W/m-K)
100	16.4
150	15.9
200	15.5
250	15.2
300	14.9
350	14.6
400	14.3
450	14.1
500	13.8
550	13.6
600	13.4
650	13.3
700	13.1
750	13.0
800	12.8
850	12.7
900	12.6
950	12.4
1000	12.4
1050	12.3
1100	12.1
1150	12.0

Table 7.14: Fuel stack thermal conductivities. Calculated by a packing fraction of 0.55, the thermal conductivities of UO_2 and a constant thermal conductivity of 20 W/m-K for matrix graphite. Inputed as $c_{\mathrm{p}} = 9\text{e-}7T^3 - 0.0025T^2 + 2.9252T + 662.46, T[C]$.

Length of evaporator/m	1.5
Length of upper adiabatic section/m	0.6
Length of lower adiabatic section/m	0.6
Length of condenser/m	0.75
Radius of vapour core/mm	24.0
Outer radius of wick/mm	24.7
Outer radius of pipe wall/mm	25.4

Table 7.15: Dimensions of heat pipes in the 3D geometry models.

T/°C	c_p (J/kg-K)
27	459
127	602
227	717
327	809.6
427	883.3
527	941.5
627	987.2
727	1023.3
827	1052.7
927	1078.3
1027	1102.9
1127	1129.4
1227	1160.5

Table 7.16: Specific heat of fuel stack. Calculated by a packing fraction of 0.55, the c_p of UO_2 and matrix graphite. Input as $c_p = 5E-07T^3-0.0014T^2+1.5831T+421.07, T[C]$.

Appendix D: Settings of the Prism Layers in Mesh 1 and Mesh 2

Prism layers are layers of orthogonal prismatic cells generated on the boundaries and walls of a geometry component with core volume meshing, which are important for the accuracy of flow solutions. Mesh 1 is first tested to investigate the appropriate ranges of parameters. Mesh 2 refines the prism layers by reducing the size of each layer and increasing the total number and thickness of layers. This is to achieve a better modeling of the heat transfer between components, e.g., the diffusion of heat from fuel rods to moderator.

For mesh 2 the fuel rods do not have prism layers inside them because the total thickness exceeds the radius of fuel rods. Thus the modeling outside the fuel rods, which is in the moderator, is refined, but the simulating inside the fuel rods may therefore be degraded. The settings of components that use specific volume control (helium gaps, fuel rods, heat pipes) overwrite those in the general control. As a result, the prism layers on both sides of the interfaces of the specifically defined components are determined by their individual volume control settings.

Geometry component	Setting	Mesh 1	Mesh 2
All	Volume growth rate	1.2	1.2
	Prism layer stretching	1.5	1.4
Reflectors	Base size	0.03 m	0.03 m
	Prism layer total thickness	0.02 m	0.02 m
	Number of prism layers	4	5
Helium gaps, Fuel rods	Base size	0.005 m	0.005 m
	Number of prism layers	3	5
	Prism layer total thickness	0.01 m	0.016 m
Heat pipes	Base size	0.01 m	0.01 m
	Number of prism layers	2	5
	Prism layer total thickness	0.08 m	0.016 m

Table 7.17: Settings of mesh for mesh 1 and mesh 2. Reflectors use the overall control settings of the mesh. Helium gaps, fuel rods, and heat pipes are specified by volume control. The mesh sizes for the same geometry component are the same in the two meshes.

Appendix E: Script of the 50% Setback Transient Code

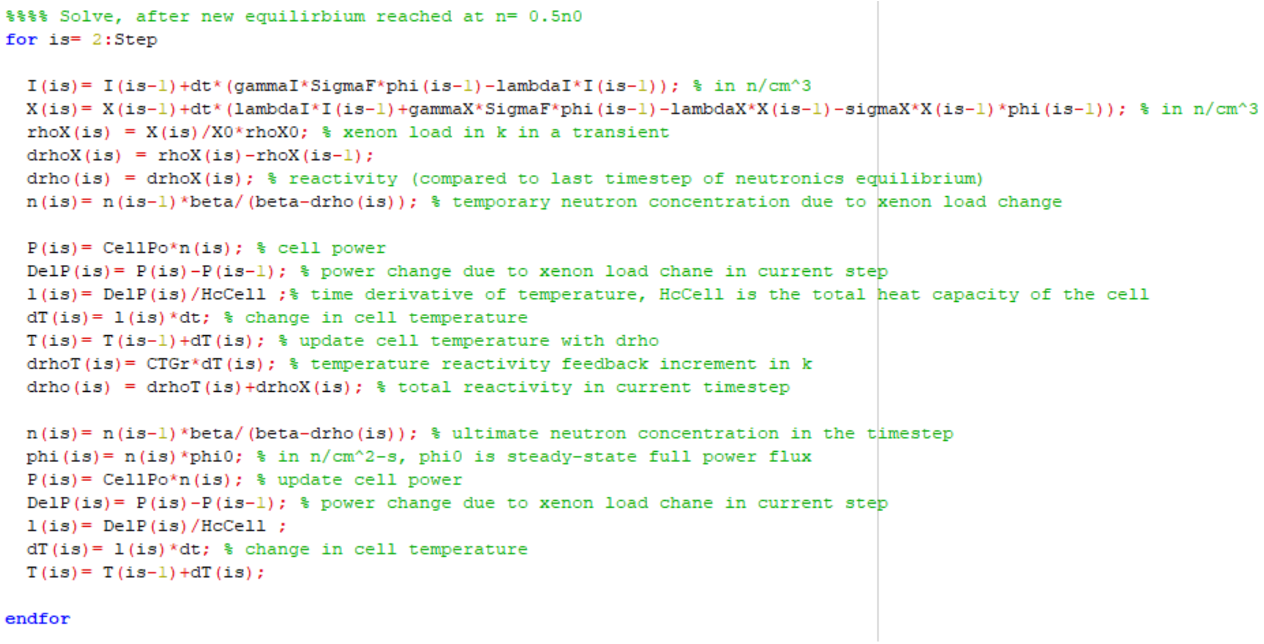

```
%%%% Solve, after new equilirbium reached at n= 0.5n0
for is= 2:Step

  I(is)= I(is-1)+dt*(gammaI*SigmaF*phi(is-1)-lambdaI*I(is-1)); % in n/cm^3
  X(is)= X(is-1)+dt*(lambdaI*I(is-1)+gammaX*SigmaF*phi(is-1)-lambdaX*X(is-1)-sigmaX*X(is-1)*phi(is-1)); % in n/cm^3
  rhoX(is) = X(is)/X0*rhoX0; % xenon load in k in a transient
  drhoX(is) = rhoX(is)-rhoX(is-1);
  drho(is) = drhoX(is); % reactivity (compared to last timestep of neutronics equilibrium)
  n(is)= n(is-1)*beta/(beta-drho(is)); % temporary neutron concentration due to xenon load change

  P(is)= CellPo*n(is); % cell power
  DelP(is)= P(is)-P(is-1); % power change due to xenon load chane in current step
  l(is)= DelP(is)/HcCell ;% time derivative of temperature, HcCell is the total heat capacity of the cell
  dT(is)= l(is)*dt; % change in cell temperature
  T(is)= T(is-1)+dT(is); % update cell temperature with drho
  drhoT(is)= CTGr*dT(is); % temperature reactivity feedback increment in k
  drho(is) = drhoT(is)+drhoX(is); % total reactivity in current timestep

  n(is)= n(is-1)*beta/(beta-drho(is)); % ultimate neutron concentration in the timestep
  phi(is)= n(is)*phi0; % in n/cm^2-s, phi0 is steady-state full power flux
  P(is)= CellPo*n(is); % update cell power
  DelP(is)= P(is)-P(is-1); % power change due to xenon load chane in current step
  l(is)= DelP(is)/HcCell ;
  dT(is)= l(is)*dt; % change in cell temperature
  T(is)= T(is-1)+dT(is);

endfor
```

Figure 7.1: The script of 50% setback transient code.